Evaluation of Systematic Uncertainties in the Precise Magnetic Field Measurements for the Muon g-2 Experiment

by

Kyun Woo Chris Hong

Seoul, Korea

BA in Mathematics, University of Virginia, 2015
BS in Physics, University of Virginia, 2015
MA in Physics, University of Virginia, 2021

A Dissertation presented to the Graduate Faculty
of the University of Virginia in Candidacy for the Degree of
Doctor of Philosophy

Department of Physics

University of Virginia
May 2023 **will be Conferred**

Committee Members

Dr. Dinko Pocanic
Dr. Marija Vucelja
Dr. Hung Q Pham
Dr. Mark Whittle

Abstract

The Fermilab E989 Muon g-2 experiment's goal is to measure the anomalous magnetic dipole moment of the muon, a_μ with a precision of 140 ppb to test the prediction of a_μ in the Standard Model (SM) of subatomic physics. The Brookhaven National Laboratory (BNL) experiment E821, the most recent previous muon g-2 measurement, produced a result in 2005 with a precision of 0.54 ppm, that differed by 3.5 to 3.7 σ from the SM prediction. After more than 10 years, Fermilab E989 continued the BNL measurement, taking the first physics data in 2018. At the time of this writing, Run 6 is ongoing and measurements of Runs 1 through Run 5 are completed. The targeted 4-fold improvement in precision would yield an above 5 sigma tension assuming the central values don't change, opening the possibility of discovery of physics beyond the Standard Model.

To reach the goal of 140 ppb, E989 aims for 100 ppb statistical and 100 ppb systematical uncertainties. In order to measure a_μ, there are two major observables needed: ω_a, the anomalous precession frequency, and $\tilde{\omega}'_p$, the average magnetic field weighted by the muon distribution around the 14-meter diameter storage ring, determined at a 70 ppb level. The field is precisely mapped using a field mapper, which carries 17 NMR probes, running around the muon storage region every 2 or 3 days. Calibration of these 17 NMR probes to the absolute probe, in-situ water-based calibration probe, is crucial for accurate measurements. The field's drift between the field maps is tracked using 378 NMR probes installed at fixed positions around the

outside of the muon storage ring. The result of the Run 1 dataset was published in April 2021 and agreed with the BNL experiment. Analysis of Run 2 and 3 data is nearing completion as of this writing. This dissertation discusses the experiment, and detailed methods applied in evaluating the systematic uncertainties for the magnetic field measurement with a focus on Run 2 and 3.

To Grand Parents, Father, Mother, and Brother.

그리고 하늘에 계신 이향단 베로니카 할머니께

Contents

List of Tables

List of Figures

List of Abbreviations

Abbreviations

BNL	Brookhaven National Laboratory
BSM	Beyond the Standard Model
BO	betatron oscillation
CBO	coherent betatron oscillation
CERN	European organization for nuclear research
DAQ	data Acquisition
DQM	data quality management
E821	Brookhaven Muon g-2 Experiment
E989	Fermilab Muon g-2 Experiment
EIW	Edge Ignore Window
ESQ	electrostatic quadrupoles
EW	electroweak
FFT	fast Fourier transform
FID	free induction decay.
FNAL	Fermi National Accelator Laboratory
Freq	frequency
FXP	fixed probe
Had	hadronic
HLbL	hadronic light-by-light

HVP	hadronic vacuum polarization
IBMS	inflector beam monitoring systems
LHC	large hadron collider
LO	leading order
Lo	local oscillator
MSSM	minimal supersymmetric standard model
NMR	nuclear magnetic resonance
NNLO	next next leading order
NLO	next leading order
NP	new physics
PP	plunging probe
ppb	part per billion
ppm	part per million
ppt	part per trillion
QCD	quantum chromodynamics
QED	quantum electrodynamics
RF	radio frequency
RMS	root mean square
SEC	seconds
SiPM	silicon photomultiplier
SM	standard model
SR	storage ring
SUSY	supersymmetry
TR	trolley probe
UMass	University of Massachusetts
UVa	University of Virginia

Acknowledgements

I want to thank the University of Virginia's Physics Department for giving me the opportunity and courage to explore the world of physics for 14 years. During my Undergrad, I had the opportunity to acquire various Physics knowledge and perspectives from brilliant Professors. During my Ph.D. program, I had an incredible experience in the field of particle sub-atomic physics with my phenomenal advisor, Dinko Pocanic. I especially want to thank Dinko for supporting me in everything to make it possible for me to complete my Ph.D. Degree. I also want to thank Peter Winter, Ran Hong, and Simon Corrodi from the Argonne National Laboratory (ANL) High Energy Physics (HEP) muon g-2 team. When I first moved to Fermilab and joined the E989 muon g-2 experiment, I was concerned and anxious during this new chapter in my studies. However, the ANL g-2 team was incredibly supportive and enlightened me in this transition and time at Fermilab. Peter helped me organize my projects on time so that I could achieve various studies. Ran taught me everything from the fundamentals of the experiment to the advanced frameworks. With Ran's guidance, I was able to concrete the cornerstones of numerous frameworks that were used. Simon, my mentor, made a significant impact in helping me with my research and guided me throughout this dissertation journey. In addition to the ANL g-2 team, I sincerely would like to thank everyone on the muon g-2 field team. Outside of school and research, I want to thank all my friends for supporting me during the duration of my Ph.D. I want to especially give a shoutout to my best

friends: Sonwoo Kim for being a great friend despite our opposite personalities; JB Park for all the fun memories that fueled my happiness in my life; Taehyun Kim for helping me in the non-physics part of my life; Jack Kim for all the drinks and hangovers together; Eungchang Kim and Sungwoo Jun for all the laughs from their crazy stories; Soobeom Park and Boyoung Suh for their warm welcomes whenever I returned to Virginia; Steven Kim, Monica Lee, and Cheolmin Kim for giving me great experiences in Chicago; Timothy Lee, Terry Kim, Peter Suh, David Ok, and Seungyun Jung for supporting me from the Los Angeles Area; Lastly, Michelle Lee for being my mental supporter and English Mentor. Finally, I want to thank my family for everything they have done for me. This dissertation is dedicated to my family.

1

Introduction

Precision measurements of the subatomic particles have been used to test the Standard Model (SM) of particle physics for many decades. In particular, precision prediction from a theory that can be tested experimentally provide the opportunity to test the SM. The g-factor of fundamental particles is such an opportunity. The g-factor of the spin-1/2 particle, g, is the quantity connecting spin, $\vec{s}$, to its magnetic moment, $\vec{\mu}$. $\vec{\mu}$ connecting to $\vec{s}$ is expressed as [1]:

$$\vec{\mu} = g\frac{q}{2m}\vec{s}, \tag{1.1}$$

where q is a charge of a particle and m is a mass of a particle. In particle physics, the Dirac equation is a relativistic wave equation derived by Paul Dirac in 1928. It describes all spin-1/2 massive particles, called **Dirac particles**. In the Dirac equation, the g-factor of Dirac particles equals 2. However, the g-factor of the particles is slightly larger than 2 because there are other contributions to modifying the g-factor such as QED, weak, hadronic, and more. In the beginning, physicists used electrons to measure the g-factor, and the first result was published by P. Kusch and H. M. Foley in 1948 [2]. The measurements have been continued and in the late 1900s,

the magnetic moment of the electron was again measured as a test of the SM and quantum electrodynamics (QED). Two electron g-2 measurements were conducted in 2006[3] and 2008[4]. The latest g-2 electron measurement[5] is published in 2023 and the precision of the new measurement is 0.13 ppt. The experimental outcome and QED theory calculation were in good agreement. Thus, there was no significant discrepancy in electron g-2 between experimental and theoretical, therefore, physicists tried to measure the g-2 value of other particles besides the electron.

Muons were discovered in 1936. Muons are 206.78 times heavier than an electron ($m_\mu = 207\ m_e$) and have the same properties as electrons for charge and interactions in SM. Muon's mean lifetime is about 2.2 μs and this long lifetime allows us to prepare beams of muons and store them which is important to get better statistics and one of the main key ingredients for precision measurement of a_μ. In addition, the parity violation in weak decay is also important. The anomalous magnetic momentum is defined as

$$a = \frac{g-2}{2}. \tag{1.2}$$

The SM prediction of a_μ, the anomalous muon magnetic moment, is determined from the sum of the contributions, such as QED[6], electroweak (EW)[7], the hadronic vacuum polarization (HVP)[7], and other hadronic contributions (more detail explanation in Chapter 2). QED is the leading order contribution to a_μ.

The first muon g-2 experiment at CERN in 1965 was mainly motivated to test QED. The experiment used non-relativistic muons drifting in a magnetic gradient. Then, forward- backward decay asymmetry was measured. CERN 1 measured a_μ with a precision of 4200 ppm in 1962 [8]. CERN II used relativistic muons and was the first muon g-2 experiment that used a storage ring, thus a_μ was directly measured. The CERN II measured a_μ with a precision of 270 ppm [9]. CERN III used electric

quadrupoles for vertical focusing, allowing a more uniform magnetic field. Electric quadrupoles will be explained in detail in Section 3.3.3. CERN III also improved to use the pion injection into the ring instead of proton injections to reduce the background signal and noise in the detectors. CERN III a_μ was measured with a precision of 7.3 ppm [10].

After CERN I, II, and III, the E281 was planned at Brookhaven National Laboratory (BNL) in the late 1900s. At BNL, the magnetic field was set to 1.45 T and the NMR probes were used for field measurements to map and track the field. NMR probes are discussed in more detail in Chapter 5. Not only did the field and field measurements been improved, but also many parts of the experiment such as the electric quadrupoles system and collimators system had been improved during this time. The BNL experiment result was published in 2006 with a precision of 0.54 ppm [11], which was a 3.5 to 3.7 σ discrepancy between the experiment and theory.

The experiment was continued at Fermilab 10 years after the BNL experiment ended. The new muon g-2 experiment at Fermilab, E989, aims for a four-fold reduction in the uncertainty, with equal systematic and statistical errors, to a total precision of 0.14 ppm. More experimental parts of the E989 will be introduced in Chapter 3. The first physics data, Run 1, was taken in 2018 and published in 2021 [12] with a precision of 0.46 ppm. Fig 1.1 shows the result of the first experimental run, which shows that 4.2 standard deviation discrepancy between the theoretical and experimental values. This result confirmed the BNL experimental results after 20 years. Table 1.1 shows the summary of results of a_μ in different experiments from CERN I to Fermilab.

Focusing on the field measurement experienced by muons, $\tilde{\omega}'_p$, the core topic of this dissertation, the Run-1 systematic uncertainties of $\tilde{\omega}'_p$ is 114 ppb which exceeds the 70 ppb error budget allocated to the field analysis for the experiment. The detailed field measurement errors for Run 1 is shown in Table 1.3. The electrostatic quadrupoles

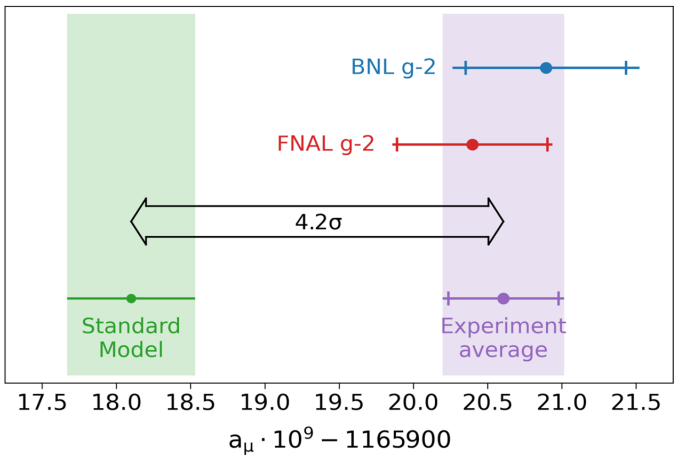

FIGURE 1.1: The result of the muon g-2 experiment first experimental run [13].

Table 1.1: Results of a_μ from various experiments up to today [14]. γ_μ is the momentum of the muon.

Experiment	Magnet	Injection	γ_μ	$\delta a_\mu / a_\mu$
CERN I (1965)	Long dipole magnet, B = 1.6 T	μ	1	0.4%
CERN II (1974)	r = 2.5 m storage ring, B=1.71 T	p	12	270 ppm
CERN III (1978)	r = 7.1 m storage ring, B=1.47 T	π	29.3	7.3 ppm
BNL (2006)	r = 7.1 m storage ring, B=1.45 T	μ	29.3	0.54 ppm
FNAL Run 1 (2021)	r = 7.1 m storage ring, B=1.45 T	μ	29.3	0.46 ppm

(ESQ) transient dominates the error which is 92 ppb. However, Run 1 is only 6% of the data so there is no expectation for the Run 1 result to meet 70 ppb. The collaboration is still on track to achieve the systematic goal of 70 ppb for the final result of the full statistics of data.

There were many improvements beyond Run 1 in reducing the uncertainty to achieve the error budget. For the field measurement, there were mainly three parts that have improved: the in-situ calibration of the field mapper (Section 7.2), the precision frequency extraction from NMR-based magnetic field monitoring (Chapter 5), and the magnetic field tracking between field maps. For the calibration, automatic scripts were implemented to reduce human error and increase the precision of the measurements. With automatic scripts, the calibration campaign had been designed

Uncertainty Source	E821 (ppb)	E989 (ppb)
ω_a statistical	460	100
ω_a systematics	180	70
$\tilde{\omega}'_p$ systematics		
Absolute calibration	50	35
Trolley probe calibration	90	30
Fixed probe interpolation	50	30
Muon distribution	30	10
Time-dependent external fields	-	5
Others	100	30
$\tilde{\omega}'_p$ total	170	70
Total	540	140

Table 1.2: A comparison of the final uncertainties from BNL E821 [11] and the proposed error budget for Fermilab E989 [15].

Systematic	Correction (ppb)	Uncertainty (ppb)
Absolute calibration	0	15
Trolley calibration	0	28
Configuration	-1	23
Trolley baseline $m^{tr}(0)$	-13	25
Fixed probe baseline $m^{fp}(0)$	0	8
Fixed probe runs $m^{fp}(t)$	0	1
Total	-14	48

Table 1.3: The result for the field measurement errors for Run 1[13].

Average over all data sets in Run 1	
Field measurement	56
ESQ Transient	92
Kicker Transient	37
Total	114

Table 1.4: The final result for $\tilde{\omega}'_p$ of the average over all data sets in Run 1 [13].

to produce better shimming measurements, better temperature control, and better alignment between the trolley and plunging probe. For the NMR probes frequency extraction methods, a new fit window optimization method was applied to improve the bad probes (short FID probes) resolutions and upgrade DQC and production campaigns. For interpolation, there are two blinded analyses conducted with two teams: Purcell [16] and Bloch [17]. These analyses also improved beyond the Run 1 analysis. For example, the Bloch analysis transitioned to a python based framework that used a different magnetic footprint removal algorithm, and more [18]. In addition, since the measurements depended highly on the temperature, we upgraded the experimental hall cooling system to keep the temperature as constant as possible. For the kicker transient, the kickers were upgraded to deflect the beam closer to the ideal orbit. Lastly, the field team improved the mapping of the perturbed magnetic field results from ESQ transient to reduce uncertainties, which is the dominant error of field measurement uncertainties.

In the dissertation, I will briefly introduce the muon g-2 theory. Then, I will introduce the experimental overview (Chapter 3) and how E989 is possible to measure a_μ with high precision (Chapter 3). After an overview of both the theory (Chapter 2) and experimental of muon g-2 (Chapter 3), I will mainly discuss my contributions (Chapter 6, Chapter 7, Chapter 8, and Chapter 9) to the experiment to improve the magnetic field measurement uncertainty for Run-2/3 and beyond Run 3 to reach the goal of a four-fold reduction in uncertainty.

2

Theory: The Calculation of g-2

As discussed in the previous chapter, the g-factor of the muon, g_μ, is the quantity connecting spin, $\vec{s}$, to its magnetic moment, $\vec{\mu}$. $\vec{\mu}$ connecting to $\vec{s}$ is expressed as [1]:

$$\vec{\mu} = g_\mu \frac{q}{2m_\mu}\vec{s}, \tag{2.1}$$

where q is a charge of the muon and m_μ is the mass of the muon. In the Dirac equation, g is equal to 2 for a spin-1/2 particle. However, there are other contributions to modifying the g-factor which ends up being slightly larger than 2. The correction from the contributions to the Dirac equation in the Standard Model (SM) is called the anomalous magnetic moment, a_μ. The SM prediction of a_μ is determined from the sum of all sectors of the SM contributions:

$$a_\mu^{\mathrm{SM}} = a_\mu^{\mathrm{QED}} + a_\mu^{\mathrm{EW}} + a_\mu^{\mathrm{HVP}} + a_\mu^{\mathrm{HLBL}}, \tag{2.2}$$

where a_μ^{QED} is quantum electrodynamics (QED) contributions, a_μ^{EW} is electroweak (EW) contributions, a_μ^{HVP} is the hadronic vacuum polarization (HVP) contributions, and a_μ^{HLBL} is the hadronic light-by-light scattering contributions [14]. Feyman diagrams of each of the contributions are shown in Fig 2.1 and the value and uncertainty

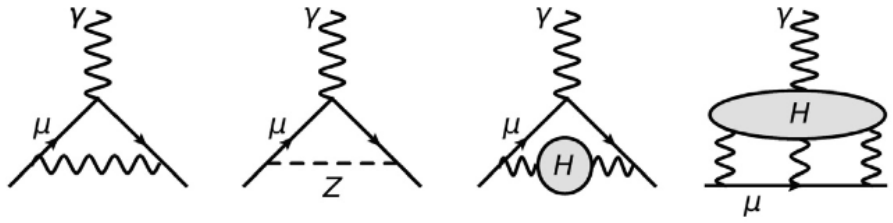

FIGURE 2.1: Leading Feynman diagrams of contributions by the fundamental SM interactions to a_μ. From left to right, the first one is the one-loop QED diagram. The next one is the one-loop EW involving Z-boson exchange. The last two are the leading order HVP diagram and HLBL diagram [14].

a_μ term	Value (x 10^{11})	Uncertainty
QED	116 584 718.931	0.104
EW	153.6	1.0
HVP	6 845	40
HLBL	92	18
Total	116 591 810	43

Table 2.1: Values and uncertainties of SM contributions to a_μ.

per each contribution are shown in Table 2. Hadronic contributions have the most dominant factor on the total uncertainty because of the non-perturbative nature of the low energy strong interaction. In this chapter, I will discuss the contributions from equation 2.2 to a_μ in the SM prediction in more detail. Moreover, I will briefly discuss the beyond SM (BSM).

2.1 The QED contributions

The QED contributions to a_μ include all contributions from leptons and photons alone, and have been calculated up to a five-loop order. Because all contributions are from leptons and photons alone, the QED contribution calculation can be measured with high precision. The full five-loop QED Feynman Diagram has a total of 12,672 Feynman diagrams and a few of them are shown in Fig 2.2. All contributions up to a

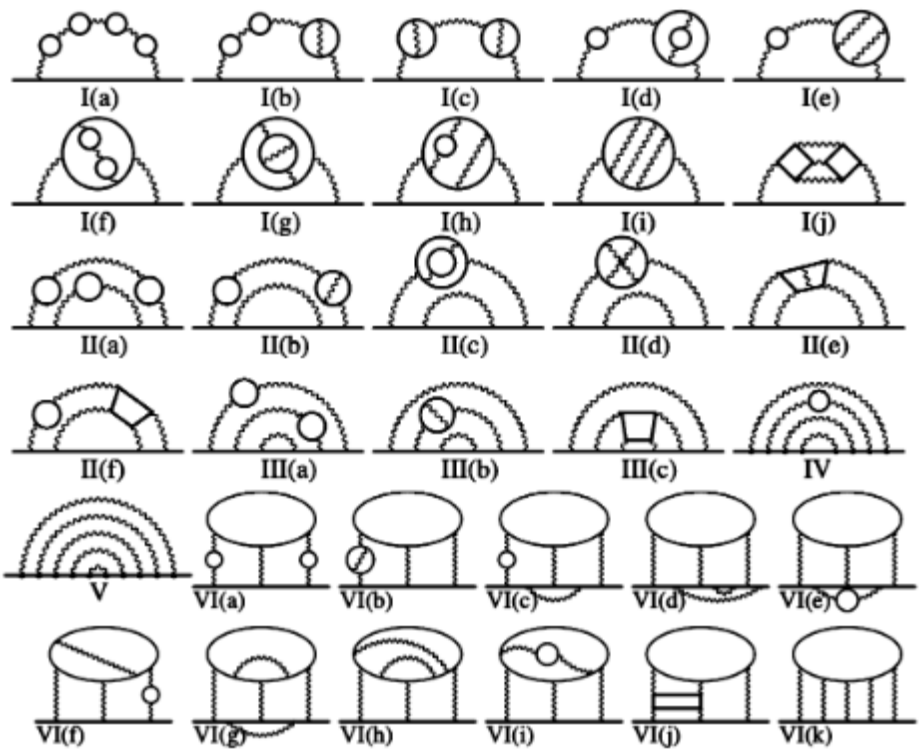

FIGURE 2.2: The full five-loop QED Feynman Diagram. The figure is reprinted from [6].

four-loop have been determined and verified by different groups from both numerical and analytical calculations [14]. The QED contribution is found to be [6]

$$a_\mu^{\mathrm{QED}} = 116\ 584\ 718.931\ (104) \times 10^{-11}. \tag{2.3}$$

2.2 The EW Contributions

The EW contributions contain at least one EW boson (W, Z, or Higg). The EW contributions to electron g-2 are enormously suppressed because of the mass of an electron. Because muons are about 207 times heavier than electrons, these contributions affect muon g-2 calculations more than electron g-2 calculations. The contributions have been calculated up to a two-loop, and the three-loop contributions have been

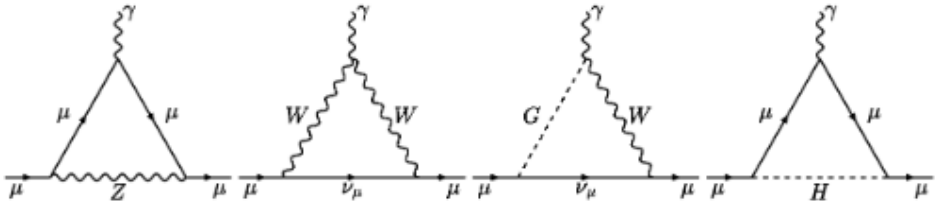

FIGURE 2.3: One-loop EW Feynman Diagram. The figure is reprinted from [7].

estimated [19]. The value of the EW contributions are found [7]

$$a_\mu^{\mathrm{EW}} = 153.6(1.0) \times 10^{-11}. \tag{2.4}$$

2.3 The HVP Contributions

HVP is an effect of polarization by fluctuations involving stronger interacting particles in the vacuum. In general, the HVP contributions are calculated from data-driven approaches or Lattice quantum chromodynamics (QCD). The HVP contributions from data-driven approaches can be evaluated from all available $e^+e^- \rightarrow$ hadrons cross-section data. The leading order (LO) HVP contribution is evaluated by dispersion relations and from integral over QCD kernel weight function, $K(s)$:

$$a_\mu^{\mathrm{LO,\ HVP}} = \frac{1}{4\pi^3} \int_{m_{\pi^2}^2}^{\infty} ds K(s) \sigma_{\mathrm{had}}(s), \tag{2.5}$$

where $\sigma_{\mathrm{had}}(s)$ is the normalized e^+e^- cross-section. About 92 % of the contributions to equation 2.5 comes from the low-energy region below $\sqrt{s} = 1.84$ GeV [20]. The process at LO is shown in Fig 2.4. The e^+e^- annihilation is due to the leptonic initial state and the exchange of a highly virtual photon coupled to any charged particle. This leads the strong interaction dynamic studies in a way as quark pairs are created initially out of QCD vacuum [7]. The leading order (LO) and next leading order (NLO) contributions to a_μ are shown in Fig 2.6. The analysis involves combining

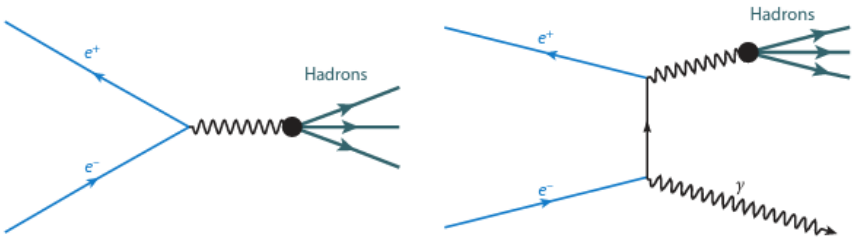

FIGURE 2.4: The LO Feynman diagram for the annihilation processes $e^+e^- \rightarrow$ hadrons (left) and $e^+e^- \rightarrow \gamma +$ hadrons with ISR (right). Reprinted from the reference [7].

FIGURE 2.5: Feynman diagram of the most dominant channel (more than 70 %) of the total HVP contributions.

all available $e^+e^- \rightarrow$ hadrons cross-section measurements for more than 35 exclusive hadronic channels from different experiments, as shown in Fig 2.7 [14]. The most dominant channel, more than 70 % of the total HVP contributions, is the two pion channel and is shown in Fig 2.5. From combinations of all different channels of data-driven experiments, the HVP contributions include $a_\mu^{\mathrm{LO,HVP}}$ [7], $a_\mu^{\mathrm{NLO,HVP}}$ [21], and $a_\mu^{\mathrm{NNLO,HVP}}$ [22] and the values of corresponding contributions are

$$\begin{aligned} a_\mu^{\mathrm{LO,HVP}} &= 6931(40) \times 10^{-11}, \\ a_\mu^{\mathrm{NLO,HVP}} &= -98.3(7) \times 10^{-11}, \\ a_\mu^{\mathrm{NNLO,HVP}} &= 12.4(1) \times 10^{-11}. \end{aligned} \tag{2.6}$$

Combining all values from values from equation 2.6, the total HVP estimation is [7]

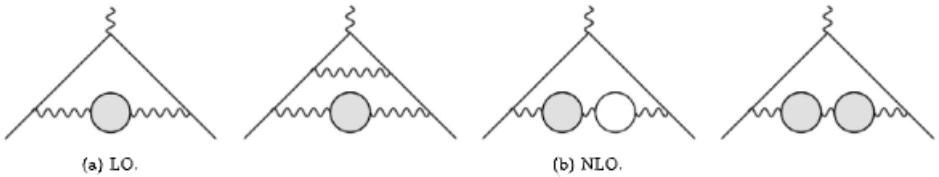

FIGURE 2.6: HVP Feynman Diagram at LO (a) and NLO (b). The grey circle represents hadronic and the white circle represents leptonic VP. The figure is reprinted from [14].

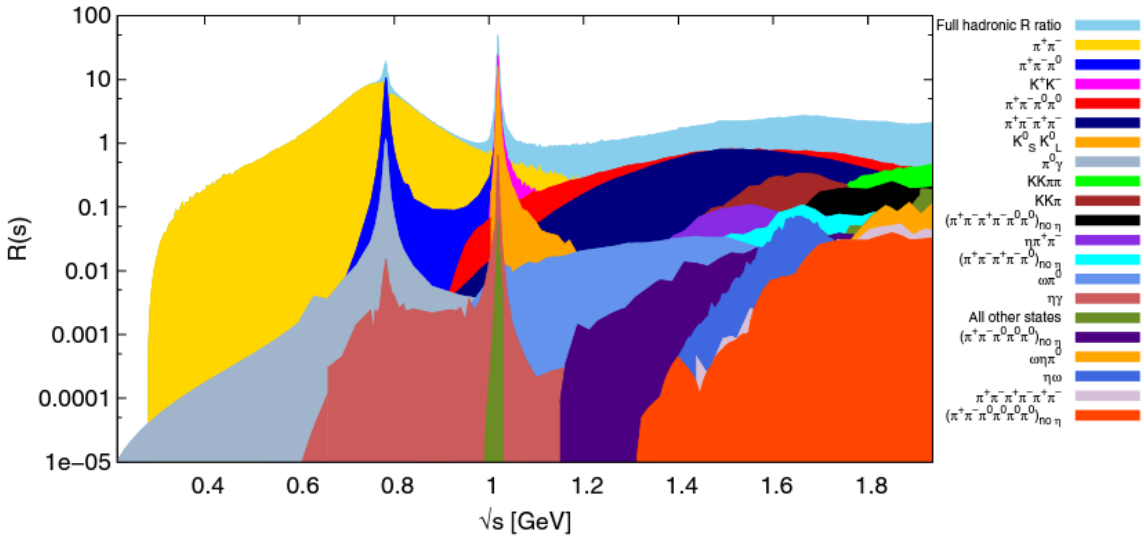

FIGURE 2.7: Contributions to the total hadronic cross-section. The figure is reprinted from [23].

$$a_\mu^{\mathrm{HVP}} = 6845(40) \times 10^{-11}. \tag{2.7}$$

The new CMD-3 result was published in February 2023. The cross-section of the process $e^+e^- \rightarrow \pi^+\pi^-$ has been measured in the center of the mass-energy that ranges from 0.32 to 1.2 GeV with the CMD-3 detector at the electron-positron collider VEPP- 2000 [24].

2.4 The HLBL Contributions

One of the largest uncertainties of SM prediction of a_μ comes from the HLBL scattering contributions. The HLBL scattering contributions, shown in Fig 2.8 and in the last diagram of Fig 2.1, describe the process of an external soft and on-sell photon interactions through a hadronic blob (the shaded blob in the diagram) with three off-shell photons that then coupled to the muon [14]. This contribution cannot be calculated in the perturbation theory and can only be relied on either lattice QCD or data-driven evaluations similar to calculations of HVP contributions. However, the calculation of HLBL contributions is more complicated than those of HVP contributions (the two-point function) because HLBL contributions are classified by a four-point function. Fig 2.9 shows various contributions to the HLBL tensor. These contributions are from single mesons (π^0, η, η', $f_0(980)$, $a_0(980)$), axial-vector mesons (a_1, f_1), tensor mesons (a_2, f_2), and charged pion or kaon loops [14]. Unlike HVP calculations, we cannot sum over all possible intermediate states at once due to the complexity of the analytic structure of the four-point function. Thus, we consider individual intermediate states and for each of these states, construct a relationship between the double spectral function, physical observables, and cross-sections involving on-shell hadrons. In this framework, the unitarity relation is able to contribute to $a_\mu^{\rm HLBL}$ intermediate states in direct and crossed channels shown in Fig 2.10. The figure shows intermediate states in the direct channel for HLBL scattering of one-particle and two-particle cuts [7]. The HLBL tensor unambiguously split the sum of all intermediate states in direct and crossed channels as:

$$\Pi_{\mu\nu\lambda\sigma} = \Pi_{\mu\nu\lambda\sigma}^{\pi^0-\text{pole}} + \Pi_{\mu\nu\lambda\sigma}^{\pi-\text{box}} + \Pi_{\mu\nu\lambda\sigma}^{\pi\pi} + ... \tag{2.8}$$

Within this framework, $a_\mu^{\rm HLBL}$ can be written as:

$$a_\mu^{\rm HLBL} = a_\mu^{\pi^0-\text{pole}} + a_\mu^{\pi-\text{box}} + a_\mu^{\pi\pi} + ... \tag{2.9}$$

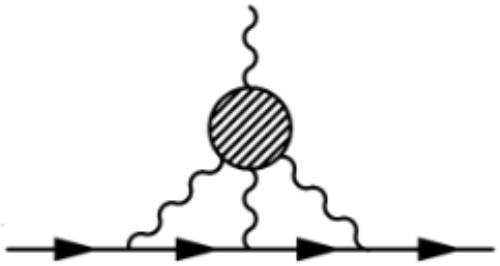

FIGURE 2.8: HLBL Feynman Diagram at LO. The shaded blob represents all possible intermediate hadronic states. The figure is reprinted from [25].

where $a_\mu^{\pi^0-\text{pole}}$ is from the exchange of $a_\mu^{\pi^0}$ in one of channels, $a_\mu^{\pi-\text{box}}$ has two-pion discontinuities in two channels (shown in diagram (a) of Fig 2.11), and $a_\mu^{\pi\pi}$ is two-pion cut only in one of the three channels (shown in diagram (b) and (c) of Fig 2.11) [7]. a_μ^{HLBL} is dominated by contributions below 1.5 GeV with the dominant contribution, π^0-pole, while other single-particle states (η and η') are suppressed. Detailed descriptions of the disperse calculations and experimental inputs of each of the various contributions to a_μ^{HLBL} can be found in the white paper [7]. The results of these calculations are shown in Table 2.4. The sum of dispersive estimations for the full HLBL scattering contributions is

$$a_\mu^{\text{HLBL}} = 92(19) \times 10^{-11}, \tag{2.10}$$

where the overall uncertainty is from a sum of data-driven errors and model-dependent errors.

2.5 Lattice QCD

In this section, I will briefly discuss the status of lattice QCD calculations of the HVP contributions and the HLBL scattering contributions to the anomalous muon magnetic moment, a_μ.

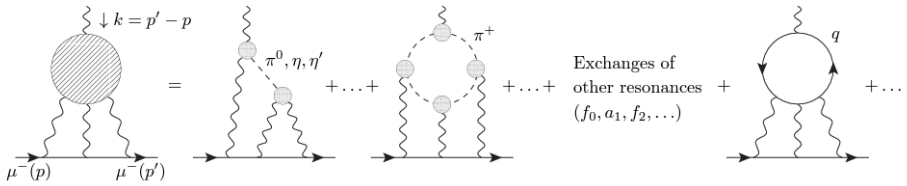

FIGURE 2.9: HLBL in the muon g-2 in model. The right side of the equal sign describes the interaction of photons with hadrons. Reprinted from the reference [7].

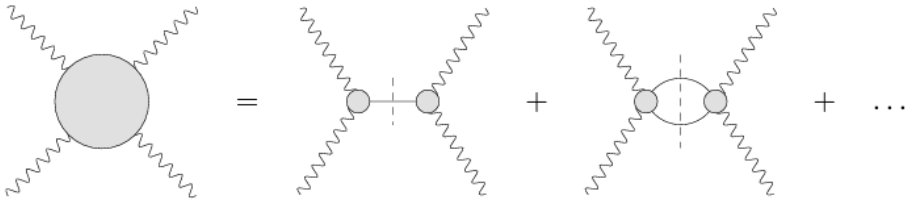

FIGURE 2.10: Intermediate state in the direct channel for HLBL scattering: one- and two-particle cuts. Reprinted from the reference [7].

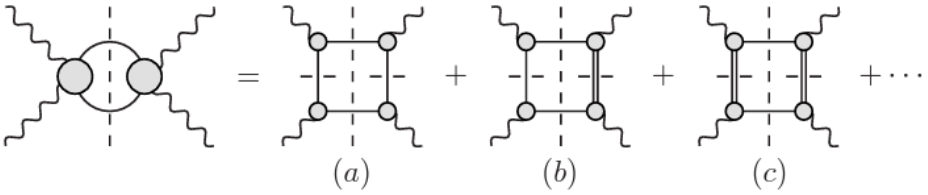

FIGURE 2.11: Two-pion cut contributions to HLBL scattering. Solid lines represent pions and wiggly lines represent photons. Double lines represent heavier intermediate states. Reprinted from the reference [7].

Contributions	PdRV(09) [26]	N/JN(09) [27] [28]	J(17) [29]	Dispersive [7]
π^0, η, η'-poles	114(13)	99(16)	95.45 (12.40)	93.8(4.0)
π, K-loop/boxes	-19(19)	-19(13)	-20(5)	-16.4(2)
S-wave $\pi\pi$ rescattering	-7(7)	-7(2)	-5.98(1.20)	-8(1)
subtotal	88(24)	73(21)	69.5(13.4)	69.4(4.1)
axial vectors	15(10)	22(5)	7.55(2.71)	6(6)
u, d, s-loop/short-distance	-	21(3)	20(4)	15(10)
c-loop	2.3	-	2.3(2)	3(1)
Total	105(26)	116(39)	100.4(28.2)	92(19)

Table 2.2: Results from various contributions to $a_\mu^{\rm HLBL}$ in unit of 10^{-11}. Table is reprinted from [14].

2.5.1 HVP from lattice QCD

HVP contribution is determined by applying Euclidean space-time discretization of vacuum polarization tensor $\Pi_{\mu\nu}(Q^2)$ for spacelike Q^2 in finite volumes and with finite lattice spacing. Then, it is taken to continuum and infinite-volume limits. Depending on the individual analysis groups, the intermediate steps of these calculations can be performed in different order and resulted in different results. The calculation of $a_\mu^{\rm LO,\ HVP}$ at $O(\alpha^2)$, according to quark-connected (conn) and quark-disconnected (disk) contribution, is determined as,

$$a_\mu^{\rm LO,\ HVP}(\alpha^2) = a_{\mu,\rm conn}^{\rm LO,\ HVP} + a_{\mu,\rm disc}^{\rm LO,\ HVP}. \tag{2.11}$$

The quark flavor-connected contribution, $a_{\mu,\rm conn}^{\rm LO,\ HVP}$, can be expressed as:

$$a_{\mu,\rm conn}^{\rm LO,\ HVP} = a_\mu^{\rm LO,\ HVP}(ud) + a_\mu^{\rm LO,\ HVP}(s) + a_\mu^{\rm LO,\ HVP}(c) + a_\mu^{\rm LO,\ HVP}(b), \tag{2.12}$$

where ud is the contributions of light u and d quarks, and s, c, and b are strange, charm, and bottom quarks contributions. The recent process in lattice determination of $a_\mu^{\rm LO,\ HVP}(\alpha^2)$ is necessary to add strong and electromagnetic isospin-breaking (IB) corrections, $\delta a_\mu^{\rm LO,\ HVP}$, because equation 2.11 do not include effects from the electric charges of the quarks [7]. Then, the total LO of HVP contribution, $a_\mu^{\rm LO,\ HVP}$, is given by,

$$a_\mu^{\rm LO,\ HVP} = a_\mu^{\rm LO,\ HVP}(\alpha^2) + \delta a_\mu^{\rm LO,\ HVP}, \tag{2.13}$$

Collaboration	$a_\mu^{\mathrm{LO,\ HVP}}(ud)$	$a_\mu^{\mathrm{LO,\ HVP}}(s)$	$a_\mu^{\mathrm{LO,\ HVP}}(c)$	$a_{\mu,\mathrm{disc}}^{\mathrm{LO,\ HVP}}$	$a_\mu^{\mathrm{LO,\ HVP}}$
LM-20 [30]	657(29)	52.8(7)	14.3(7)	11.2(4.0)	714 (30)
BMW-20 [31]	633.7(4.7)	53.4(1)	14.6(1)	18.6(2.0)	707.5 (5.5)
ETM-18/19 [32] [33]	629.1(13.7)	53.1(2.6)	14.75(56)	-	692.1 (16.3)
Mainz/CLS-19 [34]	674(13)	54.5(2.5)	14.66(45)	23.2(5.0)	720.0 (15.9)
FHM-19 [35] [36]	637.8(8.8)	-	-	13(5)	699 (15)
PACS-19[37]	673(14)	52.1(5)	11.7(1.6)	-	737 $\binom{+15}{-20}$
RBC/UKQCD-18 [38]	649.7(15.0)	53.2(5)	14.3(7)	11.2(4.0)	717.4 (18.7)
BMW-17 [39]	647.6(19.2)	53.73(49)	14.74(16)	12.8(1.9)	711.1 (19.0)
Mainz/CLS-17 [40]	588.2(35.8)	51.1(1.7)	14.3(2)	-	654 $\binom{+38}{-39}$
HPQCD-16 [41]	599.0(12.5)	-	-	0(9)	667 (14)

Table 2.3: Lattice results for flavor (ud, s, c, disk) contributions and the total estimation of $a_\mu^{\mathrm{LO,\ HVP}}$. The results already include all corrections including $\delta a_\mu^{\mathrm{LO,\ HVP}}$ (not stated in the table). The errors in the table are statistical and systematic combined uncertainties in quadrature.

with

$$\delta a_\mu^{\mathrm{LO,\ HVP}} = \delta a_\mu^{\mathrm{LO,\ HVP}}(ud) + \delta a_\mu^{\mathrm{LO,\ HVP}}(s) + \delta a_\mu^{\mathrm{LO,\ HVP}}(c) + \delta a_{\mu,\mathrm{disc}}^{\mathrm{LO,\ HVP}}, \qquad (2.14)$$

where $\delta a_\mu^{\mathrm{LO,\ HVP}}(ud)$ includes both the strong and the QED IB corrections to the connected light-quark contribution, but $\delta a_\mu^{\mathrm{LO,\ HVP}}(s)$ and $\delta a_\mu^{\mathrm{LO,\ HVP}}(c)$ contain only QED effects of order of $O(\alpha^3)$. Results from different groups of the different flavor contributions and the total estimate of $a_\mu^{\mathrm{LO,\ HVP}}$ are shown in Table 2.5.1 [7]. From the results from various lattice groups combined with using a conservative procedure into an average of lattice, the total estimation of $a_\mu^{\mathrm{LO\ HVP}}$ is $711.6(18.4) \times 10^{-10}$ [14]. The major challenges in reducing the uncertainties are from these: the finite-volume effects, the exponentially growing signal-to-noise problems at large Euclidean times, disconnected contributions, and QED IB corrections [7].

2.5.2 HLBL from lattice QCD

In a perturbative framework for QED, the HLBL scattering contribution to a_μ in a lattice QCD calculation at the order of α^3 from the diagrams are shown in Fig 2.12 and Fig 2.13. Due to the effort of the Muon g-2 Theory Initiative [7], the

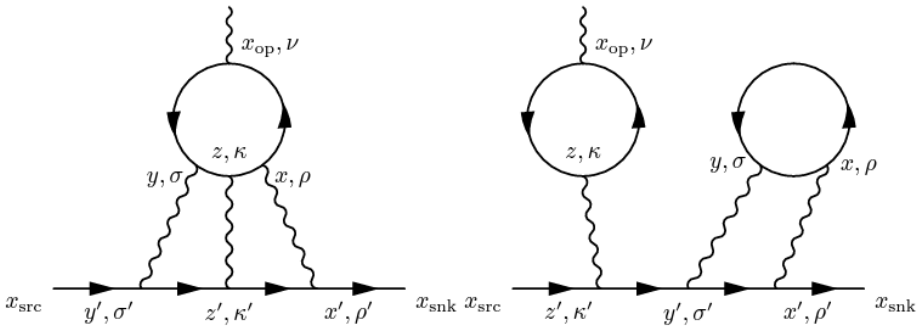

FIGURE 2.12: Diagrams contributing to HLBL scattering $O(\alpha^3)$: quark connection (left) and leading disconnection (right). Double lines represent heavier intermediate states. Reprinted from the reference [7].

full $a_\mu^{\rm HLBL}$ has now been calculated on the lattice by two groups: RBC and the Mainz group [42] [43]. In discretized Euclidean spacetime, $a_\mu^{\rm HLBL}$ has been computed treating QED both perturbatively and non-perturbatively, in both finite ($\rm QED_L$) and infinite volumes ($\rm QED_\infty$) [14]. In general, both approaches can be tested by replacing quark loops with lepton loops and the two groups cross-checking their results. More detailed derivations and the methodologies of the approaches can be found in the white paper [7]. After the infinite volume and continuum extrapolation, the RBC calculation result is [42]

$$a_\mu^{\rm HLBL} = 78.7(30.6)^{\rm stat}(17.7)^{\rm sys} \times 10^{-11}. \tag{2.15}$$

This calculation was performed for several lattice ensembles with different lattice spacing and volume and with all particles at their physical masses, including contributions from both connected and disconnected diagrams [14]. This result was recently available with the completed calculation of $a_\mu^{\rm HLBL}$. Recently, there are more recent calculations from the Mainz group available. We expected further improvement on full calculations of $a_\mu^{\rm HLBL}$ from both groups in the near future [14].

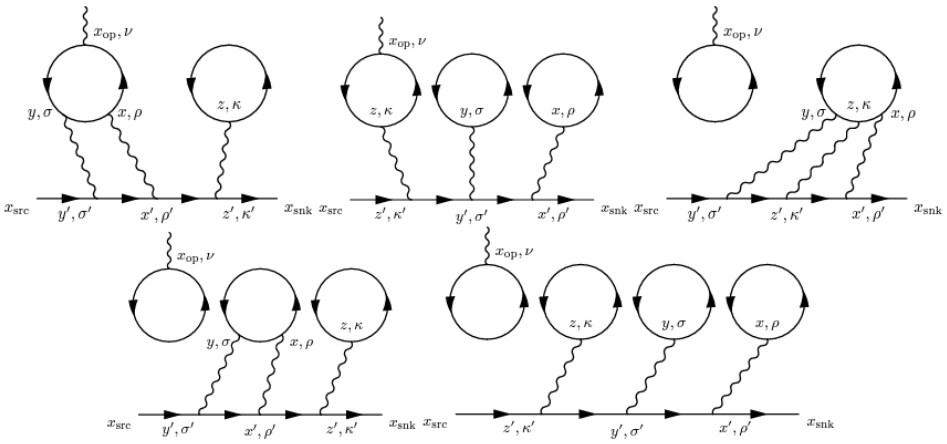

FIGURE 2.13: Sub-leading disconnected diagram contributing to HLBL scattering $O(\alpha^3)$. Double lines represent heavier intermediate states. Reprinted from the reference [7].

2.6 The SM prediction for a_μ

From all contributions that I discussed in previous sections, the SM prediction for a_μ can be determined by the summation of all contributions and is measured: [7]

$$a_\mu^{\rm SM} = 116\ 591\ 810(43) \times 10^{-11}\ (0.37\ \text{ppm}). \tag{2.16}$$

A summary of the contributions to $a_\mu^{\rm SM}$ is in Table 2.4.

Table 2.4: Summary of the contributions to $a_\mu^{\rm SM}$ from [14].

Contributions	Value (10^{-11})	Reference
HVP LO (e^+e^-)	6931(40)	[44] [45] [46] [47] [23] [21]
HVP NLO (e^+e^-)	-98.3(7)	[21]
HVP NNLO (e^+e^-)	12.4(1)	[22]
HVP LO (lattice, *udsc*)	7116(184)	[25] [38] [39] [36] [35] [34] [33] [37]
HLBL (phenomenology)	92(19)	[48] [49] [50] [51] [29] [52] [53] [54] [55]
HLBL NLO (phenomenology)	2(1)	[56]
HLBL (lattice, *uds*)	79(35)	[42]
HLBL (phenomenology + lattice)	90(17)	[48] [49] [50] [51] [29] [52] [53] [54] [55]
QED	116 584 718.931(104)	[6] [57]
EW	153.6(1.0)	[7] [19]
HVP (e^+e^-, LO + NLO + NNLO)	6845(40)	-
HLBL (phenomenology + lattice + NLO)	92(18)	-
Total SM Prediction Values	116 591 810(43)	-

2.7 Beyond the Standard Model

The first result from the Fermilab E989 muon g-2 experiment resulted in 4.2 σ discrepancy to the SM prediction, a_μ^{SM} [12]. Assuming that both experimental determination of a_μ and the SM prediction calculation of a_μ^{SM} are evaluated correctly with accurate uncertainty estimates, new ***Beyond Standard Model*** (BSM) physics must have existed to explain the discrepancy. In this section, an overview of several possible BSM models will be introduced. For a more detailed discussion of BSM constraints related to Δa_μ, the review paper can be found in [58].

BSM contributions to a_μ can be expressed as

$$\Delta a_\mu^{\mathrm{BSM}}\ C\frac{m_\mu^2}{\Lambda^2}, \tag{2.17}$$

where m_μ is the mass of muon, Λ is the mass scale of new physics, and C is the coefficient that depends on the models.

One of the possible appealing models is called **Supersymmetry** (SUSY), the virtual-loop interaction of the muon with the SUSY particle. The SUSY contributions to a_μ are from smuon-neutralino, sneutrino-chargino, and potential slepton mixing. The sample diagram is shown in Fig 2.14 [59]. In general, it was shown that the continued lack of evidence for BSM physics from the LHC and dark matter searches has greatly restricted the SUSY parameter space and implied mass patterns [14].

Other models that have been proposed to explain Δa_μ are **Alternative Higgs Models** [61][62] and the **Dark Sector**, such as dark photons[63] or dark boson [64][65]. However, all the models do not fully explain the discrepancy of Δa_μ.

The discrepancy between the experimental and theoretical outcomes of a_μ strongly motivates many scientists to explore NP and BSM. Many fascinating potential models are studied for NP and BSM up to now.

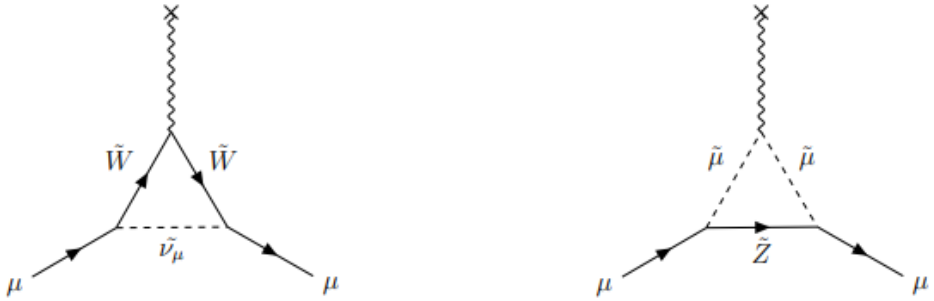

(a) Sneutrino-wino loop

(b) Smuon-neutralino loop

FIGURE 2.14: Sample SUSY Feynman Diagram. The figure is reprinted from [60]

.

3

E989 Experiment Overview

This chapter provides an overview of the E989 muon g-2 experiment in Fermilab. First, I will talk about the anomalous precession frequency, ω_a, and discuss the muon decay and how muons are produced. Then, I will explain the muon injection to the storage ring. There will be a section about the storage ring with an explanation in detail about the components of the storage ring. Components of the storage ring are crucial factors to shim and maintain the stable uniform magnetic field of the storage ring. To measure the magnetic field, there are different kinds of measurement probes. Detailed explanations of the magnetic field measurement will be in Chapter 4. Once we measured the magnetic field, we used the detectors to measure the spin precession of the muon from the number of positrons above the threshold decay as a function of time.

Here are the stages of the E989 experiment:

1. Muon particles are produced in Fermilab.
2. Muon beam is sent to the muon g-2 magnetic storage ring at MC-1.
3. Muon beam is injected and circulated in the storage ring.

4. Muon particles precess and decay to positron.

Further details can be found in the technical design report [15].

3.1 The Anomalous Precession Frequency, ω_a

In order to determine a_μ, the anomalous precession frequency, ω_a needs to be measured. ω_a is defined as the difference between the spin precession frequency, ω_s, and the cyclotron frequency ω_c. In the Dirac equation, when the g-factor is equal to 2, ω_s and ω_c are the same and there will be no precession frequency. However, since the g-factor is slightly larger than 2, ω_a is not 0. As an equation, ω_a relative to its momentum in the lab frame is given

$$\begin{aligned} \omega_a &= \omega_S - \omega_C \\ &= \frac{q}{m_\mu}[-a_\mu \vec{B} + a_\mu \frac{\gamma}{\gamma+1}(\vec{\beta}\cdot\vec{B})\vec{\beta} + (a_\mu - \frac{1}{\gamma^2-1})\frac{\vec{\beta}\times\vec{E}}{c}], \end{aligned} \tag{3.1}$$

where γ is the Lorentz factor, and $\vec{\beta}$ is the velocity in speed-of-light units. In the absence of an electric field and in the limit of planar muon orbits, $\vec{\beta}\cdot\vec{B} = 0$, the equation 3.1 is simpler,

$$\omega_a = \frac{q}{m_\mu}[-a_\mu \vec{B} + (a_\mu - \frac{1}{\gamma^2-1})\frac{\vec{\beta}\times\vec{E}}{c}]. \tag{3.2}$$

There is a specific momentum called the magic momentum, $p_{\text{magic}} = 29.3$ ($p_\mu = 3.09$ GeV/c) where the second term vanishes, and the electric field does not contribute to the spin precession. However, realistically, not all muons can have magic momentum and there is a correction due to off-momentum muons. The requirement of p_{magic} dictates the value of 1.45 T for the storage ring magnetic field.

3.2 Muon Production and Beam Line

3.2.1 Muon Decay

Muons are unstable particles in nature, so muons decay with a lifetime of 2.2 μs. The experiment uses positive muons that decay into a positron and two neutrinos via left-handed couplings to the W-boson [66]:

$$\mu^+ \rightarrow e^+ v_e \bar{v}_\mu \tag{3.3}$$

Muons are produced from the primary channel of charged pion decays. The pion decays at rest into a muon and a muon neutrino [67]:

$$\pi^+ \rightarrow \mu^+ v_\mu \tag{3.4}$$

Because both of the decays proceed through the weak force, the decays are a parity violation. Fig 3.1 illustrates the parity violation of a positive muon decay at rest. Because pions are spin 0, μ^+ needs a left-handed helicity to conserve angular momentum. Therefore, parity violation provides the means for a direct measurement of the anomalous precession frequency: the highest energy positrons from the muon decay are emitted at the rest frame in a direction strongly correlated with the muon spin direction. [68]

3.2.2 Muon Production and Beam Line

Fig 3.2 shows how the muons are produced and how they travel through each of the beam lines at Fermilab. Protons are accelerated in Linac and Booster up to 8 GeV and enter the Recycler. In the Recycler, one bunched proton beam (4×10^{12} intensity) is re-bunched into four bunches (1×10^{12} intensity) in order to satisfy the limitations of the beam for the detector DAQ systems. Then, the beam is transported to P1, P2, and M1 to a target at AP0 target hall. Positive particles with a momentum of 3.11 GeV/c are delivered to M2 and M3 lines to capture as many muons as possible with

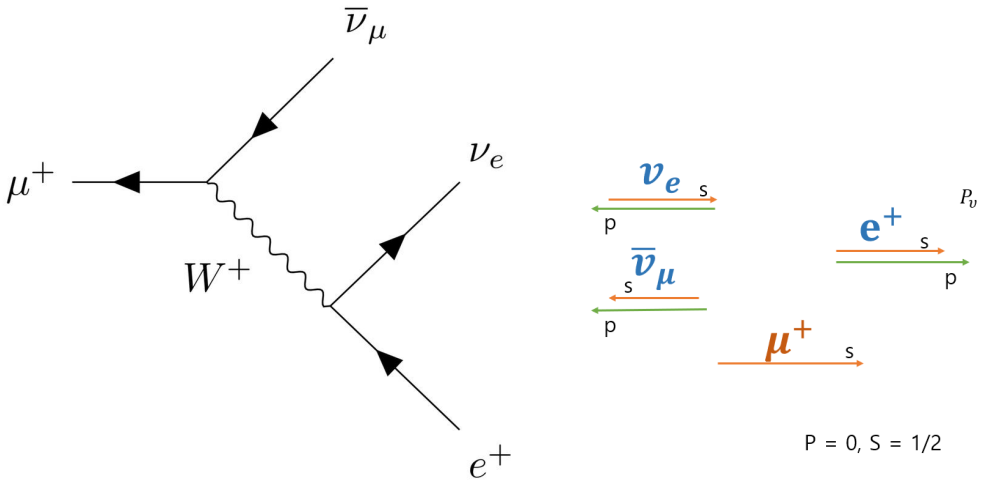

FIGURE 3.1: Left diagram is the Feynman diagram for the decay of a positive muon. The right diagram is a schematic helicity diagram of the muon decay at the Michel positron energy endpoint. Orange arrows indicate spin and green arrows indicate momentum.

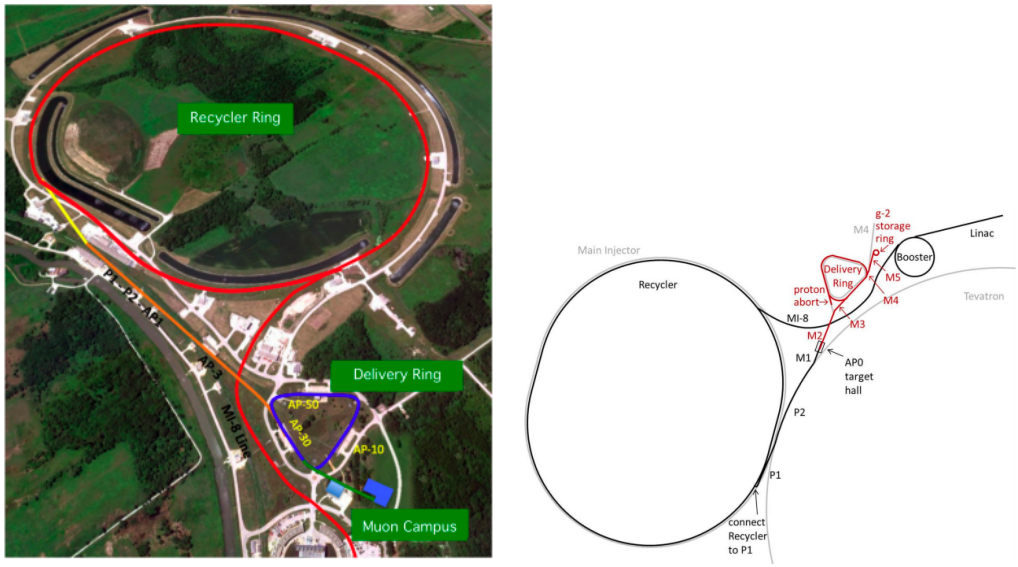

FIGURE 3.2: The diagram is the beamline to muon g-2 campus reproduced from [15]. Protons travel on black lines and muons travel on red lines.

a momentum of 3.094 GeV/c from the pion decay. Then, the beam is injected into the Delivery Ring for the remaining pion to be decayed into muons and separated from the remaining heavier protons. Lastly, the beam goes through M4 and M5 and finally arrives at the muon g-2 storage ring. [15]

3.3 The magnetic Storage Ring

In order to have a precise measurement of the magnetic field and the magnetic moment of the muon, the field should be as uniform as possible with a 1.45 T magnetic field at the center. The g-2 magnetic storage ring (SR) at Fermilab is the same SR that was used for the E821 BNL g-2 experiment which was transported from Brookhaven to Fermilab. Fig 3.3 shows the SR cross-section and the current and magnetic field directions with red markers and green arrows.

The SR is one superconducting magnet that consists of 12 with approximately 14 m diameter C- shape iron yokes to return the magnetic flux generated by three superconducting NbTi/Cu coils. There are 72 poles, 864 wedges, and 24 iron top hats to shim the field uniformly. There are six poles, 3 on top and 3 on the bottom, per yoke. The main poles provide a dipole component of the field. Iron top hats are located on the top and bottom of the yoke and affect the dipole with 30°azimuthal range. Wedges are additional shimming tools that can translate radially inwards or outwards to affect the dipole, quadrupole, and sextupole with 10°azimuthal range. In addition to the passive shimming tools, there is one active shimming tool. The active shimming tool is the surface coils that can shim the azimuthal average field during the experiment dynamically. Table 3.1 gives the values of parameters of the magnet [15].

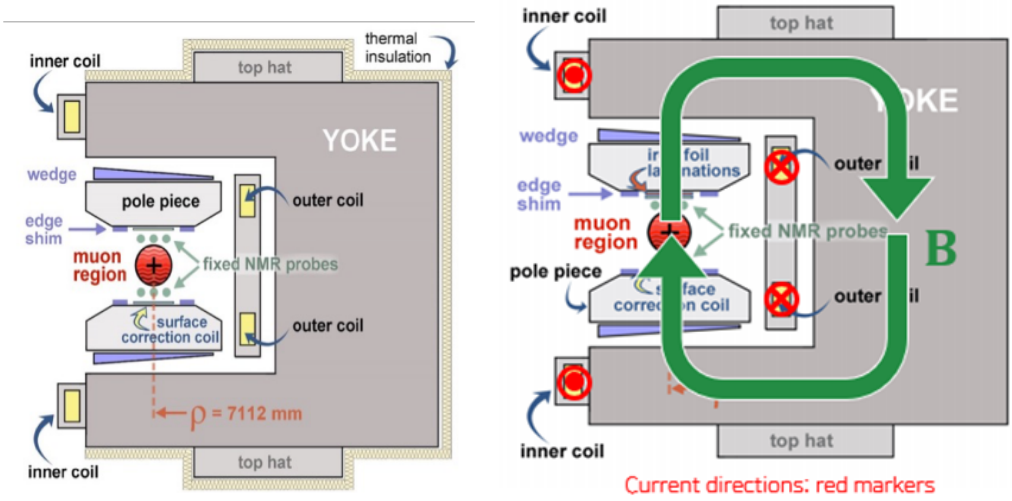

FIGURE 3.3: Both diagrams are cross section of the g-2 magnetic storage ring. Right diagram also shows the direction of the current and magnetic field [13].

3.3.1 Muon Injection to the Storage Ring

The muon beam is delivered to the storage ring via the inflector magnet which is the device that cancels the magnetic field of the ring (1.45 T) for the beam to pass without deflection. Fig 3.4 shows how the beam enters the storage ring through the inflector. The injection beam line is set to a 1.25°angle from the tangential reference line. The reference line is 77 mm radially outward from the muon central orbit. The inflector has the current windings feature with a unique double-truncated cosine theta design to minimize the flux that leaks outside the inflector volume. Fig 3.5 shows the geometry at the inflector exit [11].

3.3.2 Kicker

As the muons exit the inflector and enter the storage ring, we need to correct 77 mm radially outward from the center of the orbit. Fig 3.6 shows how the muon beam enters the central orbit with the assistance of kicker plates. There are three separated 1.27- meter-long kicker magnets in a series which are located 90°clockwise from the

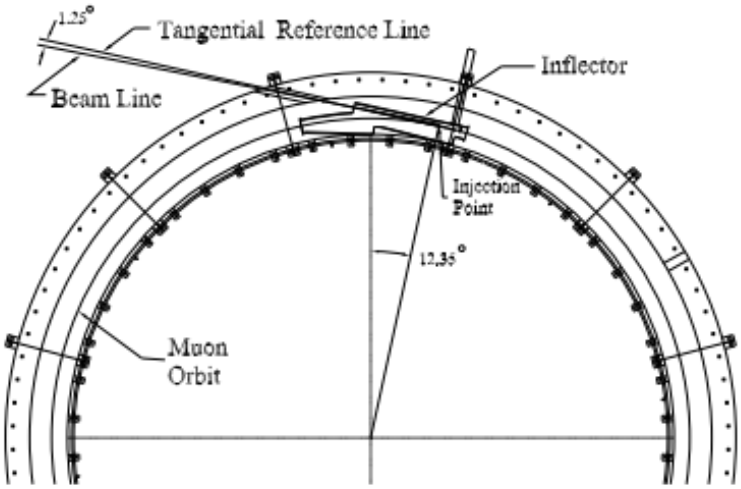

FIGURE 3.4: The diagram is the view of the beam entering the storage ring reproduced from [15].

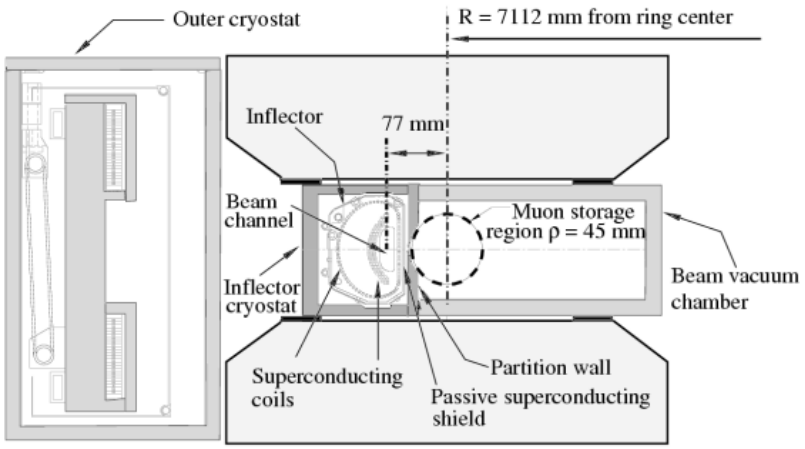

FIGURE 3.5: The inflector and storage ring geometry [15].

Table 3.1: Magnet parameters of the storage ring

Design Magnetic Field	1.451 T
Design current	5200 A
Equilibrium orbit radius	7112 mm
Muon storage region diameter	90 mm
Inner coil radius	6691 mm
Outer coil radius	7527.5 mm
Number of turns	48
Magnetic self inductance	0.48 H
He-cooled lead resistance	6 $\mu\Omega$
Yoke height	157 cm
Yoke width	139 cm
Pole width	56 cm
Iron mass	682 tons
Nominal gap between poles	18 cm

exit of the inflector [69].

3.3.3 Electrostatic Quadrupoles

The purpose of the electrostatic quadrupoles (ESQ) in the SR is to confine muons vertically. The vertical focus helps the muon not be lost after a few revolutions. Moreover, a procedure in the ESQ removes stored muons outside of the storage region. Ideally, the experiment wants to have the ESQ all around the ring, but it is not practical for technical reasons. Overall, the ESQ covers 43% of the total azimuthal range (360°) and maintains a fourfold symmetry around the SR. Fig 3.7 shows the locations of the kicker and the ESQ in the SR.

There are four ESQ around the ring and each ESQ consists of a short ESQ of 13°long and a long ESQ of 26°long. ESQ is installed inside a vacuum chamber to reduce the scattering of incident decay positrons. Q1, the first ESQ, has a slightly different design to avoid blocking the muon injection. Fig 3.8 shows the cross-section of the SR where the ESQ is installed with equipotential lines of the electric field.

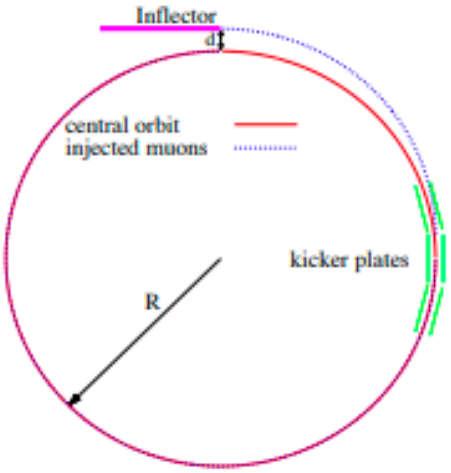

FIGURE 3.6: The diagram showed how muon beam from 77 mm off the central orbit to the ideal orbit with the assistance of kicker plates.

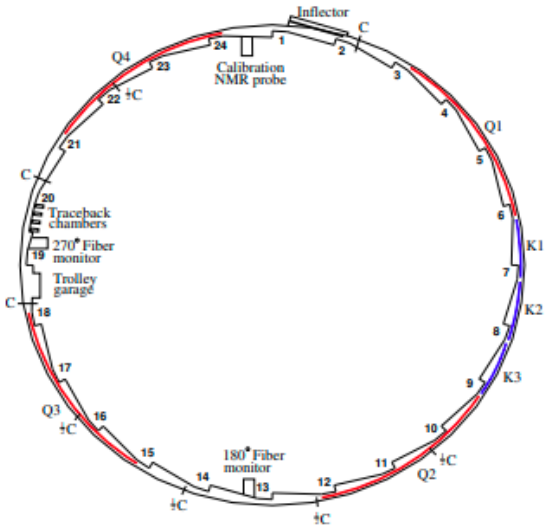

FIGURE 3.7: The diagram shows the location of inflector, kickers (K1-K3), and the electrostatic quadrupoles (Q1-Q4)

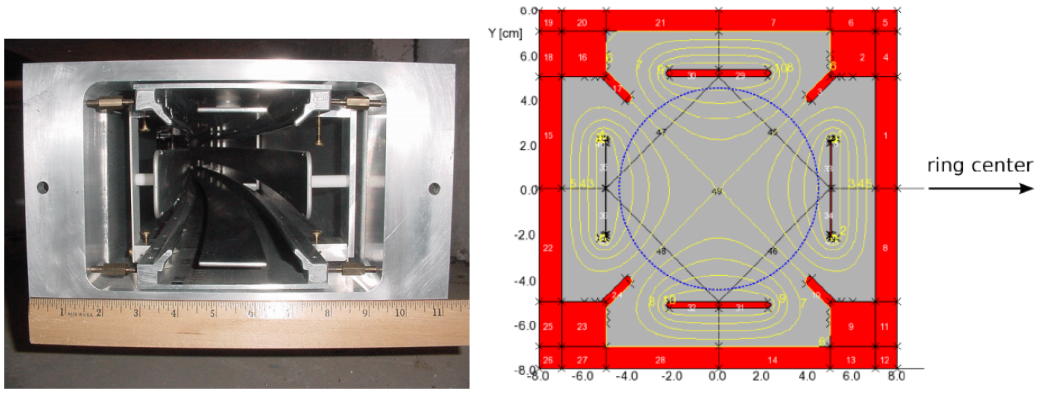

FIGURE 3.8: Left photo is the ESQ in the vacuum chamber in SR. The right diagram is the cross-section of the SR with ESQ. The yellow lines are for equipotential lines of the electric field and the blue circle represents the muon storage region (9 cm diameter)

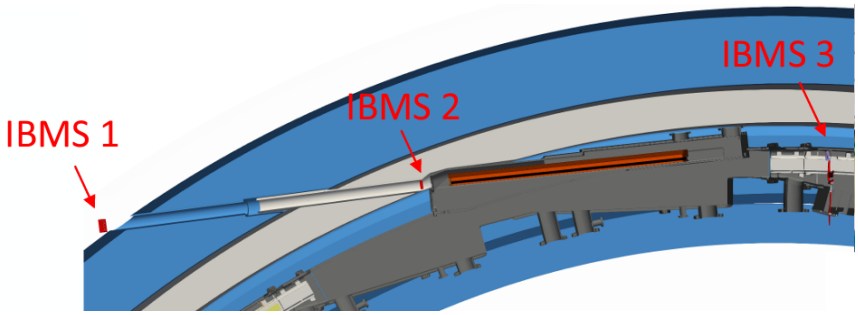

FIGURE 3.9: IBMS locations in inflector region.Orange is the inflector magnet on the diagram.

3.4 Detector System

There are various detector systems used in E989. In this section, I briefly explain the detector systems that we are using in the muon g-2 experiment at Fermilab.

3.4.1 T0 Counter and IBMS

T0 counter and the inflector beam monitoring systems (IBMS) are detectors for monitoring the injected beam. Both detectors are installed near the location of the inflector. Fig 3.9 shows the detailed locations of the IBMS near the inflector region.

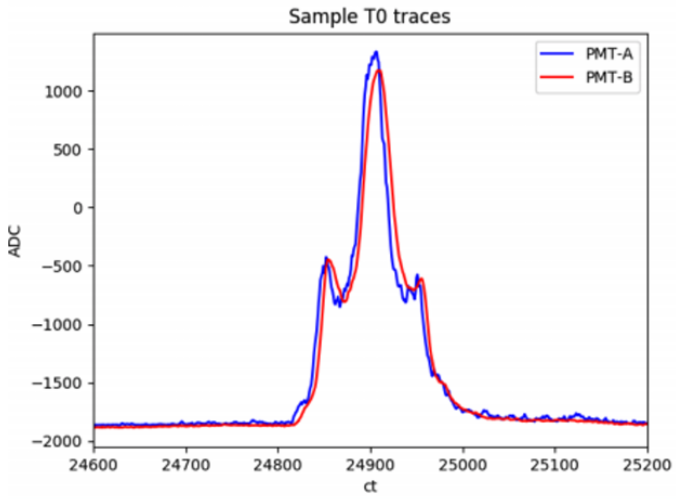

FIGURE 3.10: Sample T0 traces on monitoring system.

The T0 counter consists of a thin scintillator with 2 photomultiplier tube (PMT) readouts. It provides a beam time profile before the beam enters the storage ring. The sample T0 traces are shown in Fig 3.10.

The IBMS consists of 2 planes of scintillation fibers. The IBMS checks the beam injection characteristics: measuring the beam profile before and after the inflector. The sample IBMS monitoring plots are shown in Fig 3.11.

3.4.2 Fiber Harps

The fiber harps are strung with scintillating fibers that allow for a direct, but destructive, measurement of the distribution of stored muons and their associated beam dynamics parameters. It consists of a "harp" of seven scintillating fibers of 0.5 mm diameter, each 90 mm long, and separated from its neighbors by 13 mm [15]. Each scintillating fiber is further attached to a standard optical fiber shown in the left image of Fig 3.12. The right image of Fig 3.12 shows the horizontal measure in y of the beam profile. Maximum oscillations of the beam motion are in the center of the beam (around y =0). This is due to the vertical component of the betatron

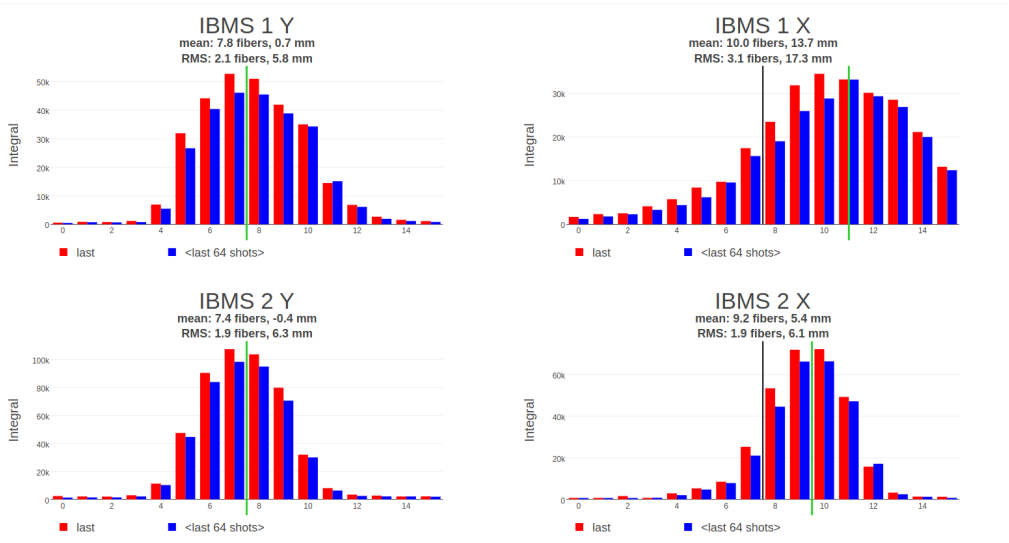

FIGURE 3.11: Sample IBMS plots on monitoring system.

oscillations [70].

3.4.3 Calorimeters and the Straw Tracker

The main detectors are calorimeters which measure the energy and time of arrival of the positrons from the muon decay. Fig 3.13 shows the locations of the calorimeters

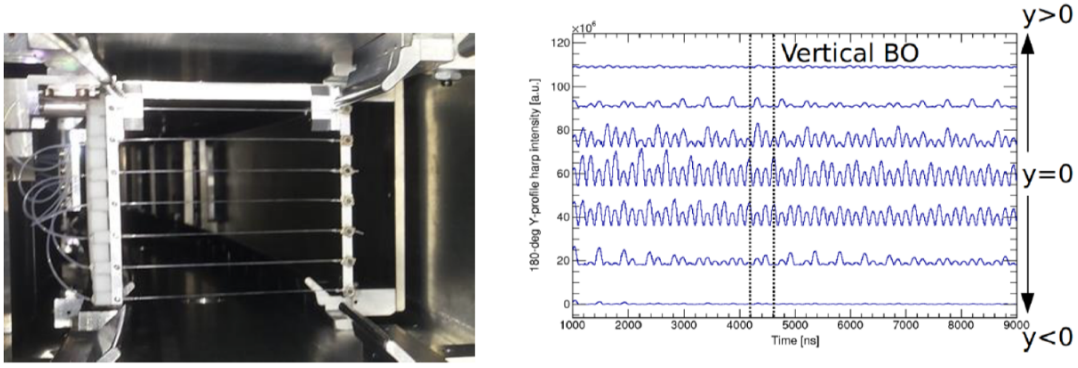

FIGURE 3.12: (Left) The image of a fiber harp; and (Right) the beam profile in y direction measured by the fiber harp. Vertical BO means the vertical component of the betatron oscillations [70].

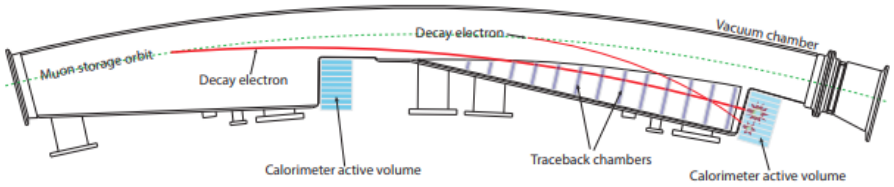

FIGURE 3.13: The diagram shows the locations of the calorimeters and trackers with one of 12 vacuum chamber segments. The red line represents the positron decay trajectory.

and trackers with one of the 12 vacuum chamber segments. Two decay positron trajectories are indicated to have high and low energy events. A total of 24 calorimeters are located that are evenly spaced around the SR. Each station contains 54 crystals for a total of 1296 individual PbF_2 crystals. Each crystal is read out by a silicon photomultiplier (SiPM). The detailed design and performance of SiPM-based readout of PbF_2 crystals can be found in reference [71].

The largest phase acceptance in Run 1 is from pileup, which refers to the overlap of events in the calorimeter from two different muon decay. When two pulses overlap, only one event with the sum of two pulses is detected. To minimize pileup, the calorimeter's response must be a few and the readout system must record information to enable the distinction between closely occurring pulse pairs. The energy resolution of 5% at 2 GeV is sufficient for the energy threshold.

In addition to calorimeters, there are tracking detectors called straw trackers which are designed to measure the muon beam profile at multiple locations around the ring as a function of time. Another physics goal of straw trackers is to understand the systematic uncertainties of the muon precession frequency measurement from the calorimeter data. The straw tracker stations are in front of the calorimeter stations 15, and 21 (180, and 270 degrees from the injection point respectively). Each station consists of 8 tracker modules and 128 straws. Fig 3.14 is a single tracker module in

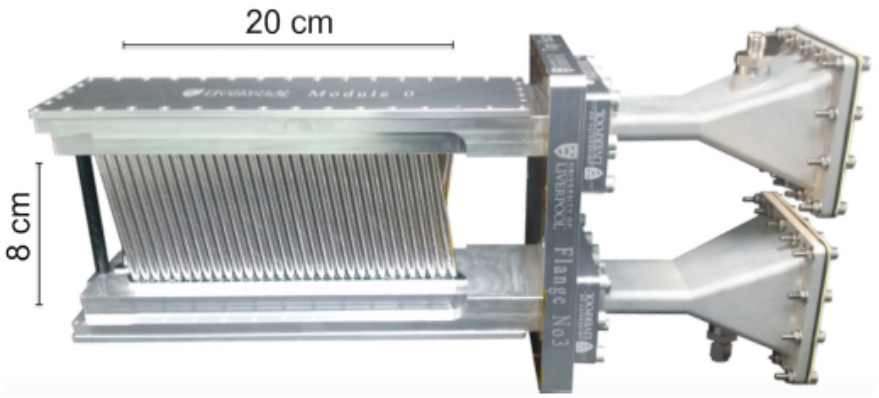

FIGURE 3.14: this picture is a single tracker module with 128 straws. A straw with a diameter of 5 mm is a chamber filled with Ar and Ethane, with a central anode wire at +1.65 kV.

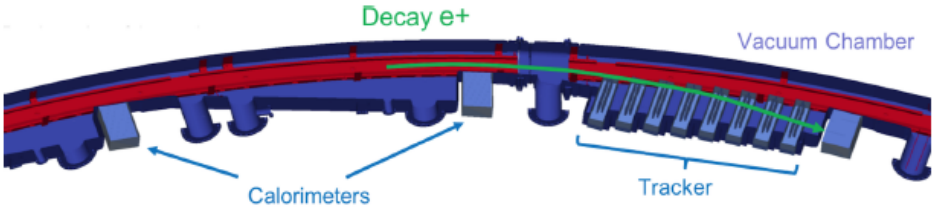

FIGURE 3.15: this diagram shows the tracker location in front of the calorimeter detectors on the inside of SR.

E989. Fig 3.15 shows where the tracker station is in the front of the calorimeter. Fig 3.16 shows the beam profile by using the extrapolated tracks and the decay arc length where higher momentum tracks originate further away from the detector.

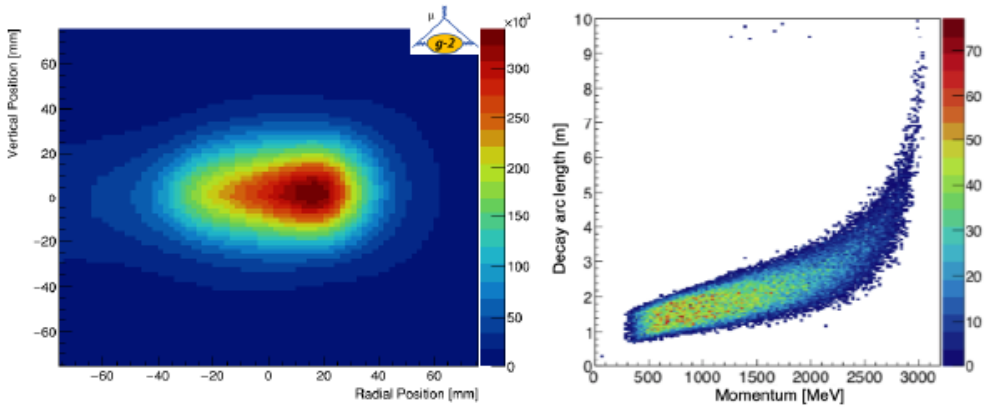

FIGURE 3.16: Left plot is from the reconstructed beam profile and the right plot is from the reconstructed decay arc length. Plots are from S. Charity [72]

4

Magnetic Field Measurement

4.1 Overview

In a highly uniform vertical magnetic field of 1.45 T, the muons circulate in the storage ring that has a mean radius of 7.112 m at a cyclotron frequency $\omega_c/(2\pi) =$ 6.7 MHz. The spin precession frequency $\omega_s/(2\pi)$ is slightly different from cyclotron frequency, and the difference between these two frequencies is called the anomalous precession frequency, a_a. Therefore, a_μ is (first introduced in Chapter 2)

$$\omega_a = \omega_s - \omega_c = -a_\mu \frac{q}{m_\mu}\mathbf{B}. \tag{4.1}$$

This equation shows that determining a_μ from ω_a requires a precise magnetic field measurement, $\mathbf{B}$. The average field over the muon distribution weighted by the detected decay over time is $\tilde{B}$. The frequency measurements determine $\tilde{B}$ which is formulated [13]

$$\tilde{B} = \frac{\bar{h}\tilde{\omega}'_p(T)}{2\mu'_p(T)} = \frac{\bar{h}\tilde{\omega}'_p(T)}{2}\frac{\mu_e(H)}{\mu'_p(T)}\frac{\mu_e}{\mu_e(H)}\frac{1}{\mu_e}. \tag{4.2}$$

$\mu_e(H)/\mu'_p(T)$ is the ratio of the magnetic moments of an electron bound in hydrogen to that of a proton shielded in a spherical water sample, measured to 10.5 ppb at

a water temperature $T_r = 34.7^\circ$ C[73]. $\mu_e(H)/\mu_e$ is the magnetic moment ratio of the electron bound in hydrogen versus a free electron and the electron magnetic momentum, μ_e, is known to 0.3 ppt [74]. Combining Equation 4.1,Equation 4.2, and $\mu_e = \frac{g_2}{2}\frac{e}{m_e}\frac{\bar{h}}{2}$, a_μ is expressed as,

$$a_\mu = \frac{\omega_a}{\tilde{\omega}'_p(T_r)}\frac{\mu'_p(T_r)}{\mu_e(H)}\frac{\mu_e(H)}{\mu_e}\frac{m_\mu}{m_e}\frac{g_e}{2}, \tag{4.3}$$

where the ratio of the mass of the muon and electron, m_μ/m_e, is measured to 22 ppb [74] [75] and the g factor of an electron, g_e, is measured to 0.13 ppt [5].

4.2 NMR Probes

NMR probes are used for magnetic field measurements since NMR probes can measure the absolute accuracy of tens of ppb. Protons in the NMR probes are in hydrocarbons in petroleum jelly that can produce and detect the free induction decay signals (FID). I will talk about the FID in detail in Chapter 5. There are three types of probes with different purposes in the experiment: plunging probes, trolley probes, and fixed probes. The schematics of fixed probes and trolley probes are shown in Figure 4.1. I will discuss each of these probes in detail in the next few sections [76].

4.2.1 Trolley Probe

17 NMR probes in the trolley are the primary system used for mapping the field around the ring in the volume that the muons are stored when the beam is off. Fig 4.2 (a) is the photograph of a trolley that is about 50 cm long. The trolley moves around the ring on the track (rail), which is installed inside the vacuum chamber by two lines to facilitate clockwise and counterclockwise motion.

Inside the trolley, 17 NMR probes are arranged in a concentric circle with one probe at the center, at the muon ideal orbit, shown in Fig 4.2 (b). There are 4

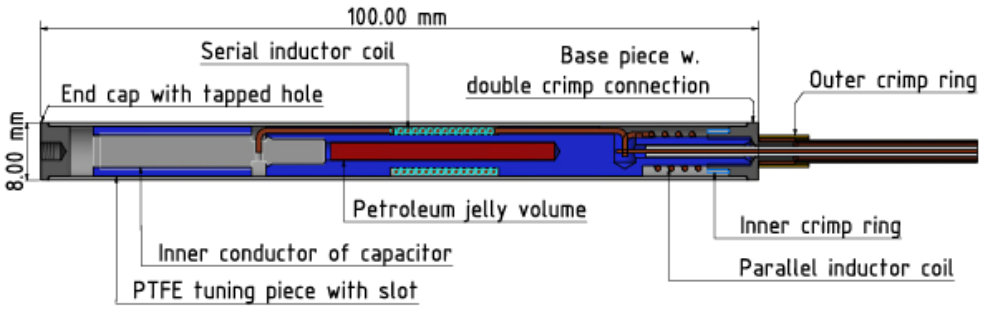

FIGURE 4.1: Schematic drawing of the NMR probe for field mapping and monitoring [13].

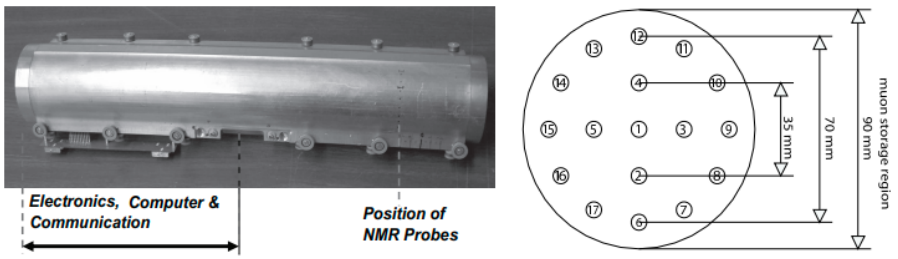

(a) NMR Trolley (b) Distribution of NMR probes

FIGURE 4.2: (a) Photograph of the trolley. (b) The schematic diagram shows 17 probe locations and there probe numbers. [15]

probes at a 1.75 cm radius and 12 probes at a 3.5 cm radius. The probes are read out sequentially, taking roughly 0.5 seconds to collect all 17 probe full measurements.

There are two ways to determine the trolley location: the encoders and the barcode. Encoders on the drums determine how much the cables have been pulled but this method has a large uncertainty because of the elasticity and the length of the cables. To improve position determination, there is a new method called optical barcode readers. We marked the bottom of the interior of the vacuum chamber with two different barcodes: the absolute barcode and the reference barcode. The absolute barcode marks are at every 20 cm and are used to locate the trolley in SR.

The reference barcode marks every 2.5 mm and it is used to interpolate positions between the absolute marks [60]. The precision of the trolley barcode positions at all times is more precise than 1 mm accuracy [77].

The trolley is retracted to the trolley garage at the outside of the muon orbit during muon storage. Then, when the beam is off, the trolley is inserted into the ring. A standard trolley run has three parts. The first part is a clockwise run from the trolley garage to the trolley drive starting position after we take out the trolley from the garage. This part is about 90°long. The second part is a counterclockwise run of the full circle from the drive starting position to the drive starting position about 360°drive. This data is usually used to analyze the field measurement since it runs full circle. The last part is a clockwise run from the drive starting position to the garage which is about 270°. Fig 4.3 shows the three parts of the typical standard trolley run.

4.2.2 Fixed Probe

The purpose of the fixed probe (fxp) system is to monitor the field continuously while the beam is on and the muons are present. A single analog multiplexer consists of up to 20 fxp and a total of 20 multiplexers handle all 378 fxp. It takes 1.33 sec for all the probes to be digitized and read out in E989.

378 fxp are mounted at 72 stations (locations) in the azimuth around the ring. There are either 4 or 6 probes for each station, evenly split between the top and bottom of the vacuum chamber. Fig 4.4 shows a geometry of 4 and 6 probe stations with respect to the muons' ideal orbit. In Chapter 6, I will discuss fxp analysis and uncertainty in detail.

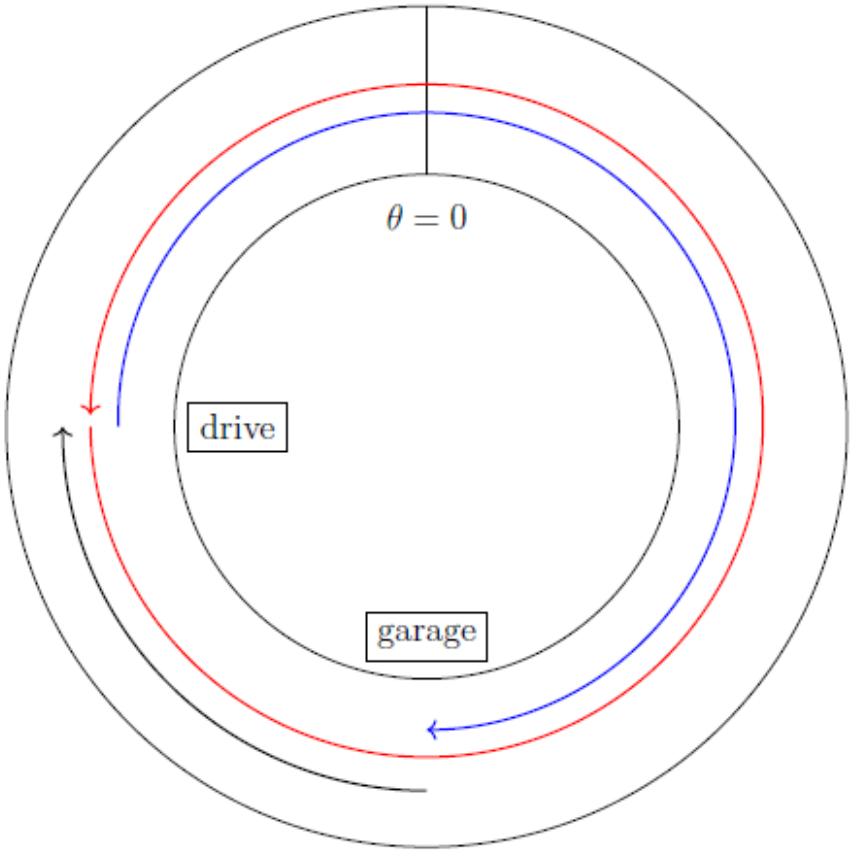

FIGURE 4.3: Typical trolley run with three different parts. The first part is black (clockwise), the second part is red (counter-clockwise), and the third part is blue (clockwise). [60]

4.2.3 Absolute Probe (Plunging Probe)

The calibration is necessary for the trolley probes which generate the magnetic field map of the storage volume because the materials (teflon, copper wire, and aluminum) of the trolley perturb the local magnetic field seen by the onboard NMR probes. An absolute probe with well-known perturbations is used to calibrate the trolley probes' unknown perturbations as a reference. More detailed calibration analysis of Run 3 and beyond will be discussed in Chapter 7. Schematic drawing of the calibration probe, or plunging probe, is shown in Fig 4.5.

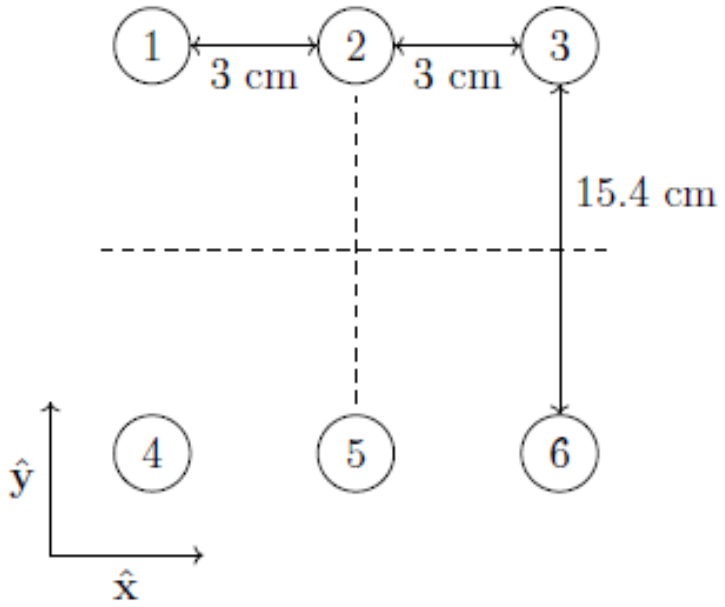

FIGURE 4.4: The diagram shows the standard geometry of a 6-probe station. A standard 4- probe station does not include probes numbered 1 and 4 [60].

The plunging probe is water-based and we use the He-3 based probe for cross-calibration in the ANL magnet. The uncertainty study for the plunging probe will be discussed in Chapter 8.

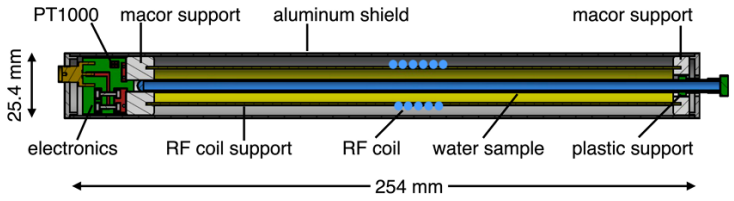

FIGURE 4.5: Design drawing for the calibration probe. Tunable capacitors and a temperature sensor are housed in the section at the far left end of the device [78].

4.3 Data Acquisition System

The magnetic field Data Acquisition (DAQ) System server is an access point for controlling individual field measurement systems including fixed probes, trolley control, trolley readout, calibration probe control, and more. These systems are each managed by custom front ends that run asynchronously and communicate with a common DAQ core. The field DAQ collects data whenever the magnet is powered [13].

4.4 Analysis Flow

The analysis flow is shown in Fig 4.6 from the calibration chain through the data processing. The first step is the extraction of FID parameters such as the frequency, amplitude, and length from all NMR measurements. Data quality cuts (DQC) are applied on these extracted parameters to discard FID waveforms that correspond to instrument failures or severe field instabilities [13]. Then, to determine $\tilde{\omega}_p'(T_r)$ from equation 4.3, we perform a sequence of measurements with proton-rich magnetometers [13]:

1. The 17 NMR probes of the in-vacuum trolley are calibrated with a precision calibration probe (plunging probe) based on a pure water sample. The calibration probe's precise measurements are corrected for material effects, temperature, and field variations during the calibration to achieve high accuracy and precision.

2. The magnetic field in the muon storage volume is mapped using the trolley approximately every three days.

3. The 378 fixed NMR probes in 72 azimuthal stations are synchronized to the trolley measurements. These fixed probes monitor the field's drift between trol-

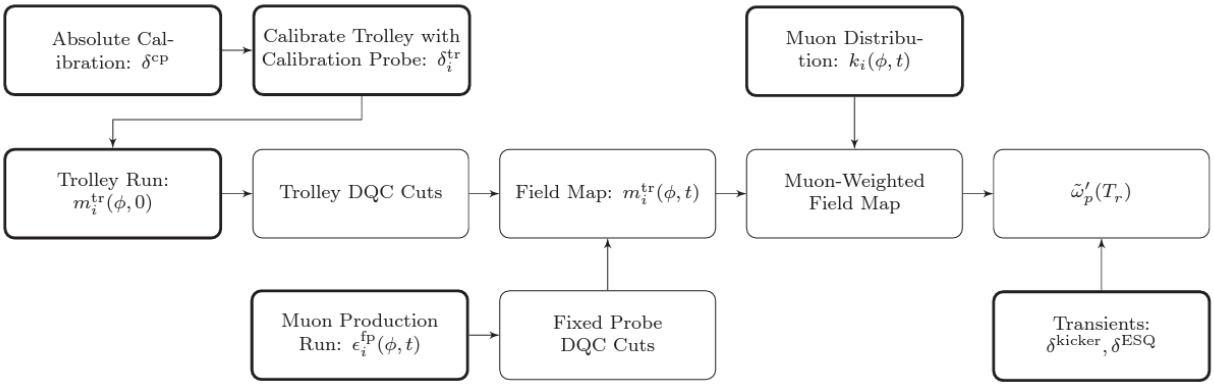

FIGURE 4.6: A flow chart of the field analysis showing the calibration chain through the data processing. The muon distribution is an input that is external to the field analysis and is required to calculate the muon-weighted field average. Bold items show input measurements to the analysis. Not shown is the NMR frequency extraction step required for each of the field measurements [13].

ley maps.

4. The magnetic-field maps are weighted by the temporal and spatial distributions of those muons included in the ω_a measurement.

5. Corrections are applied for the presence of fast transient fields generated by pulsed muon injection systems that are not resolved by the asynchronous magnetic-field tracking and not present during the trolley measurements.

Due to the limited number of fixed probes in a station, we model the drift of higher-order moments as a random walk and include its effect only as an uncertainty. The full procedure for synchronizing and tracking the field with the fixed probes is discussed in the reference [13]. If the trolley calibration does not change over time, we can combine the fixed probe tracking, trolley maps, trolley calibration, and calibration probe corrections to the field moment. Then, this field moment is weighted by the muon distribution in space and time and an averaged over time t and azimuth ϕ to determine $\tilde{\omega}_p'(T_r)$ [13].

5

NMR Techniques

In the previous chapter, Chapter 4, the first step of the magnetic field determination analysis is the extraction of FID parameters from all NMR measurements. The most important FID parameters are frequency. Thus, the FID frequency extraction is one of the key factors in the magnetic field measurement. In this chapter, I introduce the NMR frequency extraction method in the experiment and discuss the basic steps of how we extract the precession frequency of the protons in our NMR sample.

5.1 Overview

Pulsed nuclear magnetic resonance (pNMR) is widely used in high-precision magnetic field measurements because pulsed NMR magnetometers typically have a precision better than 1 ppm [79]. The magnetic field magnitude B is determined by measuring the proton spin precession angular frequency, $\omega_s = \gamma B$, where γ is the gyro-magnetic ratio of a proton [79]. The experiment applies a radio frequency (RF) pulse to rotate the effective magnetization perpendicular to the external magnetic field by $90^\circ(\pi/2)$. Fig 5.1 shows that RF pulse flips the spin from the vertical (y-axis) to the XZ plane. The magnetization precesses in the XZ plane (horizontal) and begins to relax to be

pointed along the external magnetic field. The time it happens is called T_1 time. Also, the individual proton spins influence each other, called spin-spin interaction, which causes them to dephase each other. This damps out the magnetization precessing and a time of this decoherence is called T_2 time. This oscillating signal of the rotating magnetization is called free induction decay (FID) signal [80]. We use this FID signal to extract the NMR frequency and other FID parameters.

There are three types of NMR probes in the experiment: trolley probe, fixed probe, and plunging probe. I have discussed the purposes of these probes in the previous chapter, Chapter 4. Throughout the dissertation, I will discuss individual probe types in detail: fixed probe (Chapter 6), trolley probe (Chapter 7), and plunging probe (Chapter 8).

Even though each probe has different purposes, the overall framework of NMR frequency extraction is the same. Here is the current framework:

1. Single RF pulse flips the spins by 90 °(Shown in Fig 5.1).
2. The precessing magnetization generates an oscillating signal.
3. Free induction decay (FID) signal is filtered, amplified, and frequency-mixed down.
4. FID signal passes the low-pass filter.
5. The phase as a function of time is extracted.
6. Polynomial fit to phase function within a certain fit window is used to extract frequency.
7. The frequency averaged over the active volume corresponds to the slope of the phase function at the time right after the $\pi/2$ pulse.

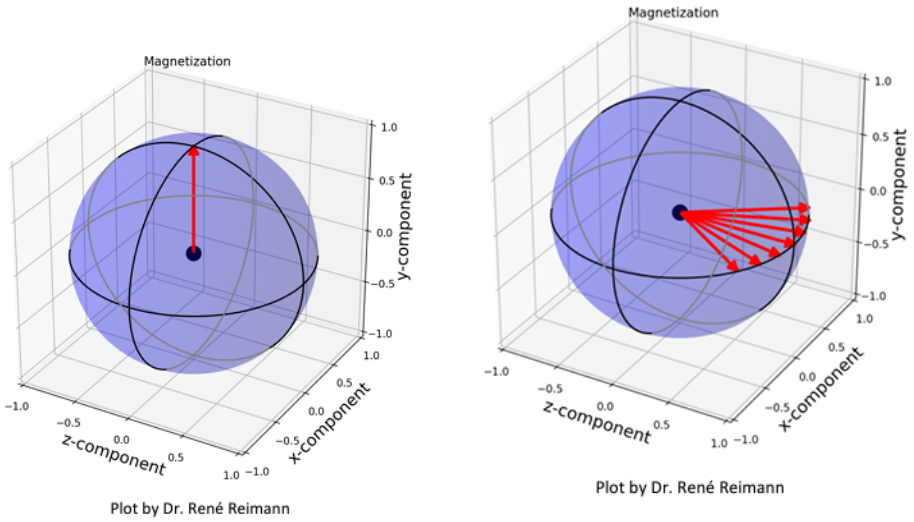

FIGURE 5.1: RF pulse flips the spins by 90°from left diagram to right diagram [81].

5.2 NMR FID Signal Model

5.2.1 Uniform Field

After the RF pulse, in a uniform field, all proton spins process at the same angular frequency ω. The signal amplitude decays due to energy loss (T_1 time constant) and decoherence (T_2 time). The FID signal model is defined as,

$$\begin{aligned} f(t) &= Aexp(-\frac{t}{\tau}exp(i(\omega t + \phi_0)), \\ \frac{1}{\tau} &= \frac{1}{T_1} + \frac{1}{T_2}, \end{aligned} \tag{5.1}$$

where ϕ_0 is a constant initial phase.

5.2.2 Non-uniform Field

In a non-uniform field, protons at different positions precess at different angular frequencies which represent $\Omega(x, y, z)$. In addition to the angular frequencies, the initial amplitude of the spin precession signal A(x,y,z) and the response function of the coil $\eta(x, y, z)$ are also a function of positions. The contributions of each spin can

be integrated, and the total signal is expressed as,

$$f(t) = exp(-\frac{t}{\tau}) \int\int\int_{-\infty}^{+\infty} exp(i\Omega(x,y,z)t + \phi_0)A(x,y,z)\eta(x,y,z)dxdydz \tag{5.2}$$

To simplify Equation 5.2, $g(\omega)$ is defined and called the signal distribution function. Equation 5.2 can be simplified as,

$$f(t) = Nexp(-\frac{t}{\tau}) \int_{-\infty}^{+\infty} g(\omega)exp(i(\omega t + \phi_0))d\omega \tag{5.3}$$

where N is a combination of normalization amplitude for $g(\omega)$.

If ω is written as $\omega = \omega_0 + \Delta\omega$, where ω_0 is the position of $g(\omega)$'s peak, the non-uniform field results in the additional factor comparing it to Equation 5.1 is,

$$\int_{-\infty}^{+\infty} g(\Delta\omega)exp(i(\Delta\omega t))d\Delta\omega \tag{5.4}$$

Equation 5.4 can be expressed as the inverse Fourier transform of $g(\Delta\omega)$.

$$\begin{aligned} \int_{-\infty}^{+\infty} g(\Delta\omega)exp(i(\Delta\omega t))d\Delta\omega &= C(t) + iS(t) \\ &= \sqrt{C^2(t) + S^2(t)}exp(i\tan^{-1}\frac{S(t)}{C(t)}), \end{aligned} \tag{5.5}$$

$$\begin{aligned} S(t) &= \int_{-\infty}^{+\infty} g(\Delta\omega)\sin(\Delta\omega t)d\Delta\omega, \\ C(t) &= \int_{-\infty}^{+\infty} g(\Delta\omega)\cos(\Delta\omega t)d\Delta\omega, \end{aligned}$$

$S(t)$ and $C(t)$ are an odd and even function of t. Finally, the FID function $f(t)$ can be rewritten as,

$$\begin{aligned} f(t) &= Nexp(-\frac{t}{\tau})E(t)exp(i(\omega_0 t + \phi(t) + \phi_0)), \\ E(t) &= \sqrt{C^2(t) + S^2(t)}, \\ \phi(t) &= \tan^{-1}\frac{S(t)}{C(t)}, \end{aligned} \tag{5.6}$$

where $E(t)$ is the signal envelope and $\Phi(t) = \omega_0 t + \phi(t) + \phi_0$ is the phase function which, in general, is not a linear function. This formalism was developed by Hong Ran [79].

5.3 NMR Frequency Extraction Methods

The average NMR frequency $\bar{\omega}$ weighted by $g(\omega)$ is determined by

$$\bar{\omega} = \int_{-\infty}^{+\infty} \omega g(\omega) d\omega, \tag{5.7}$$

which can be rewritten by calculating the derivative of the phase function at $t = 0$,

$$\bar{\omega} = \frac{d\Phi(t)}{dt}|_{t=0}, \tag{5.8}$$

where $t = 0$ is the time when the RF pulse starts. An example of a typical FID signal looks like Fig 5.2 and an example of a typical phase function looks like Fig 5.3. Fig 5.3 shows the phase function of two different NMR frequency extraction methods: Hilbert transform and zero-crossing. The Hilbert transform method is already introduced in a previous section.

5.3.1 Zero-crossing Method

Flay David and the University of Massachusetts in Amherst (UMass) team use the zero-crossing method to extract NMR frequency. When phase function, $\Phi(t) = \omega_0 + \phi(t) + \phi_0$ is equal to $(n+1/2)\pi$, where n is an integer, $f(t)$ becomes 0. We can construct zero-crossing time stamps whenever $\Phi(t)$ is equal to $(n+1/2)\pi$. Let numbers of zero-crossing N_{zc} of the FID signal within the fit window. Then FID extracted frequency is computed according to the equation:

$$f = \frac{N_{zc}}{\Delta T} = \frac{N_{\mathrm{zc}} - 1}{2(t_{\mathrm{last}} - t_{\mathrm{first}})}, \tag{5.9}$$

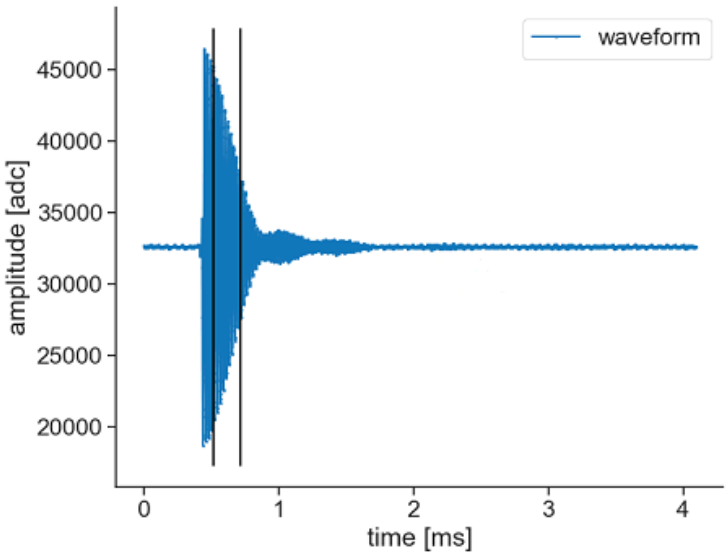

FIGURE 5.2: General example of FID. The plot shows the FID of fixed probe 0 and black lines represent the fit window.

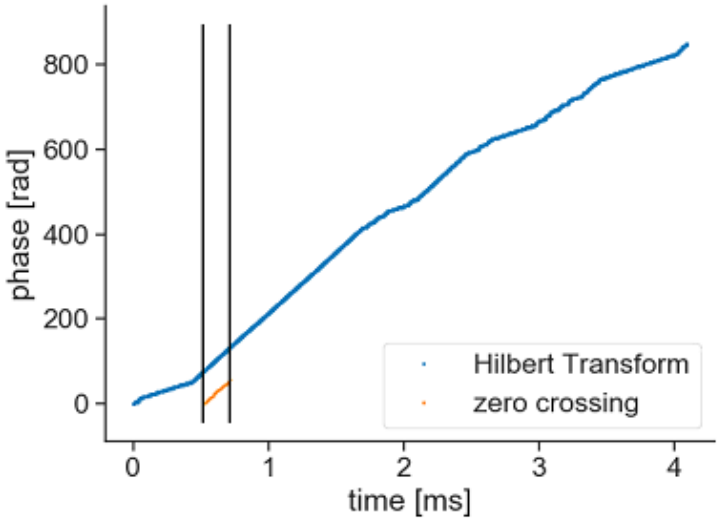

FIGURE 5.3: General example of phase function. The plot shows a phase function of fixed probe 0 with two different frequency extraction methods. Black lines represent the fit window.

where t_{last} and t_{first} are the last and first zero-crossing times of the data within fit window [80].

5.3.2 Hilbert Transform Method

The average NMR frequency $\bar{\omega}$ is determined in Equation 5.8. When I express the phase function in the Tayler series, the phase function is

$$\Phi(t) = \phi_0 + a_1 t + a_3 t^3 + a_5 t^5 ... \tag{5.10}$$

where the phase function is an odd function, so Tayler's approximation of the phase function only contains odd power terms of t. NMR frequency is calculated by the derivative of phase function at $t = 0$, $d\Phi/dt|_{t=0} = a_1$.

5.4 Phase Template Method

Since FID frequency extraction is from the polynomial fit of the phase function, a non-linearity in the phase function perturbs the frequency extraction. To reduce this perturbation to minimum effects, the phase template method is used. A phase template is made by averaging over the first 20 phase functions of 20 events per probe. Currently, we update a fixed probe phase template per a magnet cycle and we use one trolley phase template for the experiment. Once constructing the phase template, $\Delta\Phi$ is defined as

$$\Delta\Phi(t) = \Phi_i(t) - \Phi_{\text{temp}}(t), \tag{5.11}$$

where Φ_i is the phase function of event i and Φ_{temp} is the phase template. Using Tayler series to Equation 5.11, $\Delta\Phi(t)$ is expressed as,

$$\begin{aligned}
\Phi_i(t) &= \phi_{0,i} + a_{1,i}t + a_{3,0}t^3 + a_{5,0}t^5... \\
\Phi_{\text{temp}}(t) &= \phi_{0,\text{temp}} + a_{1,\text{temp}}t + a_{3,\text{temp}}t^3 + a_{5,\text{temp}}t^5... \\
\Delta\Phi(t) &= \Phi_i(t) - \Phi_{\text{temp}}(t) \\
&= (\phi_{0,i} - \phi_{0,\text{temp}}) + (a_{1,i} - a_{1,\text{temp}})t + (a_{3,1} - a_{3,\text{temp}})t^3 + (a_{5,1} - a_{5,\text{temp}})t^5...
\end{aligned} \tag{5.12}$$

Since the higher-order terms do not variate much from event to event, higher-order terms diminish and become negligible. At the end, the final $\Delta\Phi(t)$ is written as

$$\begin{aligned}
\Delta\Phi(t) &= \Phi_i(t) - \Phi_{\text{temp}}(t) \\
&= (\phi_{0,i} - \phi_{0,\text{temp}}) + (a_{1,i} - a_{1,\text{temp}})t + (a_{3,1} - a_{3,\text{temp}})t^3 + (a_{5,1} - a_{5,\text{temp}})t^5... \\
&\approx \Delta\phi_0 + \Delta a_1 t + \Delta a_3 t^3 + \Delta a_5 t^5 + ...,
\end{aligned} \tag{5.13}$$

where $\Delta\phi_0$ is $\phi_{0,i} - \phi_{0,\text{temp}}$ and Δa_1 is $a_{1,i} - a_{1,\text{temp}}$ and so on. For a fixed probe, we use only linear fit so $\Delta\Phi(t) = \Delta\phi_0 + \Delta a_1 t$. For the trolley, we use up to the fifth polynomial order to fit the phase function. The reason why we can use the phase template method is that we are not interested in the absolute value. For a fixed probe, the absolute value does not matter because the purpose of the fixed probe is to monitor the field drift. For the trolley, the absolute value does not matter because trolley measurements are calibrated by the plunging probe. The advantage of using the phase template method is to avoid using higher-order polynomials to model the residual shape at larger t, which means that the resolution is not sacrificed by shortening the fit range. Fig 5.4 shows the differences in residual plots between two phase functions: one with the phase template method and one without the phase template method. Therefore, the template method improves the quality of the fit

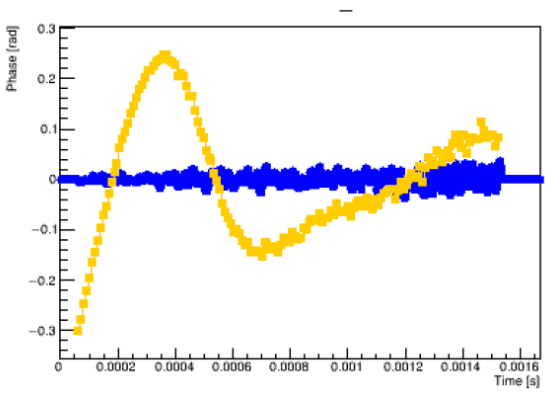

FIGURE 5.4: Blue Curve: The residual of fitting $\Delta\Phi(t)$. Yellow Curve: The residual of fitting $\Phi(t)$ alone [82].

without undermining the resolutions. However, the template method assumes that the higher-order terms do not variate from event to event. This assumption is needed to be verified and to be discussed in the systematics.

5.5 Simulation

As mentioned in Section 5.2, the precessing magnetic spins from the RF pulse generate an oscillating flux in the pick-up coil, thus oscillating voltage inside the probe. In the simulation, the RF pulse in the coil causes an oscillating magnetic field inside the coil, in the sample, that flips the spin. This needs to be calculated. Then the precession of the spin is modeled with some approximations and assumptions to simplify the calculation such as spin-spin interactions and relaxation. Finally, the signals from all spins in the NMR sample are added together to form the FID output. More detail can be found in the reference [83].

Here is the description to generate a simulated FID:

1. Define the geometry of the probe including coil and sample dimensions and the number of coil turns.

2. Calculate the magnetic field by the coil, $\vec{B}$.

3. Define the external field map.

4. Generate random spins in the sample volume.

5. Create a histogram of ω, ranging from minimum to maximum of NMR frequencies of the generated spins.

6. Fill the bin that ω_i belongs for each spin. This histogram is represented as g_ω.

7. Generate FID vector at the sampling frequency for each frequency bin.

8. Sum over all frequencies in the frequency histogram to obtain the generated FID.

9. Scale the FID to the amplitude of the experimental data, add baseline, add noise, etc.

For example, a trolley probe FID is simulated in the left plot of Fig 5.5, as a function of time in ms, and its sensitivity function is shown in the right plot of Fig 5.5, as a function of the coil length in mm. The sensitivity function will be discussed in a future chapter (Chapter 9) in more detail. This simulation tool is crucial to study the systematics of field measurements in general. We are able to estimate the uncertainty of the FID frequency extraction from NMR probes which will discuss further in Chapter 9 as well.

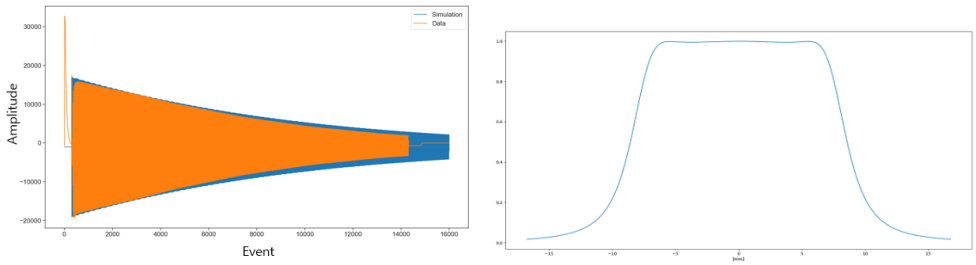

FIGURE 5.5: Left plot: example trolley simulated FID: blue signal represents simulated FID and orange signal represents actual real data FID. Right plot: example trolley sensitivity function.

6

Fixed Probe FID Frequency Extraction and Uncertainty

The purpose of the fixed probe system is to monitor the field continuously while muons are present. The system consists of a set of 378 NMR probes at 72 locations in azimuth around the ring. The number of probes at each azimuthal position alternates between two probes at radial positions of 7112 and 7142 mm, or three probes at radial positions of 7082, 7112, and 7142 mm, on the top and bottom surfaces of the storage ring vacuum chambers. From this geometry shown in Fig 4.4, the fixed probes provide a good monitor of the dipole field around the ring with some sensitivity to changes in the skew and normal quadrupole components [15].

However, every fixed probe does not have a long FID. Strong gradients, for example, near the inflector result in significantly shorter FIDs. A general example of FID and phase functions were introduced in Fig 5.2 and 5.3. Fig 6.1 shows two specific probes' FID: probe 1 and probe 16 which have significant differences in FID lengths. Probe 16 is located in the top-middle at the inflector region (location reference in Fig 4.4) and it has a short FID length that ranges only about a few microseconds.

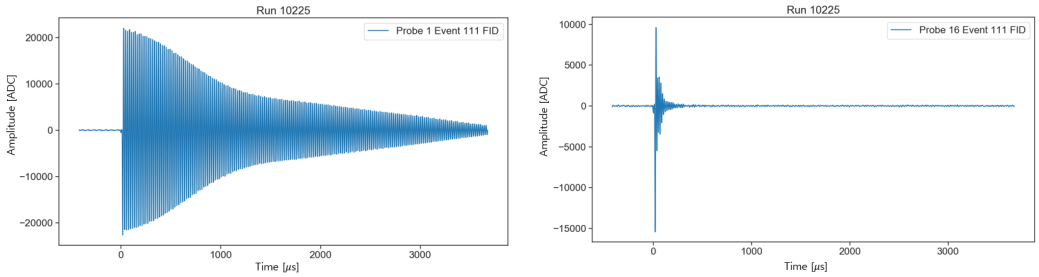

FIGURE 6.1: Left FID plot is from probe 1 which is a longer FID length probe and the right FID plot is from probe 16 which I consider a bad probe because of the shorter FID length.

Normally, we choose a fit window of FID from the maximum amplitude to 1/e of the maximum amplitude. However, due to the short FID length, a chosen fit window also becomes extremely short. Since we cannot use the first few μs from the maximum amplitude to avoid any distortions from the switching, the chosen fit window becomes even shorter. This causes challenges when conducting a frequency extraction from polynomial fit to phase function within an extremely short fit window.

6.1 FID Length Optimization

The fit window choice is an important component during the frequency extraction. Under higher-order terms, the shorter fit window is less sensitive to frequency extraction. However, the shorter fit window results in a worse resolution. To solve this issue in data production, the frequency of each FID is extracted in two fit windows. The long window is usually chosen to be from the maximal amplitude to 1/e of its maximal amplitude. The short window is generally chosen to be 40 percent of the long window, but for each of the different data sets, the length of the short window can be adjusted according to the field drift during the period and the target accuracy of the analysis.

6.1.1 Edge Ignore Window (EIW)

Edge Ignore Window (EIW) is one of the parameters in the analysis that is chosen according to the experiment before the optimization. EIW is defined as the point in time a signal reaches its maximum amplitude to the point where the fit window begins. After this short period of time, the fit window begins to take measurements so that the filter effects on the edges decay away. EIW is set to 60 μs as a default. The good probes have a FID fit window length that has a range of ms, so the value of 60 μs EIW does not affect their resolution. However, the bad probes have a FID fit window length that has a range of μs, so the EIW affects their resolutions enormously. Fig 6.2 from probe 17 shows that its fit window with 60 μs EIW does not include most of the long-amplitude oscillations of the FID and this results in a worse resolution for probe 17. Fig 6.3 shows the comparison between probe 1 and probe 17's resolutions.

Probe 17's frequencies shown in Fig 6.3 fluctuate much more than probe 1's frequencies. Therefore, the motivation of the study is to optimize the fit window to improve probes' resolutions, especially for the shorter FID probes. In order to optimize the fit window, the first step is to change the EIW value from 60 μs to 5 μs so that there is only an insignificant loss of the oscillations for the shorter FID probes. This change does not affect the longer FID probes too much because their fit ranges are usually in millisecond ranges and the difference of 55 μs from the EIW changing does not affect their frequency extractions and resolution.

From frequencies in Fig 6.4, the mean frequencies of 60 μs and of 5 μs EIW settings are 51687.25 Hz and 51685.57 Hz. The difference between the two was about 2 Hz. However, these absolute values are not meaningful because the fixed probes' purpose is to monitor the field during this period. Thus, the absolute values of the frequencies do not matter significantly, and instead, we focus on the drift of the

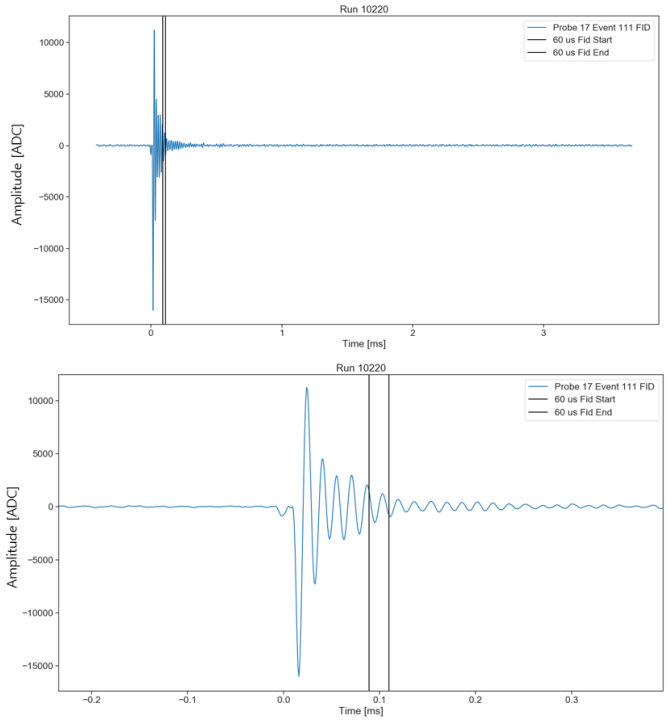

FIGURE 6.2: Top: FID plot is probe 17 which is one of the bad probes (shorter FID). Bottom: The FID plot is zoomed in the fit window of the top plot. Black lines are the range of the FID length from 60 μs after the maximal amplitude to 1/e of the maximal amplitude.

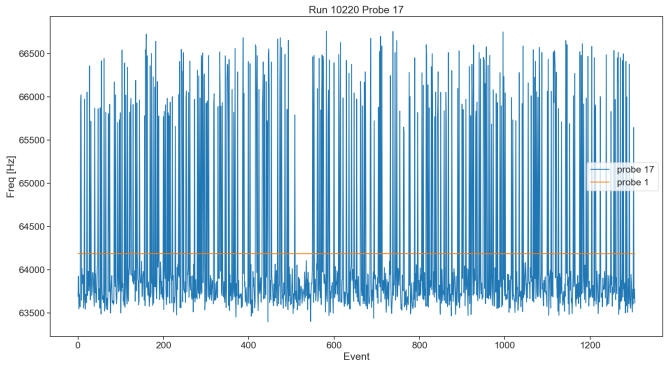

FIGURE 6.3: The data is from Run 3 (Run 10220). The blue plot is probe 17's frequencies as a function of the event and the orange plot is probe 1's frequencies as a function of the event.

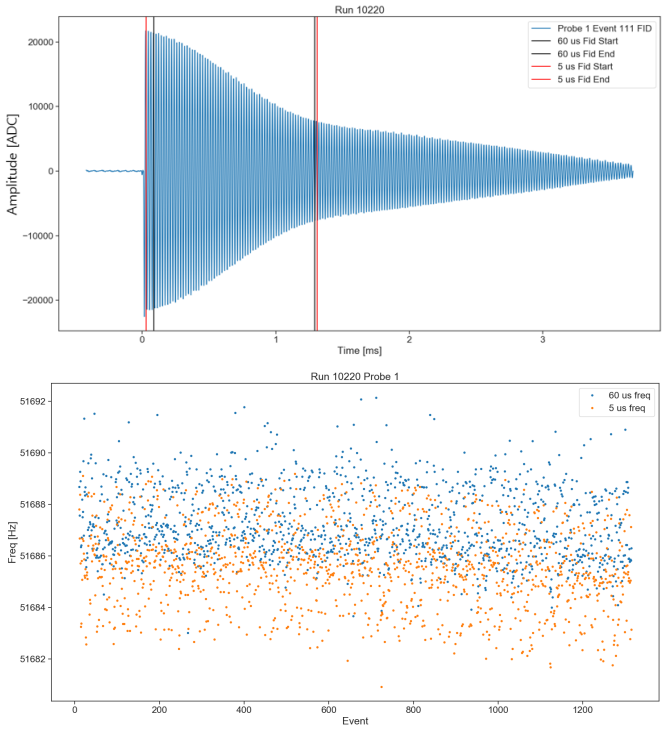

FIGURE 6.4: Top plot is probe 1's FID with 60 μs EIW (black line) and 5 μs EIW (red line). The bottom plot shows probe 1's frequencies as a function of events

data. Therefore, a 2 Hz frequency difference does not have significant importance and instead we focus on the frequency drift and resolution. The standard deviation of 60 μs EIW setting is 1.40 Hz and the standard deviation of 5 μs EIW setting is 1.54 Hz which is a difference of less than 0.15 Hz (2.5 ppb). In conclusion, the EIW change does not influence the resolutions for longer FID probes.

On the other hand, shorter FID probes are significantly dependent on EIW because of their extremely short FID length in ranges of microseconds shown in Fig 6.5. In addition to different fit window lengths, the right plot in Fig 6.5 shows that the standard deviation decreases after changing the EIW setting from 60 μs to 5 μs.

However, in a few cases, the change in the EIW distorts the resolution of the fixed probes. For example, probe 17, the left plot in Fig 6.6, shows that the fit window length is reduced when I change the EIW setting from 60 μs to 5 μs. Because the fit

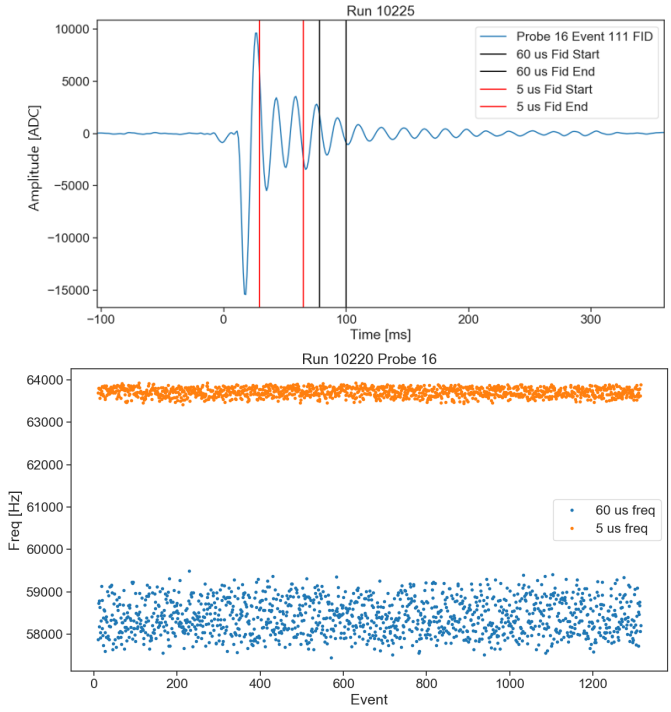

FIGURE 6.5: Top plot is probe 16's FID with 60 μs EIW (black line) and 5 μs EIW (red line). The bottom plot shows probe 16's frequencies as a function of events of two different EIW settings (Blue represents the 60 μs EIW setting and orange represents the 5 μs EIW setting .

window length is shorter, the standard deviation of probe 17 gets worse. To fix this problem, I need to figure out the optimized fit window length that has the smallest standard deviation for all probes. From this motivation, I design the optimization method.

Fit Window Optimization Method [6.1]

1. Keep the initial fit start position (5 μs EIW setting).
2. Guess the fit end position and start to increase the fit end position by a small step (depending on the fit window length).
3. Measure the extracted frequencies' RMS for each different fit window end position.

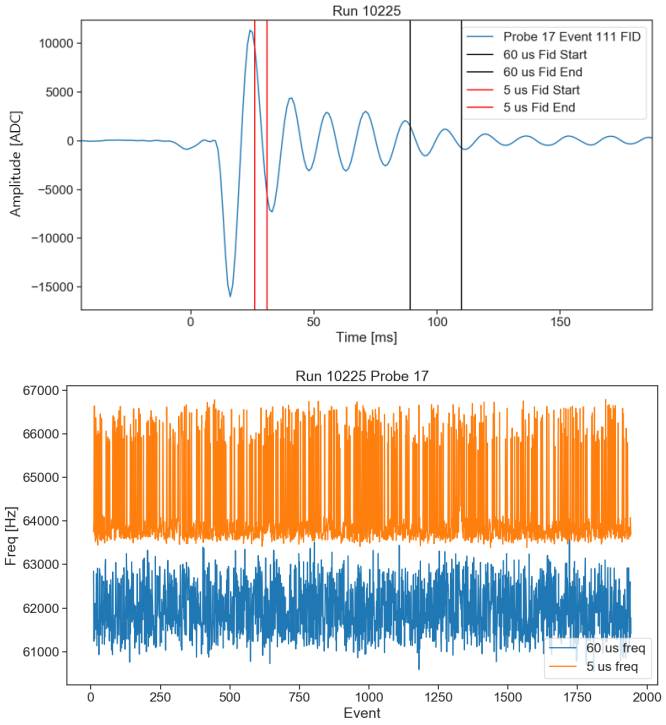

FIGURE 6.6: Top plot is probe 17's FID with 60 μs EIW setting (black line) and 5 μs EIW setting (red line). The bottom plot shows probe 17's frequencies as a function of events of two different EIW settings (Blue represents the 60 μs EIW setting and orange represents the 5 μs EIW setting.

4. Repeat step 2 to 3 until I get a long-enough fit range that is able to see the curve and find the minimum RMS.

5. Define the minimum of the curve, minimum RMS, as the end position of the optimized new fit window.

6.1.2 Finding the Optimized Fit Window

Before I start the optimization method that I describe in the previous section, I want to figure out how many probes have shorter FIDs. I define good probes (or longer FID probes) when their standard deviation is less than 2 Hz. For this analysis, I pick one of the fixed probe runs, Run 10220, from the Run 3 dataset to extract fixed probes'

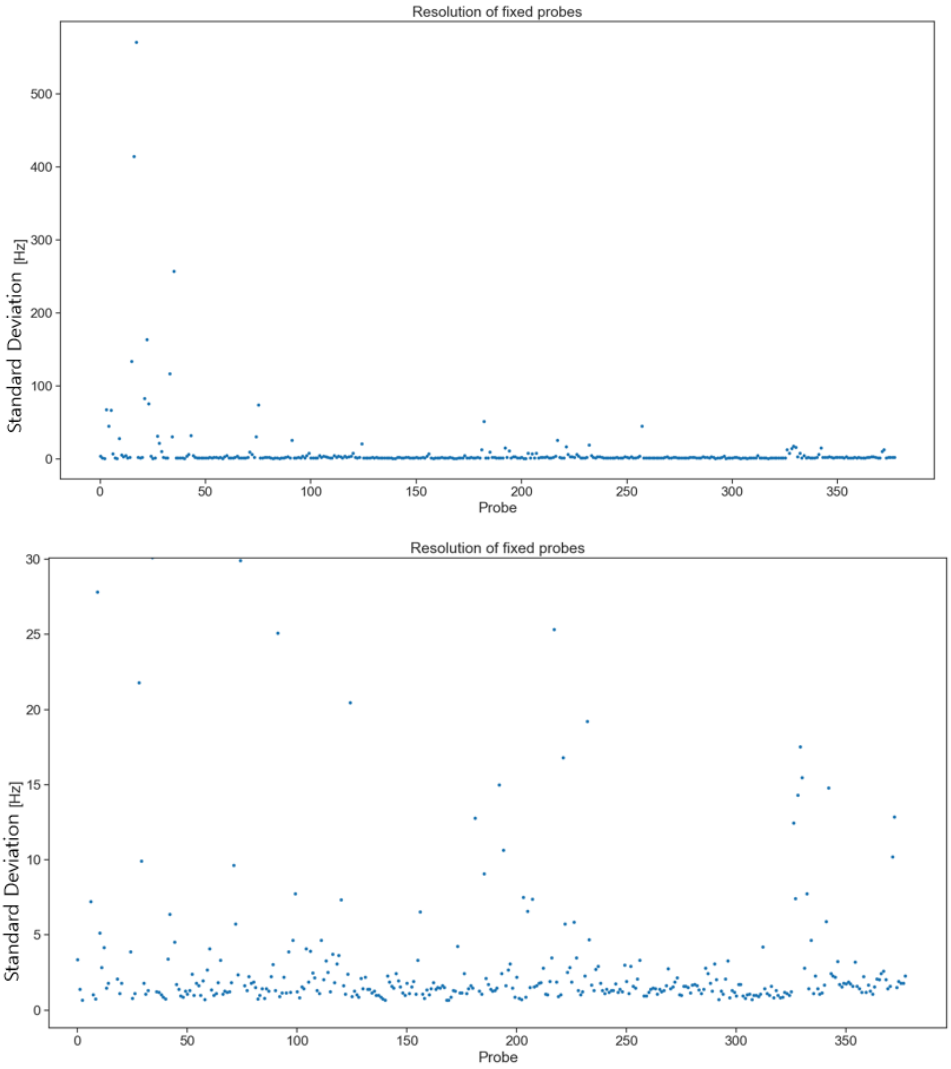

FIGURE 6.7: Top plot is the standard deviation of all fixed probes in Run 10220. The bottom plot is zoomed in y-axis ranges from 0 to 30 Hz from the top plot.

frequencies, and their standard deviation is shown in Fig 6.7. It shows that most of the fixed probes' standard deviations are less than 5 Hz. As a result, according to my definition of a good probe, 132 out of the 378 probes were defined to be bad probes.

I apply the 5 μs EIW setting to bad probes to verify that my new EIW setting actually decreases in bad probes' standard deviations. Fig 6.8 shows the standard deviations of 132 probes with two different colors: blue for 60 μs EIW setting and

Probes	Old Fit Window	New Fit Window	Std (before)	Std (after)
15	(518, 587)	(456, 544)	133.4648	18.0574
16	(498, 520)	(449, 505)	414.4725	40.8931
17	(509, 530)	(446, 507)	571.037	29.237
22	(499, 541)	(446, 570)	169.7193	13.134

Table 6.1: Examples of the new fit windows for some fixed probes. The table contains the original fit window [μs] as (start, end) and the new fit window as (start, end). Also, the table includes the standard deviation [Hz] of old and new fit window lengths. All data is from Run 10220. The full modification table is in **Appendix B**.

orange for 5 μs EIW setting. I find that there are 13 probes that have significantly larger standard deviations after the change: Probe 17, 22, 27, 59, 60, 96, 141, 182, 216, 217, 287, 296, and 367. A list of bad probes and their Run 10225 RMS are shown in Appendix B. I apply my fit optimization method 6.1.1 to these probes first.

The red lines in the left plot in Fig 6.9 represent the start and end time of the fit window range. I fix the start time and change the end time in small steps. For probe 17, I set the step as 5 μs and this step is different depending on a probe's FID length. The right plot in Fig 6.9 shows the RMS of each different end time (in a unit of μs) for probe 17. The RMS decreases as the fit window length gets longer but at a certain point, the RMS starts to increase. The end time of the smallest RMS (the smallest RMS is at 507 for probe 17 in Fig 6.9) is defined as the optimized end time. I define the optimized fit window from start time to its optimized end time and I repeat the same steps to all the other bad probes to optimize their fit window to have the smallest RMS.

However, the RMS of one single run is insignificant because there is a chance that a certain probe only acts strangely in the particular run. Therefore, one single standard deviation is not enough to conclude that my new method improves resolutions of shorter FID probes. To reiterate, the purpose of the fixed probes is to monitor the field so that the drift of the field has a higher significant importance than the

absolute value of the field.

6.2 Production Processing

To check multiple runs with the new fit window, the production script needs to be modified. The production campaign is the chain of the process to produce the dataset for analysis. There are three stages of data processing: online, nearline, and offline. The E989 uses MIDAS [15] to collect the data from the probes. Then, it tosses to the nearline which is used for monitoring and collecting calibration. Finally, it passes to offline which has the requirement to process all the data since offline data is the one used for all different analyses. The E989 experiment production team works hard to convert online data to offline data with their framework (ART). More details of the production processing can be found in TDR [15].

6.2.1 Implementation to Production Process

After finishing with the new fit window algorithm for Run 10220, I want to implement this algorithm to all runs during Runs 2 and 3. An efficient way to do this is to modify the offline script in the production campaign. We implemented these changes to the standard production codebase and included it by default in the production chain. Because the production processing used multiple CPUs for parallel processing, I was able to optimize not only bad probes but also all 378 probes at one time. After a few days, I was able to get all the production files of Run 2 and Run 3.

6.3 New Fit Window Analysis.

6.3.1 Run 2 and 3: Frequency Extraction Analysis

Run 2 Dataset is listed in Appendix A. There are more than 500 runs for Run 2. I extract the frequencies from two different modes for all runs in Run 2: default and new fit window. Then, I take 20 consecutive events of each run and find the RMS of

20 events' frequencies. RMS plots are shown in Fig 6.10. I repeat this for the Run 3 Dataset listed in Appendix A. There are 860 runs in Run 3 and the Run 3 RMS plots are shown in Fig 6.11.

Run 2 bad probes' average RMS difference between old and new fit window settings is -0.64 Hz. The maximum difference is 8.87 Hz, and the minimum difference is -14.20 Hz. A negative sign means that the old fit window setting is better than the new fit window setting. 13 probes out of 36 (total selected probes) have a worse RMS after changing to the new fit window settings, however, most of them improve RMS after the change. For Run 3, the bad probes' average RMS difference between old and new fit window settings is 0.36 Hz. The maximum difference is 3.35 Hz, and the minimum difference is -2.22 Hz. Run 3 has a better dataset than the Run 2 dataset since the overall Run 3 mean RMS is smaller than Run 2 mean RMS. There is only four probes that become worse after changing to the new fit window for Run 3. Including all 378 probes, the average difference RMS from Run 2 is -0.03 Hz and the average difference RMS from Run 3 is 0.03 Hz. Overall, both Run 2 and Run 3 do not have a significant difference from changing fit window settings and are affected by less than 0.5 ppb levels.

After analyzing Run 2 and Run 3 data, I question why my new fit window setting does not improve resolutions for some specific probes such as probe 330. My new fit window setting should include more oscillations for shorter FID probes and should be the same for good probes. I generate new plots to visualize what probes get worse after changing the fit window settings. The new plots are the mean frequency RMS differences between the two fit window settings from all datasets in Run 2 and Run 3 for each probe shown in Fig 6.12

From Fig 6.12, there are a few probes in Run 2 and Run 3 that the RMS differences are below 0. For example, RMS differences from probes 5, 35, 182, and 330 in Run 2 are worse than -50 Hz. RMS difference per probe is calculated as RMS (old setting)

minus RMS (new setting) per probe. Therefore, the negative RMS difference implies that the RMS gets worse after changing the fit window setting.

I select probes 5, 35, 182, and 330 because these four probes have the worst RMS difference after changing the fit window setting in Run 2. I generate the RMS difference plots as a function of the run numbers so that I can visualize which run numbers are the worst in Run 2 shown in Fig 6.13. Probe 5 shows that entire datasets get worse. We exclude probe 5 for the analysis because of poor resolution for my analysis but further investigations are needed from other analyzers. Probe 35 seems good besides two outliers, but I discover that these two outliers are from noise. After applying the DQC cut, these outliers are removed. Probes 182 and 330 have two parts: regions with approximately 0 RMS differences and regions with huge RMS differences. These two probes also need further investigation.

The further investigation of one of the two probes, probe 330, is shown in Fig 6.14. The subplots represent frequencies as a function of events in two different runs: run 6856 and run 7455. Run 6856 is picked in the good region, which is approximately 0 RMS differences. The left subplot shows that the bandwidths of the original and new fit window settings are almost same widths. This explains that the two settings have about the same RMS and the difference between them is close to zero. Run 7455, however, is the worst RMS difference run of the entire Run 2 dataset. The right subplot shows that there is a double-band structure for the new fit window setting which causes an extremely large RMS. I also check probe 182 and the large RMS difference is caused by the double-band structure. I investigate the FID signal to figure out why the double-band structure happens for some specific probes.

The FID of probe 330 is shown in Fig 6.15. The FID shape is not the typical FID shape because it has multiple nodes. In general, FID does not have any nodes and looks like a decay exponential function. Black vertical lines represent the old-fit window's start and end. The new fit windows for run 6856 and run 7455 starts in

the same position but run 6856 ends at the red vertical line and run 7455 ends at the green vertical line. One thing I notice is that the differences between run 6856 and run 7455 fit end positions are far from each other. Indeed, Run 7455's fit end position passes the first node to another node. I suspect that because Run 7455's fit end position passes the first node of the FID and is located in the second node, the double band is formed. I start to investigate further to verify a fit end position in the other nodes besides the first node causes the double band.

For probe 233, in run 8996, frequencies as a function of events are shown in the top plot from Fig 6.16 with three different settings: old fit window, new fit window 0.4 (40% of the nominal fit window), and new fit window 0.7 (70% of the nominal fit window). The new fit window 0.4 and the new fit window 0.7 shows that we used 0.4 and 0.7 proportion of the fit window length. For example, when the fit window length is 100 ms, the fit window of 0.4 and 0.7 proportions is 40 ms and 70 ms. The plot shows that the orange color graph, labeled as new setting 0.7, forms a double-band structure whereas the other two graphs do not. In order to investigate the cause of the double-band structure, I need to look at FID, and the bottom plot in Fig 6.16 shows that FID with all fit window ranges for each setting. Probe 233's FID also does not look like a typical FID and has two nodes before the signal completely fades out. I realize that the fit window end point of the new setting 0.7 passes the first node and is located in the second node. Meanwhile, the fit window end points of the old setting and the new setting 0.4 lands within the first node. There are two more probes, probe 182 and probe 221, where the RMS differences are huge. Therefore, I look at these two probes as well. Fig 6.17 shows the FIDs of probe 182 and probe 221. In conclusion, the huge RMS differences between the old and new fit window settings happen in probes' FIDs that are not typical FID shapes and have more than one node. Whenever the fit window range passes the first node, the double band structure occurs and causes an extremely large RMS. To improve my new fit

window optimization algorithm, the maximum fit window range setting is needed so that it prevented the double band structure to the production stage.

6.3.2 Run 2 and 3: Sync Offset Analysis

The main handle on estimating our ability to track the field drift is called *sync offset*. It is the difference between a field map tracked by the fixed probes to the times of a second field map with respect to the "truth" of this second field map. *Sync offsets* can be calculated as a function of azimuth and an example of an azimuthally resolved *sync offset* of the **3d2** *trolley period* is shown in Fig 6.18. All the trolley periods of Run 2 and Run 3 are listed in Appendix A. The detailed explanations of interpolation and sync offsets are from the Run 2 and Run 3 field paper [18].

For this thesis study, I use the Purcell framework, one of two parallel code repositories used in the field analysis. There are two sync offsets we are interested in:*mixing* and *mixing with m5 from trolley*. *Mixing* represents the fixed probe's multipoles mixed into the dipole tracking. *Mixing with m5 from trolley* represents the trolley's normal sextupole (m5) mixed into *mixing*.

To use the Purcell framework, first, I need to choose the *period* and run the script to generate the sync offset average values and plots. The **3o3** trolley period sync offset plots are shown in Fig 6.19 with two different fit window settings. The plot shows all three types of sync offsets: *no mixing*, *mixing*, and *mixing with m5 from trolley*. *No mixing* represented the dipole tracking without any multipole mixing but we, in general, were not interested in the *no mixing* values. In **3o3** trolley period, average *mixing* sync offset reduces from -15.95 Hz to -15.13 Hz after changing the fit window setting. Average *mixing with m5 from trolley* sync offset, however, increases from -2.69 Hz to -2.92 Hz after changing the fit window setting. Average sync offset values of all periods of Run 2 are shown in Table 6.3.2 and average sync offset values of all periods of Run 3 are shown in Table 6.3.2. The histograms from the two tables,

Dataset		Mixing Avg		Mixing with m5, from trolley	
Run	Sub Run	Old [Hz]	New [Hz]	Old [Hz]	New [Hz]
2B	1	-5.97	-4.97	-1.61	-2.06
2C	1	5.64	5.37	-1.01	-1.42
	3	11.31	13.58	2.79	2.38
2D	1	4.53	5.67	-4.55	-4.79
	2	-3.69	-5.07	-2.80	-2.43
	3	3.03	2.93	-0.27	-0.28
	4	-2.86	-2.61	-0.59	-0.65
	5	2.04	1.89	-3.26	-3.28
	6	2.18	2.20	1.29	1.33
2E	1	0.34	-19.63	3.59	2.65
	2	-17.84	-33.28	-2.41	-2.88
2F	1	-6.48	-4.46	-4.63	-4.61
	2	-5.07	-4.33	-3.68	-3.70
2G	1	7.79	11.96	-4.92	-5.04
2H	1	-5.98	-6.85	-4.56	-4.56

Table 6.2: The table is shown an average sync offset of the azimuthal of old and new fit window settings in two different sync offset measurements: Mixing and Mixing with the trolley's m5.

Table 6.3.2 and Table 6.3.2, are generated and shown in Fig 6.20.

6.4 Summary

There are 378 probes mounted outside of the muon's path around the storage ring. Some regions, such as the inflector region, inevitably have larger gradients than other regions that affect the FID signal lengths. In general, a nominal fit window is chosen from the maximum amplitude to 1/e of the maximum amplitude. However, a nominal fit window causes bad resolutions to a few specific probes with extremely short FID lengths. Therefore, optimized fit windows per probe are needed to improve their resolutions. While the effects on individual probes of optimized fit windows can be significant, this study shows that the analysis can be optimized but with marginal overall gains.

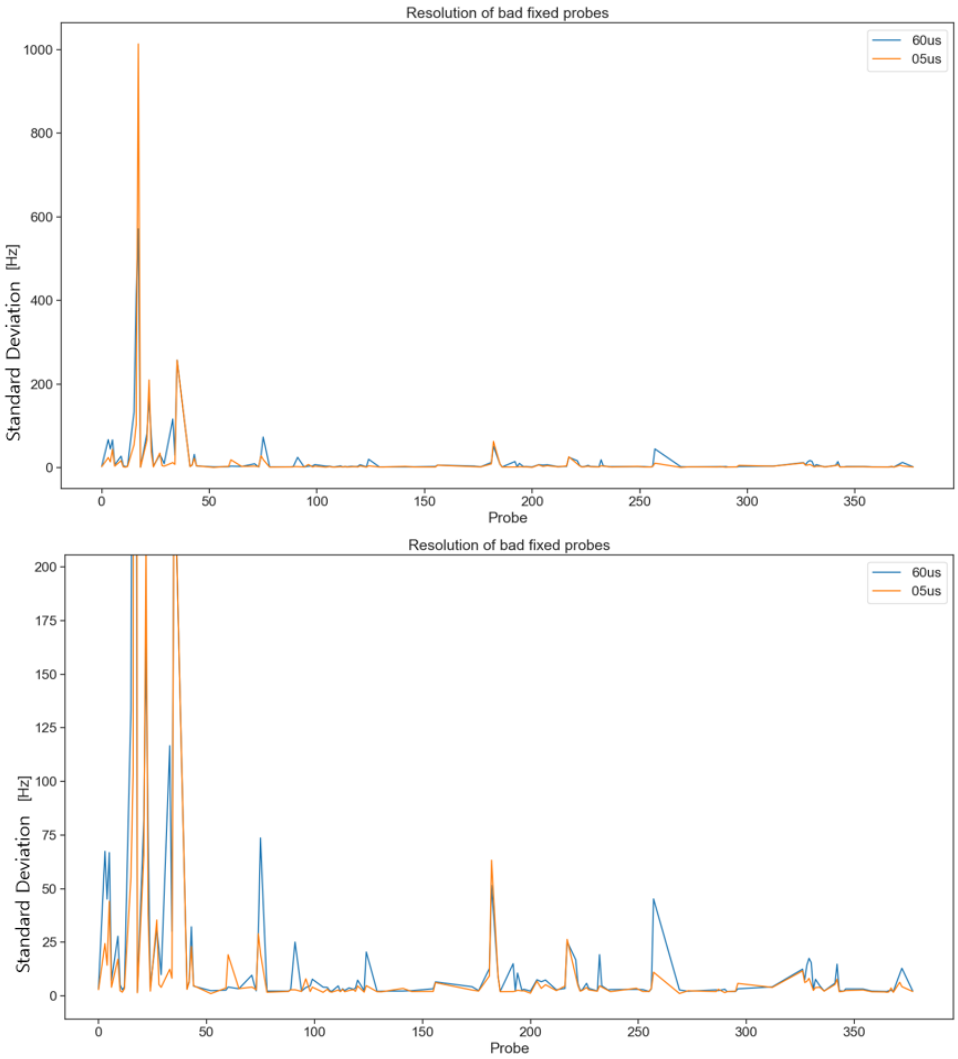

FIGURE 6.8: Top plot is the standard deviation of 132 fixed probes in Run 10220. The bottom plot is zoomed in on the y-axis ranging from 0 to 200 Hz from the top plot. The blue line is 60 μs EIW setting and the orange line is 5 μs EIW setting.

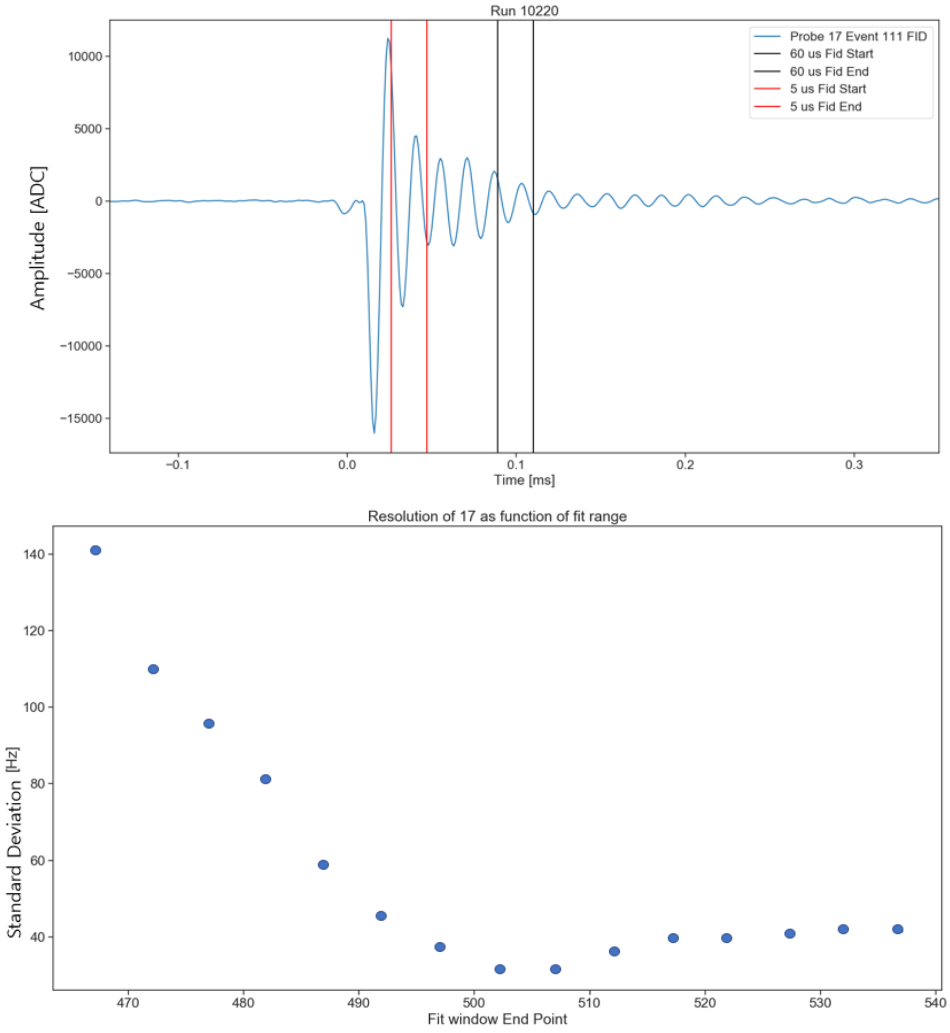

FIGURE 6.9: Top plot is probe 17's FID. Black vertical lines represent the fit window start and end (EIW: 60 μs). Red vertical lines represent the fit window start and end (EIW: 5 μs). The bottom plot is the standard deviations as a function of fit window end positions.

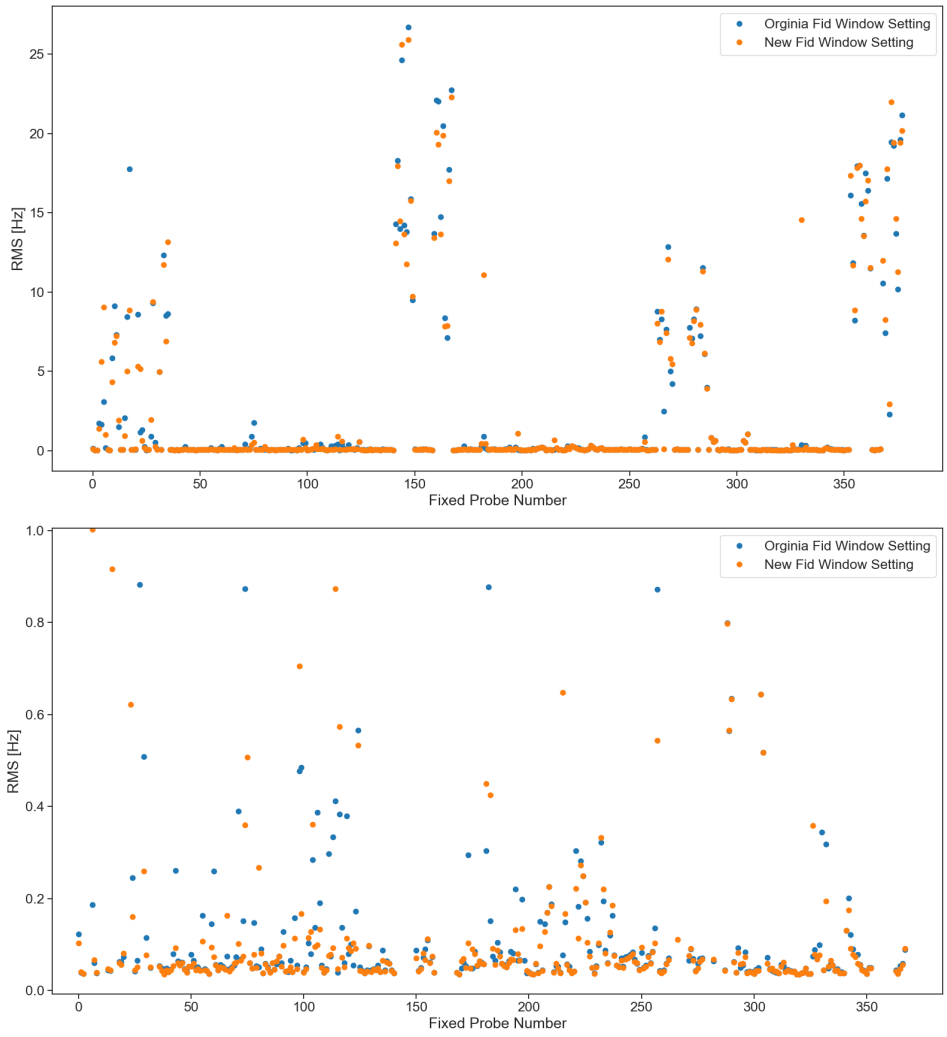

FIGURE 6.10: The top plot is RMS from Run 2 with two different fit window settings: default and new. The bottom plot is zoomed in on the y-axis ranging from 0 to 1 Hz of the top plot.

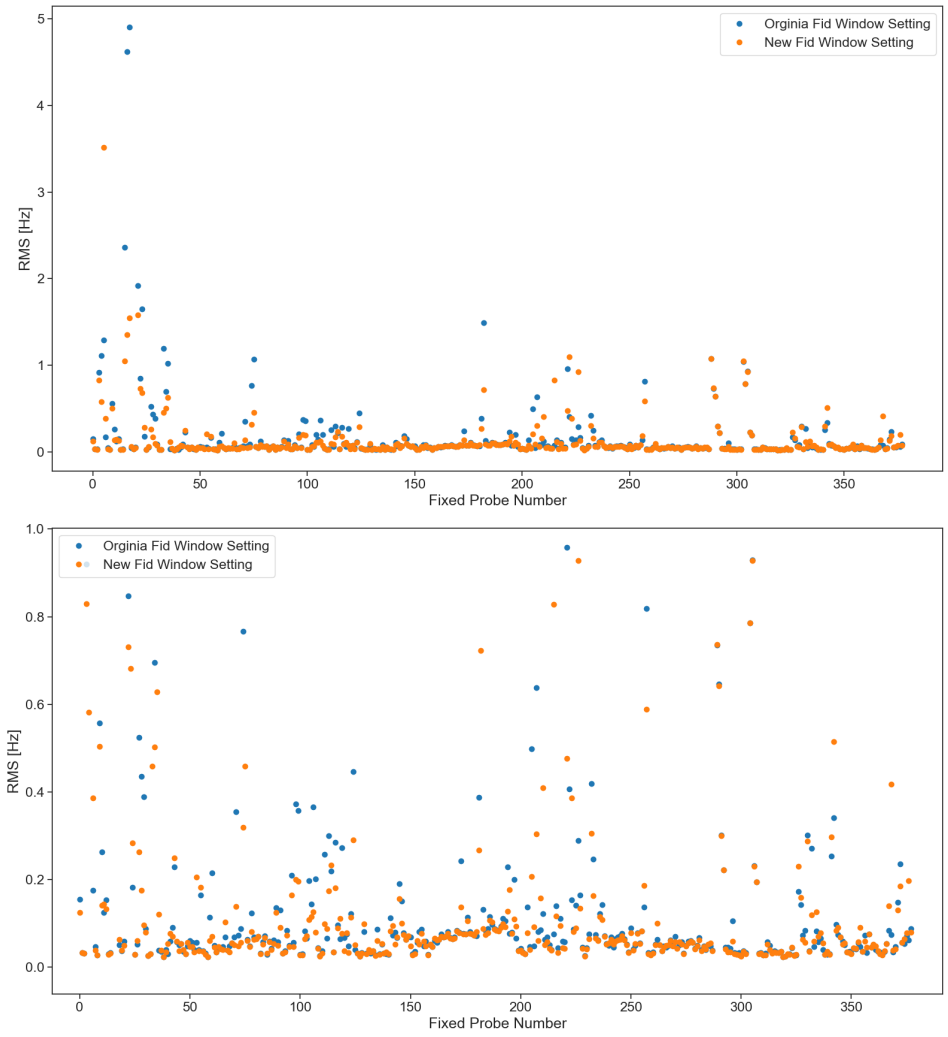

FIGURE 6.11: The top plot is RMS from Run 3 with two different fit window settings: default and new. The bottom plot is zoomed in on the y-axis ranging from 0 to 1 Hz of the top plot.

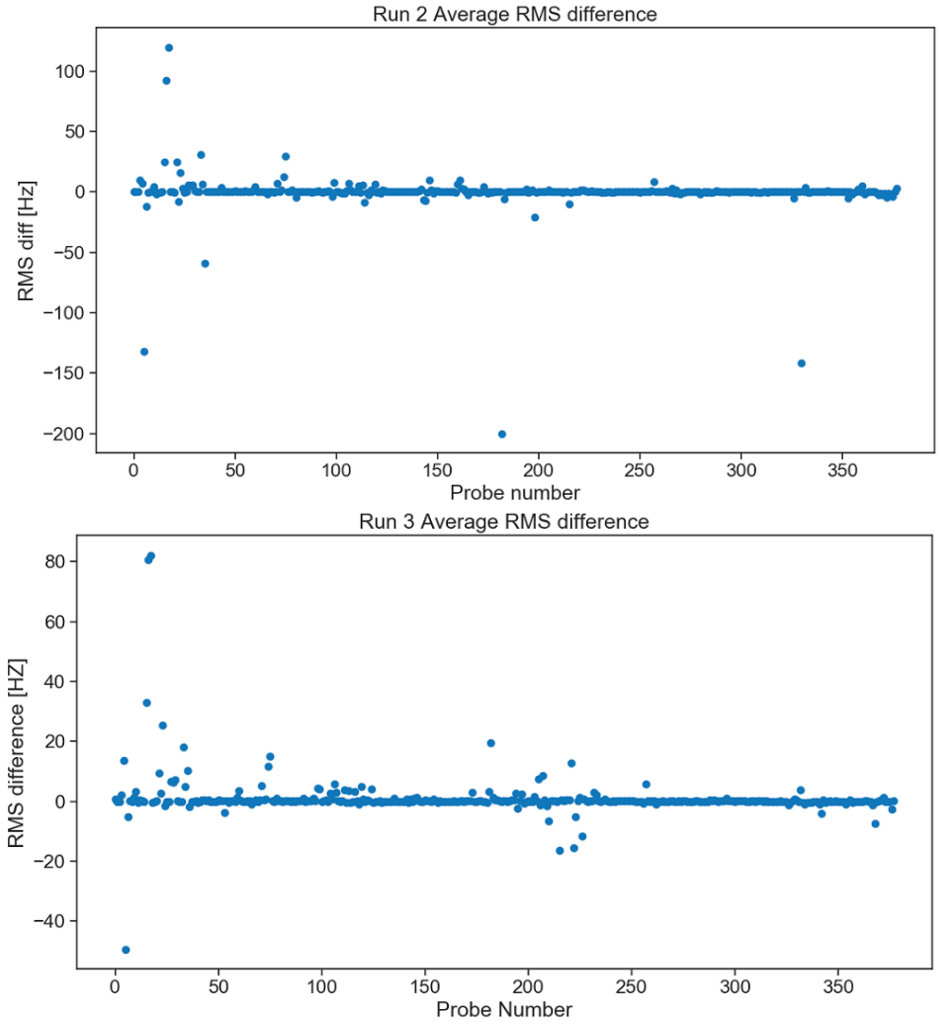

FIGURE 6.12: Run 2 and Run 3 mean frequency RMS with two different fit window settings from all datasets: default and new.

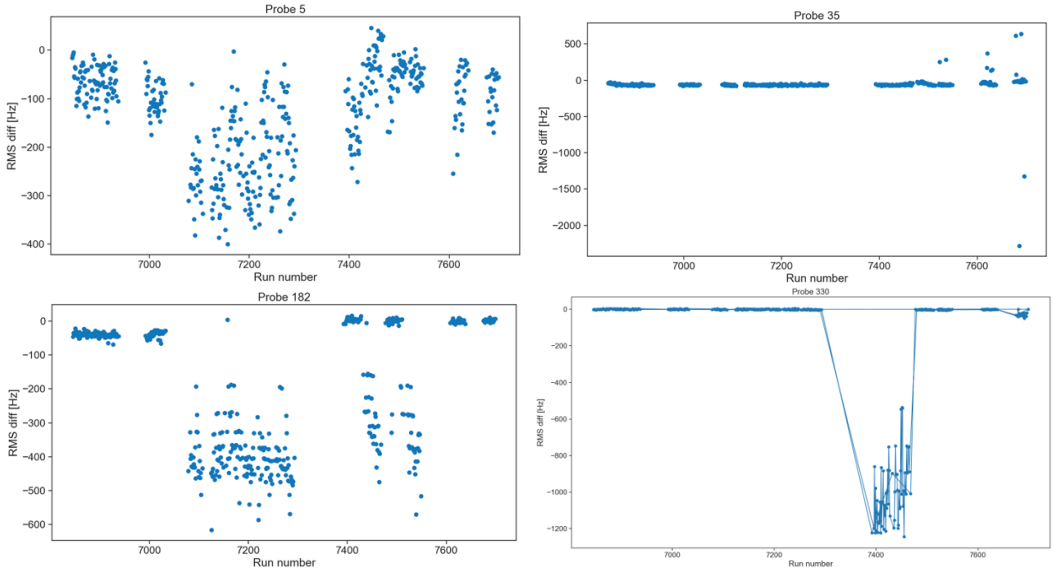

FIGURE 6.13: Four graphs represent RMS differences from selected probes (probe 5, probe 35, probe 182, and probe 330 in order) as a function of the Run numbers in Run 2.

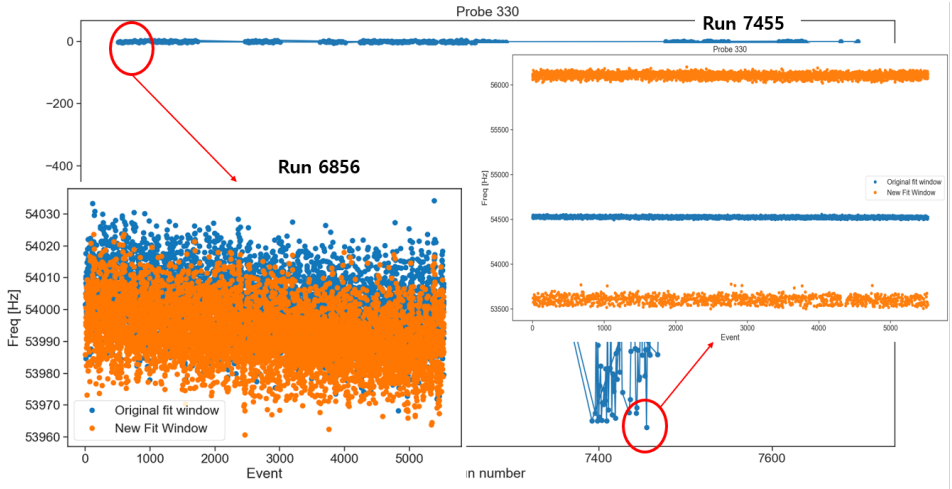

FIGURE 6.14: Further investigations on Run 2 probe 330. Two subplots are the frequencies as a function of events in two different runs: run 6856 and run 7455.

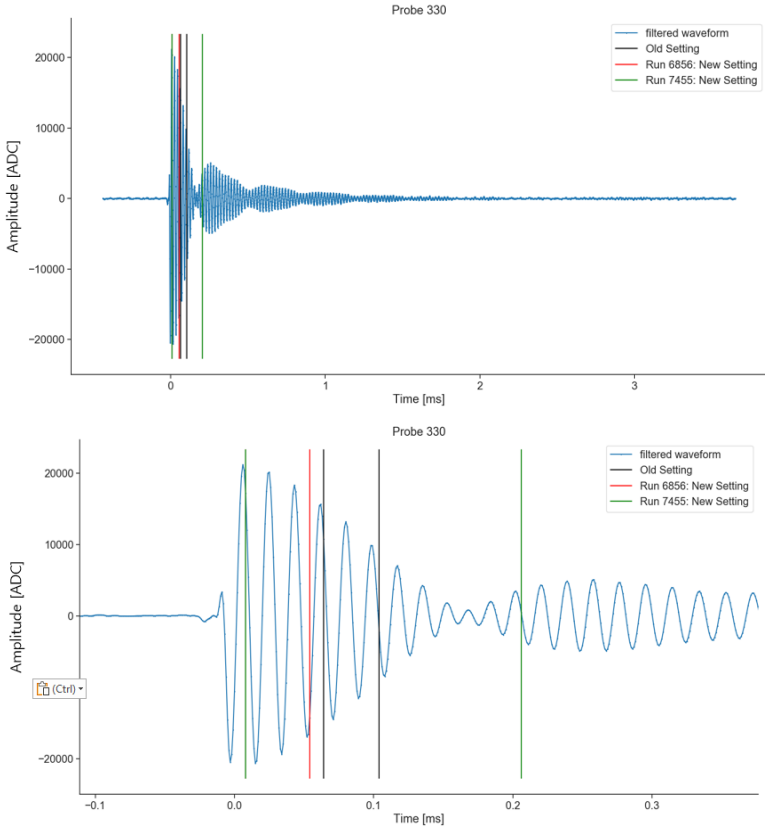

FIGURE 6.15: Probe 330 FID (Same plots with different scales). Black lines represent the old-fit window setting. Red lines represent the new fit window setting for run 6856. Green lines represent the new fit window setting for run 7455.

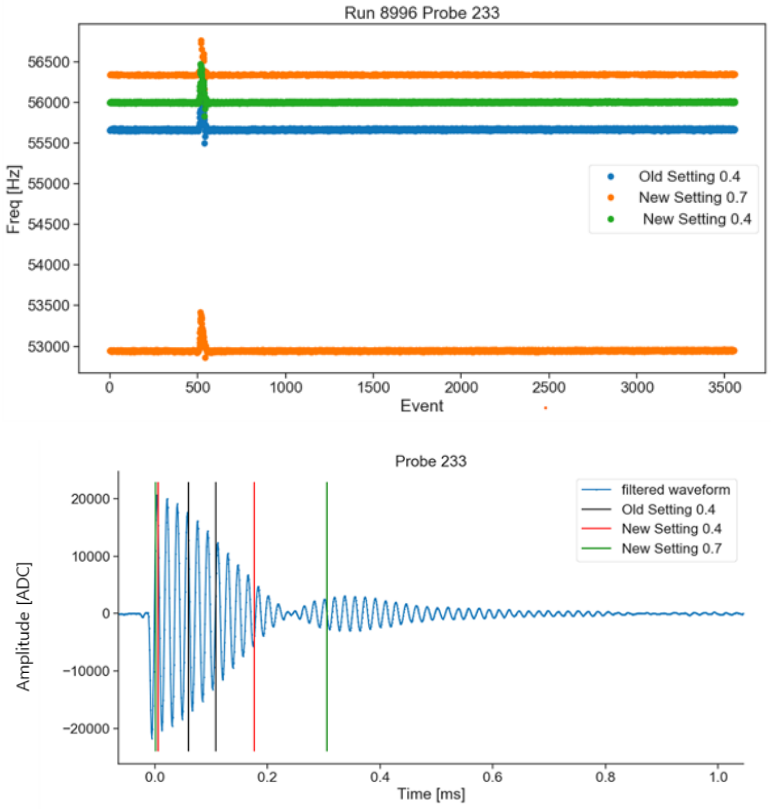

FIGURE 6.16: Top plot: Probe 233's frequencies as a function of events in run 8996 for three different settings: old fit window, new fit window 0.4, and new fit window 0.7. There is a jump in the middle of the plots due to the trolley's magnetic footprint. Bottom plot: Probe 233's FID with corresponding fit window ranges.

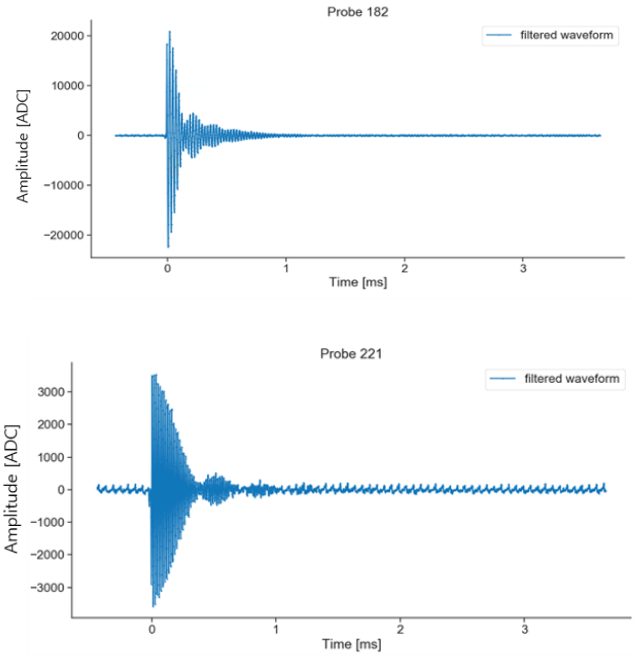

FIGURE 6.17: FIDs of probe 182 and probe 221

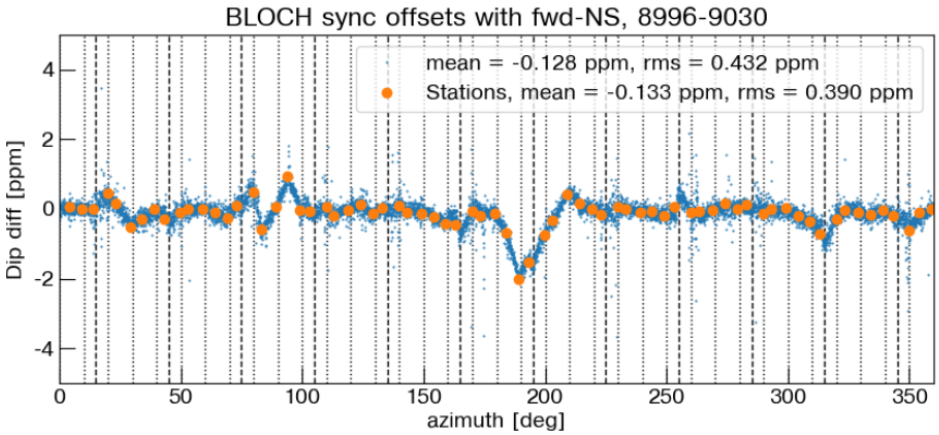

FIGURE 6.18: Azimuthaly resolved dipole *sync offset* of the **3d2** *trolley period* from the Bloch analysis.

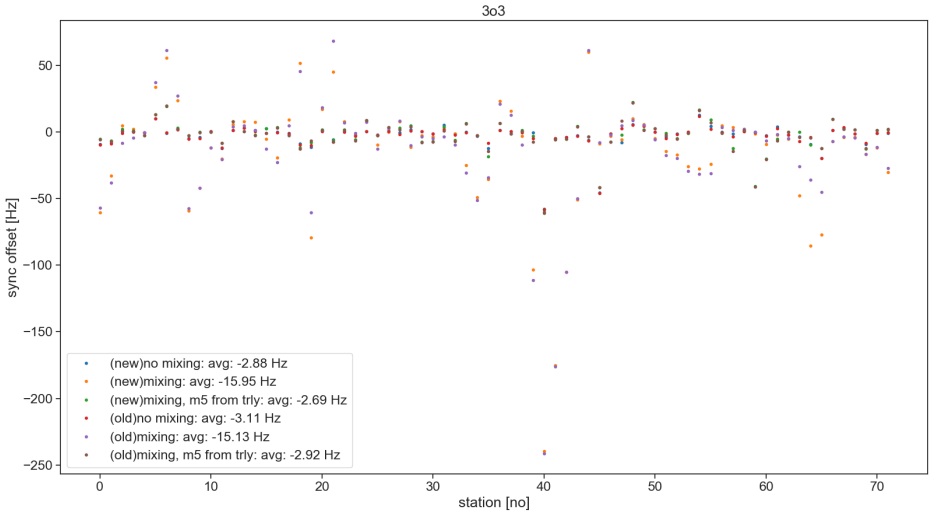

FIGURE 6.19: The **3o3** period two sync offsets, mixing and mixing with m5 from the trolley, with old and new fit windows as a function of station

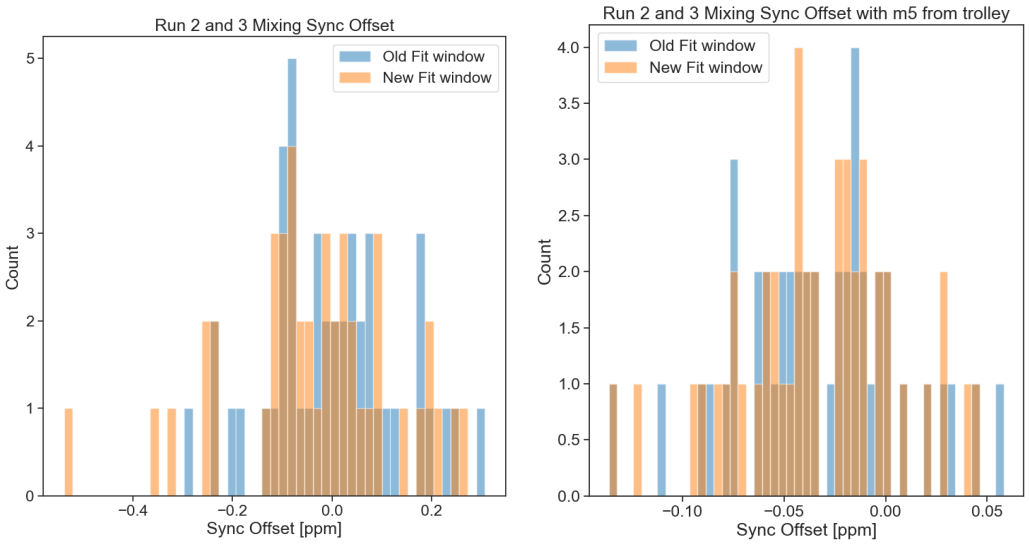

FIGURE 6.20: The two histograms, mixing and mixing with m5 from trolley, from Table 6.3.2 and Table 6.3.2.

Dataset		Mixing Avg		Mixing with m5, from trolley	
Run	Sub Run	Old [Hz]	New [Hz]	Old [Hz]	New [Hz]
3B	1	14.35	3.42	-2.62	-3.16
	2	-11.60	-14.58	-2.05	-2.27
	3	18.97	16.40	-1.05	-1.31
3C	1	-1.44	-15.34	-6.84	-7.47
3D	1	0.96	0.57	-3.95	-3.96
	2	-7.98	-7.80	-1.26	-1.07
	3	-5.15	-5.18	-1.04	-0.80
	4	12.31	11.90	0.10	-0.07
	5	1.69	1.33	-0.56	-0.71
3E	1	11.31	11.05	1.94	1.79
	2	-0.70	-0.45	-1.23	-1.28
	3	-4.58	-4.99	0.16	0.02
3F	1	2.58	-2.53	-5.54	-5.87
3G	1	11.02	8.97	-2.50	-2.69
	2	-5.44	-6.49	-2.23	-2.34
3J	1	3.85	1.24	-3.38	-3.51
	2	-1.63	-1.38	-2.61	-2.57
	3	4.98	5.41	-0.87	-0.83
3L	1	-12.26	-21.94	-8.19	-8.41
3M	1	-1.98	-6.68	-3.98	-4.48
	2	-14.71	-14.56	-3.14	-2.77
	3	4.68	4.36	0.64	0.52
3N	1	0.18	-0.39	-0.80	-0.88
	2	-6.25	-5.68	-1.40	-1.14
	3	15.09	15.47	1.76	1.72
	4	-7.54	-7.31	-1.46	-1.31
	5	-0.65	-1.29	-0.19	-0.14
3O	1	6.76	0.59	-5.38	-5.71
	2	-4.95	-5.61	-3.57	-3.63
	3	-15.13	-15.95	-2.92	-2.69

Table 6.3: The table is shown an average sync offset of the azimuthal of old and new fit window settings in two different sync offset measurements: Mixing and Mixing with the trolley's m5.

7

Trolley Probe FID Freq Extraction and Calibration

As described in Section 4.2 and 4.2.1, the trolley is the primary measurement tool to scan the field and generate the 2D field map periodically around the SR every 3 to 5 days when the muon beam is not present. There are 17 trolley probes inside the trolley which is made of aluminum. Because the trolley is made of aluminum, it perturbs the magnetic field locally. To measure the magnetic field that the muon sees when the trolley is not present, trolley probe calibration is necessary. In this chapter, I discuss an overview of the trolley FIDs and the detailed trolley calibration analysis.

7.1 Trolley FID Overview

The 17 NMR probes take measurements sequentially and hence the field in a helical pattern. In each measurement, the RF ($\pi/2$) pulse is pulsed 300 μs that lasts for 14 ms, and the baseline settles around 600 μs. For the trolley FID, the signal (waveform) from 650 μs to 12.6 ms is used. The reference frequency the trolley received is 61.74 MHz. The FIDs are mixed down to 50 kHz for a field around 1.45 T. The exact sampling period is $62.0/61.74 = 1.0004\mu s$. An example of a trolley FID is shown in

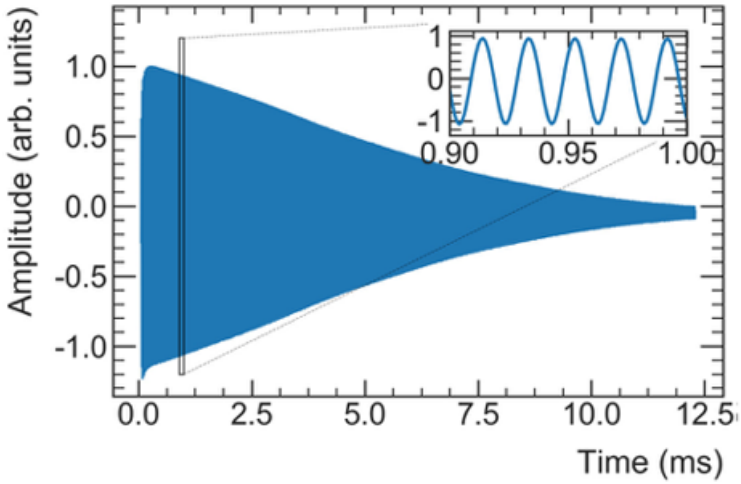

FIGURE 7.1: Typical Trolley FID.

Fig 7.1.

7.1.1 Optimization and Parameter Choices

Similar to the fixed probes analysis (Chapter 6), *Edge Ignore Window*, *smoothing parameters*, *frequency filter*, and *T0 shifts* are needed to be determined to a fixed constant for the trolley analysis. Here are the chosen empirical numbers for each analysis parameter:

- Edge Ignore Window: 60 μs
- Smooth parameters : 3 ($\approx$ 20 μs)
- Frequency filter: 0 Hz to 200 kHz
- FID truncation: 350^{th} event to 12600^{th} event
- T0 shifts : 350^{th} event

The fit window is also similar to the fixed probe analysis which is from the maximum amplitude to 1/e of the maximum amplitude. Then, 40% of a fit window is used for

the polynomial fit. Both linear and polynomial fit results are recorded, and analyzers choose either of them depending on the requirement of the resolution and accuracy. The resolution and uncertainty of the trolley probes are discussed more in Chapter 9.

7.2 Calibration

There are 17 trolley probes in an aluminum shell that contains the readout electronics. The materials, including the probes themselves, perturb the magnetic field. To correct the probe measurements to $\tilde{\omega}_p'$, the plunging probe - 1 NMR probe with pure water sample with known magnetic properties - is used for the calibration. In this section, I present the detailed procedures and analysis to evaluate the calibration constants.

7.2.1 Calibration Procedures and Technique

7.2.1.1 Overview

The calibration constant, CC_{raw}, is defined as the difference in frequency measurement between the plunging probe and selected trolley probe i, $CC_{\text{raw,i}} = f_{\text{pp,i}} - f_{\text{tr, i}}$ at the same position in space, as perfectly as possible, for this measurement. For the shielded proton correction, the calibration constant is adjusted to the new calibration constant, $CC_{34.7^{\circ}C}$. There are numbers of steps involved with determining the calibration constant and one of the key steps of the calibration procedure is to ensure that the plunging probe is aligned with the selected trolley probe, as perfectly as possible, within $0.5mm$ in each direction.

Therefore, the first step of the calibration procedures is a series of ΔB measurements to align the plunging probe to each selected trolley probe (see Section 7.2.1.2). During the ΔB measurements, the surface correction coils (SCC), which generate an imposed gradient in a single direction, are turned on and off. At the calibration

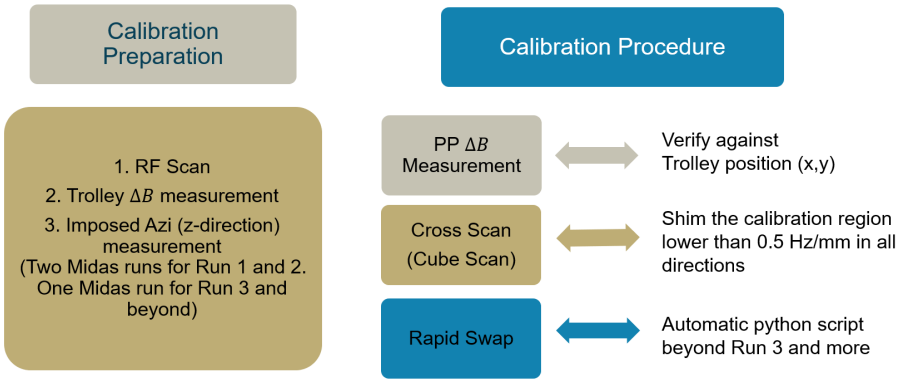

FIGURE 7.2: Calibration flow chart and procedure diagram

region, there are special coils that allow not only x and y direction gradients but also azimuthal z direction. The plunging probe and trolley probe are placed in the storage ring to measure the two field measurements when the SCC is on and off. The difference between these two measurements is called ΔB measurement. The plunging probe's ΔB measurement and trolley probe's ΔB measurement are exactly the same when the plunging probe and trolley probe measure the field at the exact same position. After ΔB measurement, the local field needs to be shimmed (see Section 7.2.1.3) to be highly uniform by adjusting the current to the SCC. Once the local field is uniform and stable, the rapid swap (see Section 7.2.1.4) is executed in which the plunging probes and trolley probes swap and measure the field in the same position 10 times. Fig 7.2 shows the diagram of the calibration procedure. Each of the steps will be discussed in later sections in more detail.

7.2.1.2 ΔB Measurement

The plunging probe must align with the selected trolley probe to evaluate a perfect calibration constant. This is almost impossible so the ΔB measurement is able to describe how close the two probes are in the calibration region. By adjusting the currents of the SCC, we can generate a linear imposed gradient in either a radial (x), vertical (y), or azimuth (z) direction. ΔB measurement defines that $\Delta B_{ij} =$

B_{ij}(SCC ON) − B_{ij}(SCC OFF) where the specific probe i are from 1 to 17 and the direction j are in either x, y, z. During the calibration campaign, there are two toggles for the plunging probe in all directions, two toggles for the trolley probe in the z direction, and four toggles for the trolley probe in the x and y directions. The power supply feedback must be off or paused - which means that the current is held during ΔB measurements - avoiding that the feedback reacts to the field changes seen by the fixed probe.

Then, the comparison between ΔB measurements between the plunging probe and trolley probe, $\Delta B(TR - PP) = \Delta B_{\mathrm{TR}} - \Delta B_{\mathrm{PP}}$, is used to estimate the relative position between them. The threshold is a 20 Hz difference, which means that the relative position offset between the plunging and trolley probe is within 0.5 mm in the x and y direction since gradients in the x, y directions, dB_x/dx and dB_y/dy, are about -40 Hz/mm. In the z direction, the threshold is a 5 Hz difference, which is 0.5 mm offset between, since a gradient in the z direction, dB_z/dz, is about - 10 Hz/mm.

7.2.1.3 Shimming the Field

The next step is shimming the field at the target position. The goal is to minimize the local gradients along x, y, and z directions to reduce the effects of the misalignment once ΔB measurements are done. During the calibration campaign in Run 1 and Run 2, only **cross scan** at the target position in all three directions is performed. However, for Run 3 and beyond, there are two shimming operations performed: **cross scan** and **cube scan**.

During the cross scan, there is a nine-point field map, 5 mm away from the target position in all directions, shown in the left diagram in Fig 7.3 and Table 7.1. The choice of 5 mm adjustment is due to the limitation of the trolley movements in the x,y, and z directions. Once the three-point scan is done, a second-order polynomial is used to fit it as a function of distances from the target. The gradient of the fit is called

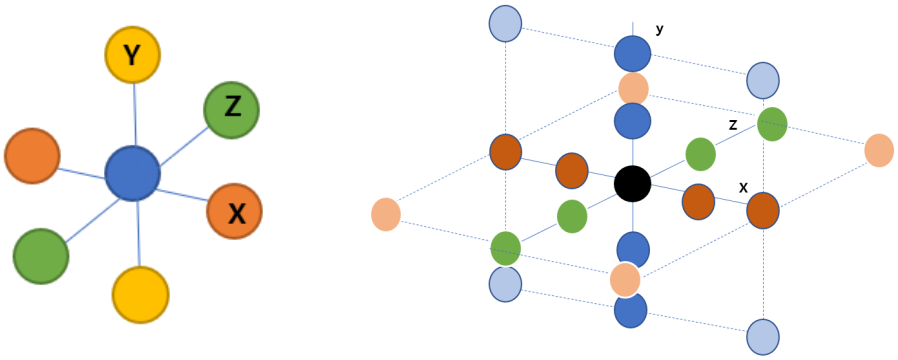

FIGURE 7.3: [Left] Cross Scan diagram. The blue dot is the target position and there is a nine-point field map: 3 from the x direction, 3 from the y direction, and 3 from the z direction. Each point is 5 mm apart. [Right] Cube Scan diagram. The black dot is the target position. Blue points, green points, and brown points are in the x, y, and z directions. There are other points that are combinations of x, y, and z directions

Scan	x	y	z
1	PP_x+5 mm	PP_y	PP_z
2	PP_x-5 mm	PP_y	PP_z
3	PP_x	PP_y	PP_z
4	PP_x	PP_y+5 mm	PP_z
5	PP_x	PP_y-5 mm	PP_z
6	PP_x	PP_y	PP_z
7	PP_x	PP_y	PP_z+5 mm
8	PP_x	PP_y	PP_z-5 mm
9	PP_x	PP_y	PP_z

Table 7.1: Nine-point Scan. PP means Plunging Probe

the *shimmed gradients*. Then the SCC configuration file is adjusted for shimming the field to high uniformity. The cross scan is repeated until the gradient is acceptable for rapid swapping, which is less than 20 ppb/mm, in all directions.

After the cross scan, the cube scan is performed, which are multiple-point measurements, about a 32-point scan, shown in Fig 2. Not only in the x, y, and z direction scans, but also in combinations of x and y, y and z, and z and x scans that are measured to gather more information about cross terms for the uncertainty study. Detail

scan orders can be found in Table 7.2. Once both cross and cube scans are done, the final step is the rapid swap.

7.2.1.4 Rapid Swap

The rapid swap procedure is where the selected trolley probe and plunging probe are swapped at the target position to measure the magnetic field. Python script automatically operates 10 swaps that take about one and a half hours. The trolley moves back to a 180-degree position (about azimuthally 10 degrees away from the target position) during the plunging probe measurements and the plunging probe extracts as the selected trolley measures the field. Each measurement takes 30 seconds after the complete stop. The difference between the two field measurements is the raw calibration constant without any misalignment and other corrections. The reason for 10 swaps during the rapid swap process is to reduce any bias and obtain good statistical uncertainty.

7.2.2 Analysis Detail

7.2.2.1 Overview of the Analysis

From rapid swapping, the raw calibration constant, without alignment and temperature correction, is the difference of the field measurements between the selected trolley probe and plunging probe which is $CC_{\mathrm{raw},i} = B_{\mathrm{PP},i} - B_{\mathrm{TR},i}$, where i is the selection of probes from 1 to 17. The full calibration constant is defined as

$$CC_{34.7^{\circ}C,i} = B_{\mathrm{PP},i} - B_{\mathrm{TR},i} + \sum_{q=\mathrm{x,y,z}} B_{\mathrm{mis},i} + B_{\mathrm{bar},i} + \mathrm{temp}_{\mathrm{corr}} \tag{7.1}$$

where $\sum_{q=x,y,z} B_{\mathrm{mis},i}$ is the misalignment correction term in different directions x, y, and z, $B_{\mathrm{bar},i}$ is the barcode correction for trolley positions, and $\mathrm{temp}_{\mathrm{corr}}$ is the temperature and shielded proton correction to the reference temperature, $34.7^{\circ}C$. Temperature and shielded corrections are discussed in Section 7.2.2.6. The misalign-

Scan	x	y	z
1	PP_x	PP_y	PP_z
2	PP_x	PP_y+5 mm	PP_z
3	PP_x+5 mm	PP_y+5 mm	PP_z
4	PP_x-5 mm	PP_y+5 mm	PP_z
5	PP_x	PP_y+5 mm	PP_z
6	PP_x	PP_y+2.5 mm	PP_z
7	PP_x	PP_y-5 mm	PP_z
8	PP_x+5 mm	PP_y-5 mm	PP_z
9	PP_x-5 mm	PP_y-5 mm	PP_z
10	PP_x	PP_y-2.5 mm	PP_z
11	PP_x	PP_y	PP_z
12	PP_x+5 mm	PP_y	PP_z
13	PP_x+2.5 mm	PP_y	PP_z
14	PP_x-5 mm	PP_y	PP_z
15	PP_x-2.5 mm	PP_y	PP_z
16	PP_x	PP_y	PP_z
17	PP_x	PP_y	PP_z-5 mm
18	PP_x	PP_y-5 mm	PP_z-5 mm
19	PP_x	PP_y+5 mm	PP_z-5 mm
20	PP_x	PP_y	PP_z-5 mm
21	PP_x	PP_y	PP_z
22	PP_x	PP_y	PP_z-5 mm
23	PP_x+5 mm	PP_y	PP_z-5 mm
24	PP_x-5 mm	PP_y	PP_z-5 mm
25	PP_x	PP_y	PP_z-2.5 mm
26	PP_x	PP_y	PP_z
27	PP_x	PP_y	PP_z+2.5 mm
28	PP_x	PP_y	PP_z+5 mm
29	PP_x	PP_y-5 mm	PP_z+5 mm
30	PP_x	PP_y+5 mm	PP_z+5 mm
31	PP_x	PP_y	PP_z+5 mm
32	PP_x	PP_y	PP_z
33	PP_x	PP_y	PP_z+5 mm
34	PP_x+5 mm	PP_y	PP_z+5 mm
35	PP_x-5 mm	PP_y	PP_z+5 mm
36	PP_x	PP_y	PP_z+5 mm
37	PP_x	PP_y	PP_z

Table 7.2: Cube Scan. PP means Plunging Probe

ment correction can be expressed as,

$$B_{\mathrm{mis},i} = \left.\frac{dB_s}{dq}\right|_{q=0} \cdot \frac{\Delta B(\mathrm{TR\ -\ PP})}{dB_{\mathrm{imp}}/dq}, \tag{7.2}$$

where dB_s/dq is the shimmed gradient from cross and cube scans, ΔB(TR - PP) is the difference ΔB measurements between the selected trolley probe and plunging probe, and dB_{imp}/dq is the imposed gradient from ΔB measurements.

7.2.2.2 Rapid Swap Analysis

During rapid swapping, the trolley probe and plunging probe measure each other 10 times at the target position. In a perfect world, the trolley would stop at the same position 10 times, the field would always be uniform, and there would be no oscillations and drifts. However, these conditions are not held. There are following corrections needed to be done in the rapid swap analysis:

- Oscillation correction
- Barcode correction
- Field drift correction
- Temperature correction

Barcode and field drift corrections are done after extracting the frequencies from each probe. Oscillation and temperature corrections must be done measurement by measurement.

Plunging Probe

The plunging probe takes measurements when it gets triggered, so data selection is not needed. Once the plunging probe arrives at the target position, it has 30 seconds to measure the field. During these 30 seconds, the plunging probe takes 6 data points.

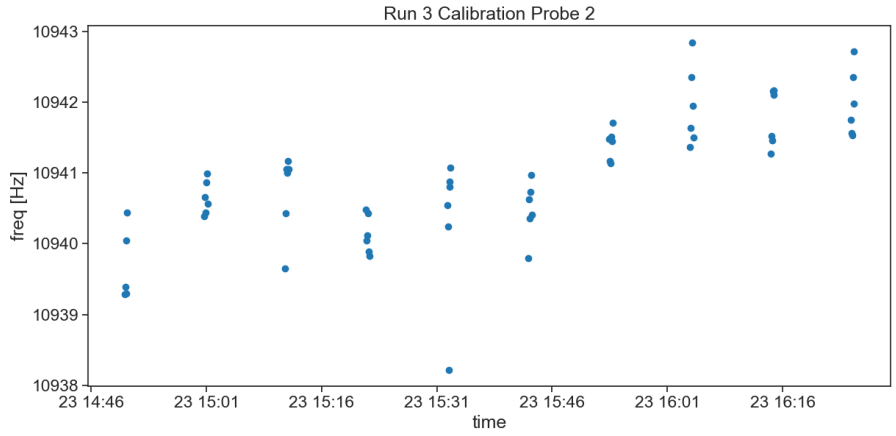

FIGURE 7.4: Run 3 probe 2 calibration campaign (rapid swap): plunging probe measurements for 10 swaps.

There is a total of 60 data points per probe for 10 swaps. Fig 7.4 shows the plunging probe's six measurements per swap during rapid swapping in the Run 3 probe 2 calibration campaign. I use the mean and standard deviation of the six-point scans as swap frequencies and uncertainties.

Trolley Probe

Unlike the plunging probe, the trolley probe takes data continuously during rapid swapping. Therefore, data selection is necessary. The field measurements need to be selected where the trolley probe is located at the target position for 30 seconds. Fig 4 shows the probe 2 trolley measurements during rapid swapping. While the trolley is moving, frequency measurements are changing dramatically. When the trolley stops, the spread of the frequency measurements is less than a few Hz so that it is a flat horizontal line on the plot without zooming in. The trolley stops either at 180 degrees during the plunging probe measurements or roughly at 189 degrees at the target position.

The data selection procedure consists of two steps. As the first step, I look at the Root Mean Square (RMS) of the nearest five data points to determine where

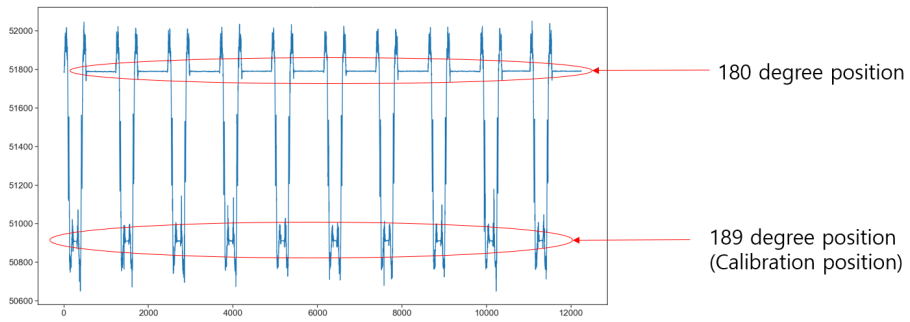

FIGURE 7.5: Run 3 probe 2 calibration campaign: (rapid swap) trolley probe measurement. The y-axis is frequencies in Hz and the x-axis is events (sample) or data points during rapid swapping. The top flat lines are when the trolley is at 180 degrees while the plunging probe takes measurements. I want to select the data where the trolley is at 189 degrees which is the target position.

the trolley stops. Then, I look at the length of the stopping time to determine the trolley at the target position and finalize the data selection. While the trolley is moving, the frequency measurements are changing dramatically so that the RMS of the nearest five data points must be huge. I set each probe with the appropriate threshold to determine whether the trolley is moving or not shown in Table 7.3. I set different thresholds for each probe because of the different probe locations in the trolley. Once I find where the trolley stops, I need to select the data where the trolley is at the target position. Fig 7.5 shows that the stopping time of the trolley at 180 degrees is much longer than the stopping time of the trolley at the target position, approximately at 189 degrees, because the plunging probe needs longer time to insert, measure, and extract while the trolley stops at 180 degrees. I set the threshold of 200 events, approximately 90 seconds, to select the data. Then, the first 20 events are skipped to avoid any mechanical bias or uncertainty. Fig 7.6 shows that the red marks represent the data selection for the analysis. The mean and RMS of the selected data regions for each swap represent the trolley field measurement and uncertainty for each swap.

Probe	Threshold [Hz]
1	1.5
2	1.5
3	1.5
4	3.0
5	3.0
6	4.0
7	3.0
8	10.0
9	3.0
10	3.0
11	4.0
12	4.0
13	3.0
14	3.0
15	3.0
16	3.0
17	7.0

Table 7.3: Rapid Swap RMS Thresholds for Trolley Probes

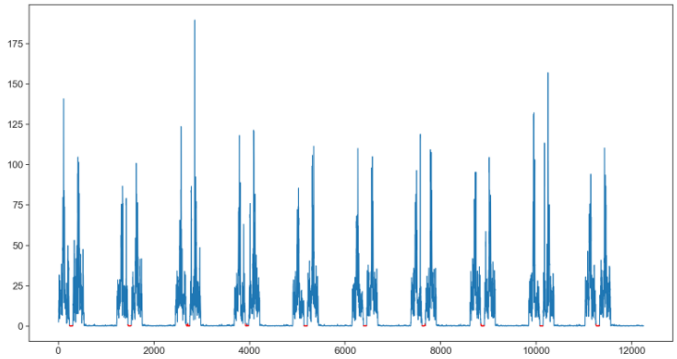

FIGURE 7.6: Run 3 probe 2 calibration campaign: (rapid swap) RMS plot from trolley probe measurements. The y-axis is the RMS in Hz and the x-axis is events (sample) or data points during rapid swapping. Red marks represent where I select the data for the analysis.

Oscillation Correction

During the calibration campaign, an oscillation with a period of two minutes can be observed. Both the plunging probe and trolley probe measurements take about 30 seconds, which is one-quarter of the oscillation period. Therefore, the oscillation perturbs the data measurements. To correct the perturbation, first, I generate the oscillation signals. Then, I apply local offsets to the measurement. Here are the detailed steps on how to generate the oscillation signals:

- Calculate the average frequency f_i of the selected fixed probes for i events
- Calculate the average of the frequencies f_{ave} of f_i for all events
- Define the oscillation signals as $f_i - f_{\text{ave}}$

To evaluate the oscillation patterns, half of the total numbers of the fixed probes are chosen which are from 90 to 270 degrees. However, the fixed probes that are located in the regions where the trolley moves around must be excluded because of the field perturbation. Therefore, fixed probes from 90 to 180 degrees and 190 to 270 degrees are first selected, which is a total of 180 fixed probes. To remove noises and spikes, I look at each individual 180 fixed probes and measure the resolution (RMS) of the measurements. Then, I remove the fixed probes that are worse than 50 ppb resolution from the selection. As a result, each probe in the calibration campaign has different numbers of the selected fixed probe. Fig 7.7 shows the oscillation signal of probe 2.

Once the oscillation signal is generated for each probe, I apply the oscillation correction to each trolley and plunging probe rapid swap data. Here are the steps on how I apply the correction:

- Find the corresponding frequency of the event i at the time the event occurred by using interpolation from the oscillation signal, f_i.

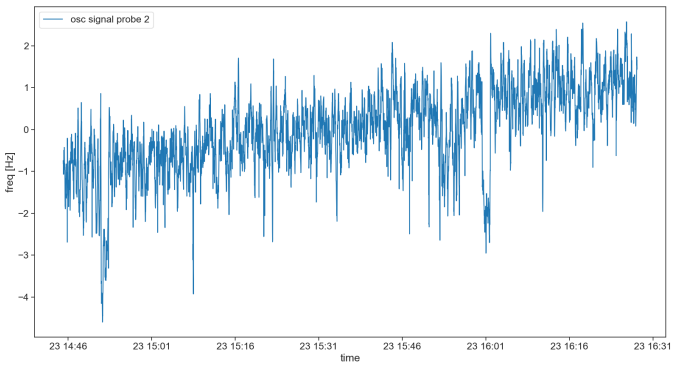

FIGURE 7.7: The oscillation signal for probe 2

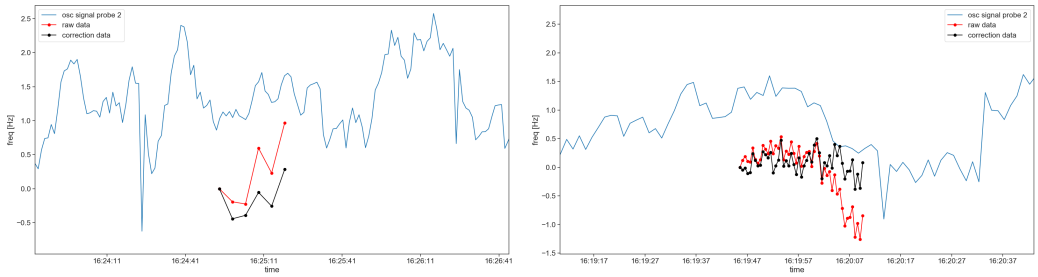

FIGURE 7.8: Blue line represents the oscillation signal for probe 2. The left plot is plunging probe data and the right plot is trolley probe data for 10^{th} swap for probe 2 rapid swap. Red dots and black dots represent raw and correction measurements.

- Apply the offset, f_i, to the frequency measurement by plunging and trolley probe.

Comparisons between the raw and correction measurements of the last swap for both the trolley and plunging probe of the probe 2 rapid swap measurements are shown in Fig 7.8.

The oscillation correction does not affect the frequency and uncertainty significantly, but it helps to reduce the oscillation pattern. After the application of the oscillation correction, the plunging probe improves by 2.6 ppb and the trolley probe improves by 3.5 ppb in uncertainty resulting in the average of all rapid swaps of 17 probes.

FIGURE 7.9: Two different barcode marks on the trolley track. (The drawing is Not in Scale)

Barcode Correction

During rapid swapping, even running by automatic operation by a Python script, the trolley is not able to stop at the same exact spot 10 times (or 10 swaps). The trolley position is usually measured by the encoder, but the encoder position is not accurate enough due to an uneven backlash and tension of the cable over time. Therefore, the trolley position is different for each swap and the offset is needed to evaluate with respect to the first swap. Beside the encoder position, there is another position measurement method called the **Barcode Position**. There are two marks on the trolley track: Regular mark and Absolute mark. While the trolley is moving, there are 2 sets of LED lights and sensors equipped at the bottom of the trolley that read the barcode on the track by collecting *the light reflection (voltage)* signals as the barcode signal. When the trolley passes the white gap, the voltage is at the maximum, and when the trolley passes the black mark, the voltage is at the minimum, so the voltage-position plot has close to a sine function. The diagram of how the marks look on the track is shown in Fig 7.9. The gap between the two regular marks is about 1.95 mm and there are 30 reg marks between the two neighbor absolute mark groups. Each absolute mark group represents a unique binary number to indicate the position.

I am unable to use the barcode position determination in the calibration directly to figure out where the trolley is at in the calibration region because of the trolley motion during rapid swapping: moving back and forth. Barcode position is determined by matching the absolute/regular barcode to the database between 2 regular

marks. However, the trolley is not able to get 2 regular marks because it stops and does not collect the second (next barcode) mark. Therefore, there is up to 1.95 mm offset from the last barcode mark that the trolley read, which is not able to find the exact position of the trolley directly from the database. Here is the method to find the trolley position without the second marker position.

- Pick one trolley dataset to create the ***voltage*** database.
- Find the extremes of the trolley measurement.
- Use the ***voltage*** database to find the unseen extreme.
- Create the template function to determine the trolley position.

The idea is to use normal trolley runs as the database to predict the trolley position in rapid swaps during the calibration campaign. In order to use normal trolley runs as the database, the barcode signals from normal trolley runs must be identical and repeatable. The barcode signals from different trolley runs are shown in Fig 7.10 and plots from each of the three trolley run from the Run 3 dataset are almost identical and verify that the barcode signal (voltage-position relationship) is highly repeatable. I pick Run 10225 as the dataset for the Run 3 calibration analysis. Due to the 2 sets of LED lights and sensors equipped at the bottom of the trolley, the voltage between two extremes indicates the position of the trolley. Fig 7.11 shows the barcode signal and Vol_{diff} of Run 10225. From the reference [84], the voltage difference, $Vol_{\boldsymbol{diff}}$, between extremes are stable within 0.01 V. By using Vol_{diff}, the unseen regular mark can be predicted.

Once the database is ready, the extremes are found from the measurements from each swap of the rapid swap of the selected probe run. Because Vol_{diff} is also highly repeatable, I match each swap extreme data to the database shown in Fig 7.12. After matching, based on the database, the unseen regular mark is predicted. In the last

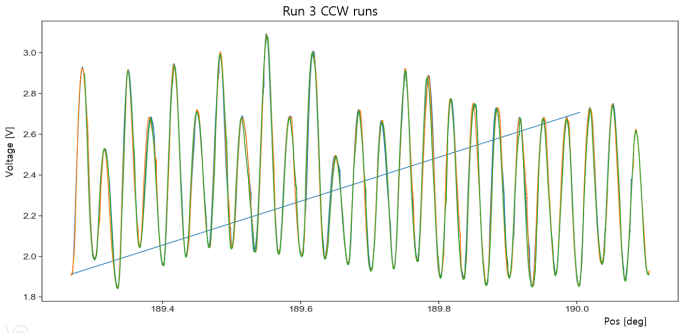

FIGURE 7.10: Barcode signal of three Run 3 CCW: Run 10148 (blue), Run 10191 (orange), and Run 10225(green)

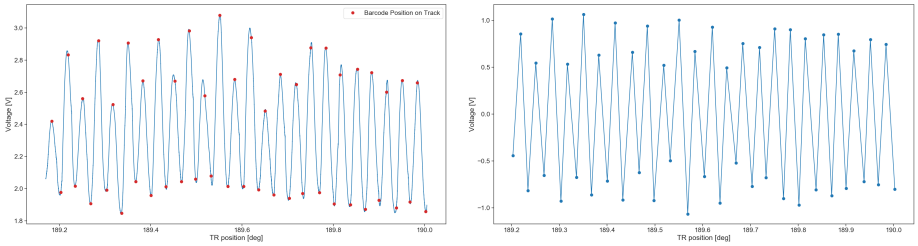

FIGURE 7.11: Left: Barcode Signal of Run 10225. Red marks represent Barcode Position in the system. Right: Vol_{diff} of Run 10225

step of the method, after predicting the unseen regular mark, the template function is created to determine the final trolley position. The template function is expressed as:

$$
\begin{aligned}
Vol &= A\sin\left(k(pos - pos_{\text{reg}}) + b\right) + B \\
A &= \frac{|Start_{\text{vol}} - end_{\text{vol}}|}{2} \\
B &= \frac{|Start_{\text{vol}} + end_{\text{vol}}|}{2} \\
k &= \frac{\pi}{pos_{\text{reg}} - pos_{\text{unseen}}} \\
b &= -\frac{\pi}{2}.
\end{aligned}
\tag{7.3}
$$

Then, from equation 7.3, the final position is defined as:

$$
pos = pos_{\text{reg}} + \frac{1}{k}\arcsin\left(\frac{Vol - B}{A}\right) - \frac{b}{k} \tag{7.4}
$$

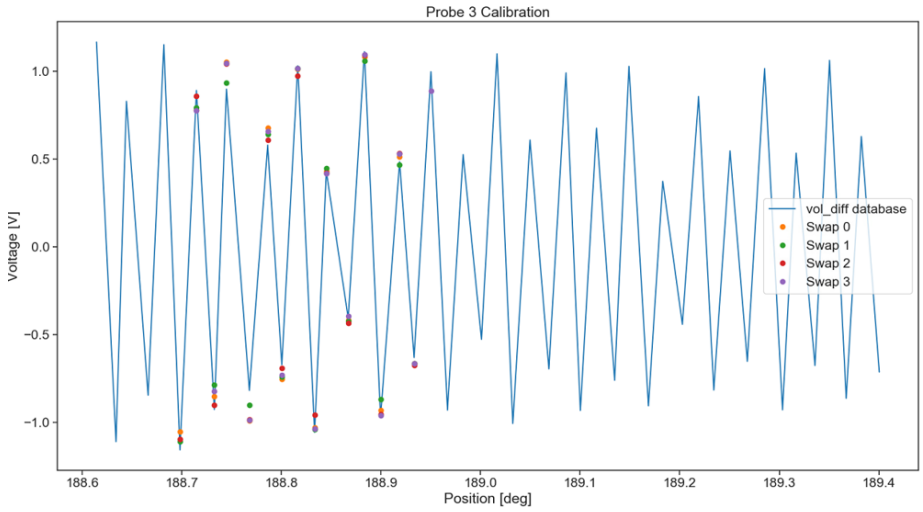

FIGURE 7.12: Matching probe 3 extreme data from swap 0 to 3 to the database (Run 10225)

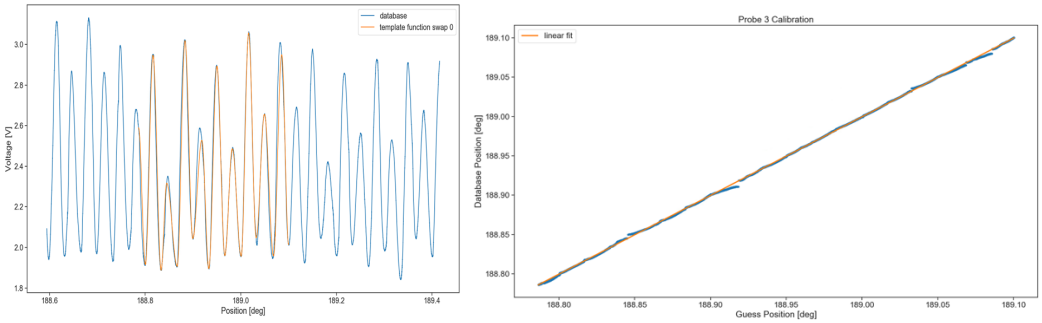

FIGURE 7.13: Left: Blue line represents the barcode signal of Run 10225 and the orange line represents the guess position or the barcode signal from the method of the first swap of Probe 3. Right: the linear relationship between the guess position and the real position

The position template function for the first swap of probe 3 is shown in Fig 7.13. The real position and guess position signals are almost matched and the linear relationship with the coefficient of the slope, $1.0000 \pm 5.1415 \times 10^{-5}$ and the correlation, 0.9999. Offsets are the difference between each swap's final position and the first swap position since the first swap position is the reference point because that's the only swap that ΔB is measured during the calibration campaign. The result is shown in Table 7.4.

Probe	swap1	swap2	swap3	swap4	swap5	swap6	swap7	swap8	swap9	swap10
1	0.00	-0.45	-0.43	-0.37	0.20	-0.05	0.15	-0.40	0.25	-0.04
2	0.00	1.22	-0.42	-0.21	-0.17	2.94	0.09	1.05	-0.39	1.13
3	0.00	0.32	0.04	1.84	0.05	0.53	1.88	-0.03	0.69	0.82
4	0.00	-0.20	0.23	-0.98	-0.12	-0.14	0.01	0.13	0.21	-1.15
5	0.00	-0.01	-0.08	-0.01	0.14	0.63	-0.31	0.68	0.27	0.81
6	0.00	-0.08	0.00	0.11	0.08	-0.05	0.06	-0.05	-0.08	-0.03
7	0.00	-0.04	-0.17	-0.09	-0.07	-0.01	-0.19	-0.13	-0.16	-0.17
8	0.00	-1.66	0.39	0.02	-0.06	-0.44	0.26	-0.51	-0.49	-0.45
9	0.00	0.12	1.03	0.98	0.95	1.00	-0.80	1.16	-0.21	-1.80
10	0.00	0.41	1.41	0.16	0.78	0.20	0.43	1.10	1.12	0.05
11	0.00	0.00	-0.23	-0.22	-0.13	-0.21	-0.06	-0.01	-0.26	-0.08
12	0.00	-0.43	-0.01	-0.48	0.52	0.11	0.62	-2.32	0.05	0.11
13	0.00	-0.02	-0.02	-0.06	-0.03	-0.04	-0.03	-0.03	-0.01	-0.05
14	0.00	0.01	0.00	0.01	0.00	0.09	0.04	0.05	0.07	0.03
15	0.00	-0.31	-0.08	-0.87	0.00	-0.67	-0.37	-0.45	-0.09	-0.13
16	0.00	-0.09	-0.19	-0.27	0.20	0.00	-0.14	0.30	-0.27	0.33
17	0.00	0.24	0.25	-0.11	-0.01	-0.01	0.07	-0.01	0.06	-0.01

Table 7.4: Barcode Correction results. Unit: Hz

Field Drift Correction

The rapid swap measurements take about 1.5 to 2 hours. During this time, the field is drifting and this drift perturbs the measurement significantly. To correct the field drift over time, the ABA method is used in the analysis. Fig 7.14 shows the scheme of the ABA method: the combination of trolley (A) - plunging (B)- trolley (A) measurements. Let's assume the field has a linear drift with slope c. At the time t_1, the frequency from the trolley probe is $B_1 = B_0 + c \cdot t_1$. At the time t_2, the frequency from the plunging probe is $B_2 = B_0 + b + c \cdot t_2$, where b is the perturbation of the field because of the swapping from the trolley to the plunging probe. At the time t_3, the frequency from the trolley probe again, after retracting the plunging probe, is $B_3 = B_0 + c \cdot t_3$. To remove the drift and calculate the perturbation b is used:

$$b = \frac{t_3 - t_2}{t_3 - t_1}(B_2 - B_1) + \frac{t_2 - t_1}{t_3 - t_1}(B_2 - B_3) \tag{7.5}$$

The coefficient $(t_3 - t_2)/(t_3 - t_1)$ and $(t_2 - t_1)/(t_3 - t_1)$ are time-weighted coefficient,

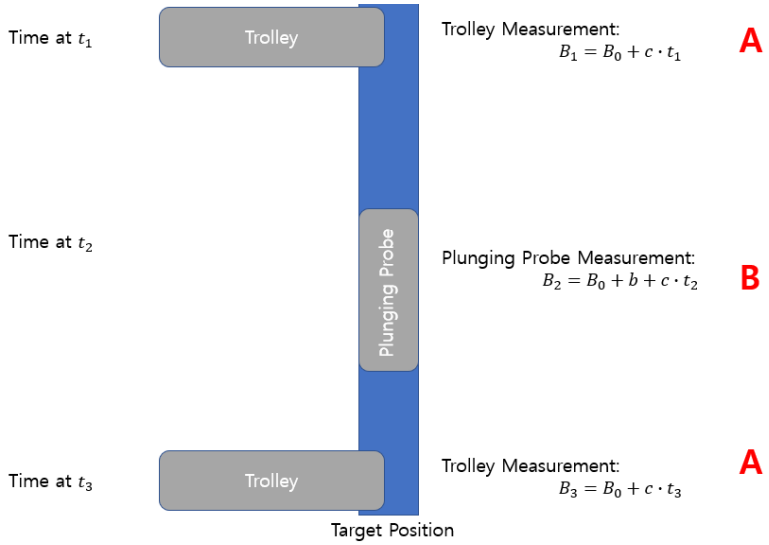

FIGURE 7.14: Schematic of ABA method: trolley - plunging -trolley combination

which are defined as ω_1 and ω_2. The uncertainty of the ABA method is expressed:

$$\delta b^2 = \omega_1^2 \delta B_1^2 + \omega_2^2 \delta B_3^2 + (1 - 2\omega_1\omega_2)\delta B_2^2 \tag{7.6}$$

There are 10 swaps per rapid swap. Therefore, there are 9 combinations for each probe from the ABA method. For example, the first b is from the first swap of the trolley and plunging and the second swap of the trolley. The second b is from the second swap of the trolley and plunging and the third swap of the trolley and so on. A total of nine b measurements are calculated from the ABA methods for each rapid swap. When I average the final nine b values, the measurements become correlated because chains of the ABA methods overlap swapping measurements. Instead of chains of the ABA methods, to avoid the measurement correlations, I make ABA, BAB, ABA, and so on without overlapping data. In this case, it would be easier to alternate the uncertainty. The uncertainty δb is the square root of the quadratic summation of alternate uncertainties. Fig 7.15 shows the ABA results for probe 6. The blue markers are from the raw data, which is the difference between the plunging and trolley-swapping measurements. The green markers are from ABA methods. The green markers have smaller error bars and are flatter than the blue markers.

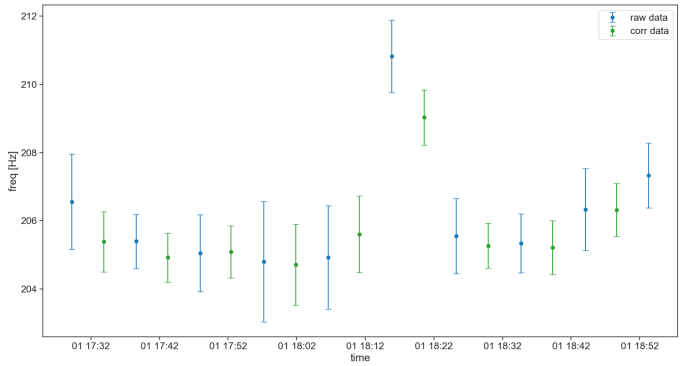

FIGURE 7.15: ABA results for probe 6. The blue markers are for raw data and the green markers are for the correction data.

Therefore, the field drift affects the data measurements during the rapid swapping run and the correction improves the data quality by using the ABA method.

7.2.2.3 ΔB Measurement Analysis

ΔB measurement determines the misalignment between the trolley and the plunging probe. I first measure ΔB for both of the trolley and plunging probe. Then, I extract the imposed gradient from ΔB measurements. The misalignment can be expressed as:

$$Mis = \frac{\Delta B_{\text{tr}} - \Delta B_{\text{pp}}}{dB_{\text{imp}}/dq} \tag{7.7}$$

where ΔB_{tr} and ΔB_{pp} represents ΔB measurements for the trolley and plunging probe, dB_{imp}/dq is the imposed gradient for q in x, y, and z directions in a local regime where the higher orders gradients and the cross terms are small. The detailed explanation is in Section 7.2.1.2.

Plunging Probe

The plunging probe measurement mechanism is explained in Section 7.2.2.2. It takes 6 measurements for each SCC status and I take the mean and standard deviation of these 6 measurements. Since the measurements take about 30 minutes, the

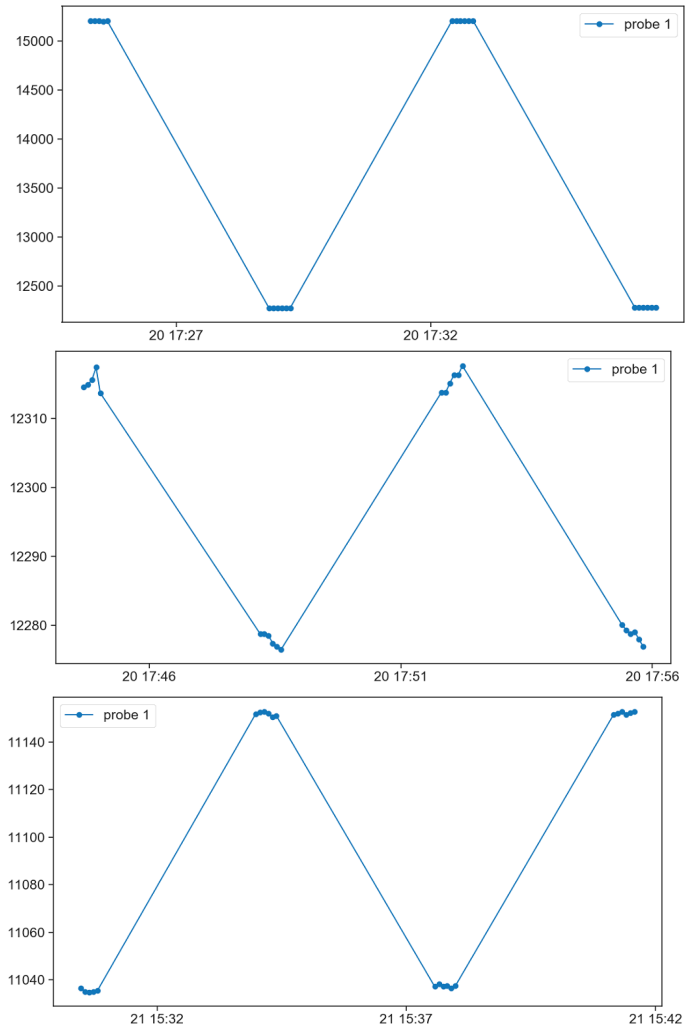

FIGURE 7.16: Plunging probe ΔB measurement plot for probe 1 - x, y, and z direction in order from top to bottom. X-axis is times and y-axis is frequencies in units of Hz

field drift perturbs the data taking so the ABA method (see Section 7.2.2.2) is used to correct the field drift. Fig 7.16 shows how the plunging probe data looks in the x, y, and z directions for probe 1.

Trolley Probe

The trolley probe measurement is explained in Section 7.2.2.2. The trolley probe is taking data continuously, so data selection is required when SCC is ON or OFF.

Probe	ΔB_x	$\delta\Delta B_x$	ΔB_y	$\delta\Delta B_y$	ΔB_z	$\delta\Delta B_z$
1	5.14	1.50	-11.68	1.49	-2.27	0.80
2	-3.82	1.05	2.99	1.32	1.95	0.81
3	5.04	1.71	-8.88	1.55	1.06	0.99
4	-19.24	1.22	-14.22	1.28	-1.86	1.94
5	-15.92	1.36	14.89	1.60	-1.34	1.50
6	-8.47	3.72	12.45	2.55	-0.60	1.91
7	7.47	2.71	8.96	1.91	2.03	2.63
8	8.69	1.69	14.43	1.69	1.94	1.46
9	-9.78	1.08	-0.53	1.19	5.15	1.61
10	6.76	2.68	-14.84	1.34	-3.17	1.55
11	15.37	3.19	-7.83	1.69	7.24	2.49
12	-19.35	2.13	-18.85	2.11	8.41	2.57
13	-18.85	2.05	27.53	2.81	0.50	1.75
14	-23.49	2.59	-0.20	1.33	4.05	1.39
15	-8.14	2.54	17.72	1.71	4.17	2.03
16	-10.49	1.38	-14.44	1.93	-3.69	1.78
17	-13.51	2.94	3.95	2.11	4.07	1.96

Table 7.5: Differences of ΔB measurement between trolley and plunging probe for each direction and each probe in unit of Hz

For the x and y directions, there are 4 toggling, so a total of 8 selections of trolley data are selected. I use the RMS method to select the data as the same technique I use for extracting data on the rapid swap analysis. Then, I use the ABA method (see Section 7.2.2.2) to correct linear drift. I use two ABA methods for the x and y directions and average them to get the final result. For the z direction, there are only 2 toggling, so 4 selections of trolley data are selected. I use one ABA method to correct the field drift. Fig 7.17 shows how the trolley probe data looks in the x, y, and z directions and red markers represent the data selections. Table 7.5 shows the difference of ΔB measurements between the trolley and plunging probes.

Imposed Gradient

Once the ΔB measurement is done, the imposed gradient can be determined. There are two separate parts to evaluate the imposed gradient: the transverse direction (x

and y directions) and the azimuthal direction (z-direction). The imposed gradients of the transverse direction can be evaluated from the ΔB measurements of the trolley probes and the imposed gradient of the azimuthal direction can be evaluated from the stepper run (Run 11334 for Run 3 calibration campaign) with SCC ON and OFF in the calibration region. For the transverse direction, I can map the gradient in a 2D contour plot with 17 trolley probes ΔB measurements. The 2D contour plots of the imposed gradient in the x and y direction are shown in Fig 7.18. To extract the gradient, the 2D 3^{rd} order polynomial is used around the beam center:

$$f(x,y) = p_0 + p_1 x + p_2 y + p_3 x^2 + p4y^2 + p_5 xy + p_6 x^3 + p_7 y^3 + p_8 x^2 y + p_9 xy^2. \quad (7.8)$$

The derivatives of the fitting function with respect to x and y of each trolley probe location give the imposed gradient in the x and y directions.

For the azimuthal direction (z-direction), one stepper run scans the field in six different positions from 189.00 to 189.20 degrees with SCC ON and OFF. The stepper run is shown in Fig 7.19. The region between each of the two red dashed lines represents the measurements of six different positions. I use the RMS method to select the data and the ABA method to correct the field drift of two toggle measurements (SCC ON and OFF) for each region or each position. Then, I fit the linear function to these 6 measurements as a function of positions. The slope of the linear function represents the imposed gradient in the azimuthal (z) direction. Fig 7.20 shows six measurements as a function of the trolley positions and linear fit of the function. Table 7.6 shows the results of imposed gradients in all directions. I find dB_{imp}/dx is between 44 Hz/mm to -47 Hz /mm, dB_{imp}/dy is between 32 Hz/mm and -44 Hz/mm, and dB_{imp}/dz is between 8 Hz/mm and -12 Hz/mm, each with uncertainties at the 0.1 Hz/mm level.

Probe	dB_x/dx	$\delta dB_x/dx$	dB_y/dy	$\delta dB_y/dy$	dB_z/dz	$\delta dB_z/dz$
1	-45.2598	0.0004	-38.4125	0.0010	-8.1413	0.1572
2	-45.5722	0.0005	-39.4095	0.0018	-8.9784	0.1590
3	-45.2458	0.0007	-37.5200	0.0013	-8.1134	0.1568
4	-45.5267	0.0005	-39.5844	0.0018	-8.8221	0.1659
5	-45.0450	0.0007	-36.7750	0.0013	-8.1395	0.1537
6	-46.4641	0.0009	-42.5754	0.0052	-12.0092	0.1646
7	-45.4818	0.0012	-41.1548	0.0045	-10.8477	0.1648
8	-44.7305	0.0017	-36.7926	0.0031	-8.9360	0.1594
9	-45.0029	0.0019	-34.0975	0.0026	-8.0787	0.1561
10	-46.0298	0.0017	-35.9017	0.0031	-8.7614	0.1622
11	-46.7478	0.0012	-40.3919	0.0045	-10.5233	0.2355
12	-46.3730	0.0009	-42.9252	0.0052	-11.5807	0.1815
13	-45.2023	0.0012	-40.7128	0.0045	-10.6285	0.1715
14	-44.3373	0.0017	-35.6772	0.0031	-8.8468	0.1561
15	-44.6015	0.0019	-32.6076	0.0026	-8.0874	0.1528
16	-45.7277	0.0017	-34.4364	0.0031	-8.9446	0.1578
17	-46.6259	0.0012	-39.3440	0.0045	-10.8949	0.2127

Table 7.6: Imposed Gradient Result in unit of Hz/mm

7.2.2.4 Shim Gradient Analysis

Before rapid swapping is executed, the field in the calibration region must be shimmed to be highly uniform. To shim the local gradients, cross scan and cube scan (see Section 7.2.1.3) are performed. The cross scan only measures x, y, and z directions so there is no information about cross-axis terms. On the other hand, the cube scan measures a combination of the x, y, and z axis, which takes more than 30 points per calibration campaign, so I am able to get richer information and measurements for the cross-axis terms. Therefore, first, the cross scan is run for shimming local gradients. Then, the cube scan is run for obtaining detailed gradient information about the local field in the calibration region [85].

Cross Scan

The cross scan takes a nine-point scan to use to map the gradient (see Fig.7.3): 3 points measured in each direction. The second-order polynomial function is used to

Probe	dB_s/dx	dB_s/dy	dB_s/dz	d^2B_s/dx^2	d^2B_s/dy^2	d^2B_s/dz^2
1	-0.12	-0.08	-0.55	-0.16	0.11	0.07
2	-0.46	0.78	-0.58	-0.30	0.25	-0.01
3	-0.29	-0.17	-0.64	-0.22	0.17	0.03
4	-0.15	-0.85	-0.52	-0.11	-0.06	0.04
5	-0.06	0.18	-0.53	-0.10	-0.07	0.00
6	1.03	-0.16	0.17	-0.75	0.92	0.15
7	0.59	-1.12	0.19	0.57	-0.70	-0.13
8	-0.09	0.57	-0.62	0.53	-0.19	-0.05
9	-0.21	0.25	-0.66	-0.60	0.52	0.05
10	0.43	-0.15	0.43	-0.20	0.31	0.12
11	0.31	0.03	1.70	-0.53	0.96	0.22
12	-0.10	-0.70	0.64	-0.25	0.31	0.31
13	0.02	-0.49	0.09	0.60	-0.88	0.04
14	0.27	0.15	-0.39	0.51	-0.58	-0.03
15	0.05	0.53	-0.34	-0.19	0.11	0.42
16	0.52	0.57	-0.20	-0.14	-0.07	0.01
17	-0.02	0.46	-0.05	-1.33	1.37	0.11

Table 7.7: Run 3 cross scan result

fit the 3-point measurements per each (x, y, z) around the probe position at (x_0, y_0, z_0):

$$\begin{aligned} B(x) &= p_0 + p_1(x - x_0) + p_2(x - x_0)^2, \\ B(y) &= p_0 + p_1(y - y_0) + p_2(y - y_0)^2, \\ B(z) &= p_0 + p_1(z - z_0) + p_2(z - z_0)^2. \end{aligned} \tag{7.9}$$

The cross scan measurements and fit functions for each direction of probe 1 are shown in Fig 7.21. The cross scan data is used for the active volume correction. The active volume correction will be discussed in a later section. The cross scan result is shown in Table 7.7.

Cube Scan

During Run 1 and Run 2 calibration campaigns, the cross scan is only performed to shim the local gradient. However, during the cross scan, cross-axis terms do not collect since it scans only one axis (either x, y, or z). To improve the systematic

source, the cube scan is used during Run 3 and beyond the calibration campaign. There are more than 30 scans during the cube scan and each scan detail is shown in Table 7.2. After obtaining measurements from the cube scan, oscillation correction is needed. The explanation of why oscillation correction is needed for the measurements is in section 7.2.2.2. The effect of the oscillation correction for probe 1 is shown in Fig. 7.22. After applying oscillation correction (orange markers on the plot), the error of each scan reduces significantly.

Due to 30 and more scans, the cube scan takes about one hour to one and half hours to complete. Unlike the cross scan, which is relatively short-running-time, field drift cannot be ignored in the cube scan. To correct the field drift, during the cube scan, the plunging probe takes several data measurements at the same position at different times. The several data measurements on the top of a linear fit function are shown in Fig 7.23. Using the slope of the linear fit, the field correction is applied to each scan measurement on the top of the oscillation correction.

After both oscillation and field drift corrections, instead of using all three directions, I pick 3 planes (xy, yz, and zx) and use the 2D second-order polynomial to fit the plane to evaluate the shim gradients.

$$f(q_1, q_2) = a_1 q_1^2 + a_2 q_2^2 + a_3 q_1 q_2 + a_4 q_1 + a_5 q_2 + a_6, \tag{7.10}$$

where q_1 and q_2 are (x,y), (y,z), or (z,x). The shim gradients are derivative of the equation 7.10:

$$\begin{aligned} \frac{\partial f(q_1, q_2)}{\partial q_1} &= 2a_1 q_1 + a_3 q_2 + a_4 \\ \frac{\partial f(q_1, q_2)}{\partial q_2} &= 2a_2 q_2 + a_4 q_1 + a_5 \end{aligned} \tag{7.11}$$

Each plane has two shim gradients for each q_1 and q_2. Therefore, I can get 2 gradients per axis, and I use the average of two gradients to finalize the shim gradient of each x,

y, and z direction. I propagate two uncertainties to determine the final uncertainty for each x, y, and z direction. The difference between these two results and the difference between cross scan and cube scan is described in the next section. Here are the tables showing two results from two planes for each direction x,y, and z from the cube scan (Table 7.8, 7.9, and 7.10). Since the cube scan is first introduced and implemented in the Run 3 calibration campaign, some of the cube scan results are not as clean as they should be. Also, each cube scan measured different numbers of measurements and positions for each probe. However, beyond pre Run 4 calibrations, the cube scan perform much better and cleaner with uniform numbers of measurements and positions per probe. In Table 7.8, 7.9, and 7.10, **-** means that the measurement is not able to extract from the cube scan. If only one of two measurements in each probe was marked as **-**, I only use the other one as the final result instead of averaging the two results. If both of the measurements in each probe are marked as **-**, I use the cross-scan measurement for that probe. The final result is shown in Table 7.11, which contains not only the shimmed gradient, but also the second-order shimmed gradient in x, y, and z directions.

	dB_x/dx		$\delta dB_x/dx$		d^2B_x/dx^2		$\delta d^2B_x/dx^2$	
Probe	XY	XZ	XY	XZ	XY	XZ	XY	XZ
1	-0.08	-0.16	-	0.04	-0.11	-0.12	-	0.03
2	-0.57	-0.62	-	0.04	-0.28	-0.29	-	0.02
3	-0.18	-0.31	-	0.05	-0.08	-0.16	-	0.03
4	-0.18	-0.11	-	0.08	-0.20	-0.18	-	0.05
5	-0.09	0.00	-	0.13	-0.20	-0.11	-	0.08
6	-0.34	0.38	0.40	0.20	-0.74	-0.78	0.24	0.13
7	0.66	0.69	0.62	0.42	0.99	0.88	0.29	0.20
8	-0.20	-0.02	0.24	0.08	0.29	0.57	0.11	0.05
9	0.17	-0.21	0.18	0.19	-0.49	-0.61	0.11	0.11
10	0.35	0.28	0.20	0.12	-0.29	-0.25	0.09	0.07
11	0.44	0.48	0.18	0.17	-0.41	-0.49	0.08	0.08
12	0.13	-0.47	0.14	0.16	-0.22	-0.26	0.09	0.10
13	0.47	0.37	0.29	0.12	0.76	0.74	0.13	0.07
14	0.16	0.28	0.17	0.05	0.45	0.62	0.08	0.03
15	0.01	0.35	0.13	0.17	-0.06	-0.07	0.08	0.10
16	0.38	-	0.09	-	-0.10	-	0.04	-
17	-0.32	-0.35	0.38	0.30	-1.21	-1.21	0.18	0.14

Table 7.8: Two x-direction measurements from two planes XY and XZ during cube scan.

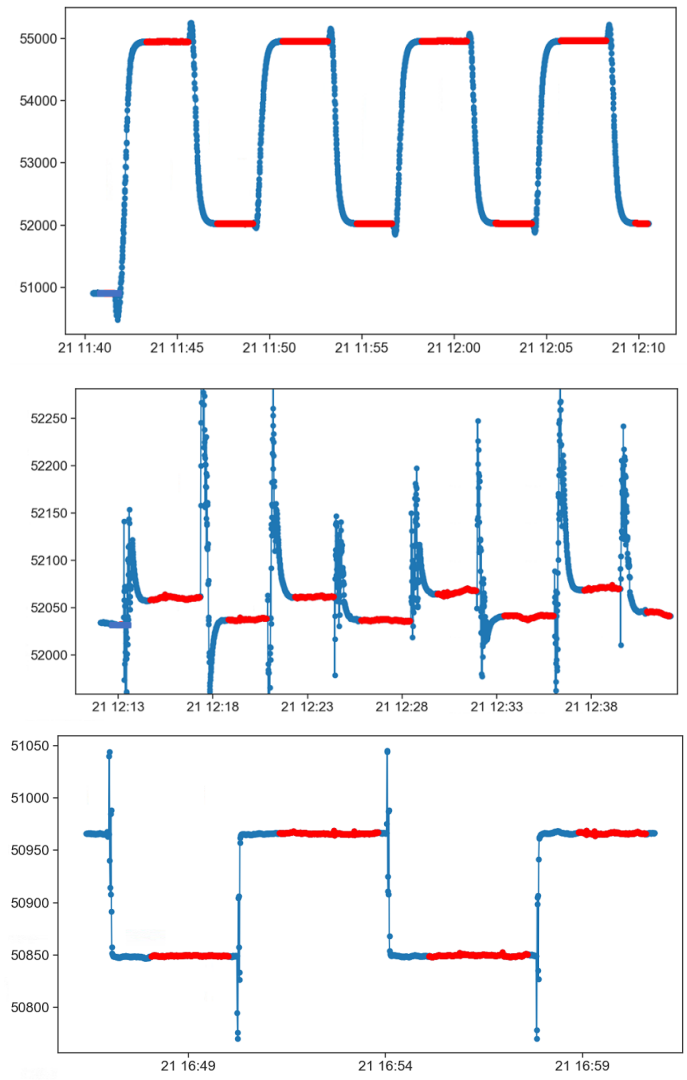

FIGURE 7.17: Trolley probe ΔB measurement plot for probe 1 - x, y, and z direction in order from top to bottom. Red markers represent the data selections. X-axis is times and y-axis is frequencies in units of Hz

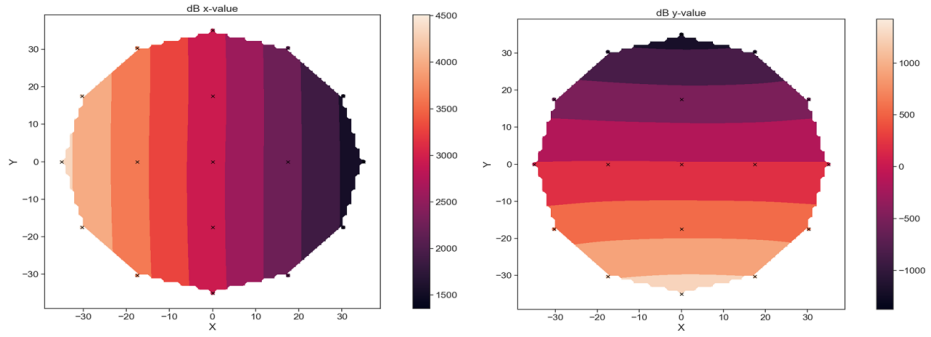

FIGURE 7.18: The 2D contour plots of imposed gradient in transverse direction. Left: x-direction, Right: y-direction

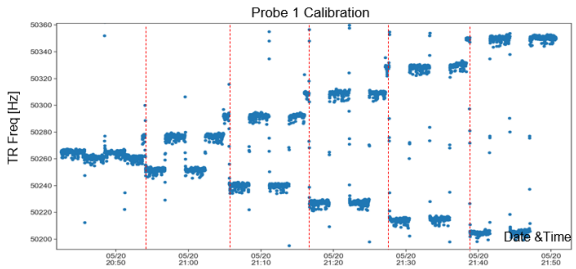

FIGURE 7.19: The stepper run with SCC ON and OFF for probe 1. The region between two red dash-lines represents the measurements of different positions of the trolley

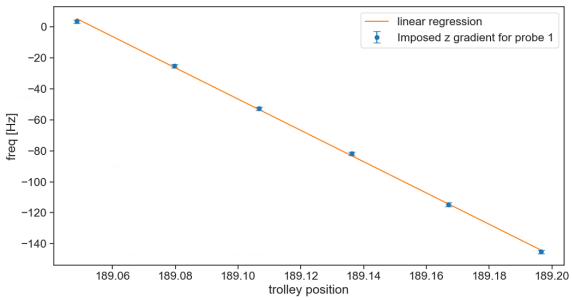

FIGURE 7.20: ΔB of the stepper run as function of trolley positions from Fig.7.19. Blue markers represent the mean and error for each position and the orange line represents the linear fit. The slope (or gradient) of this linear fit is the imposed z gradient.

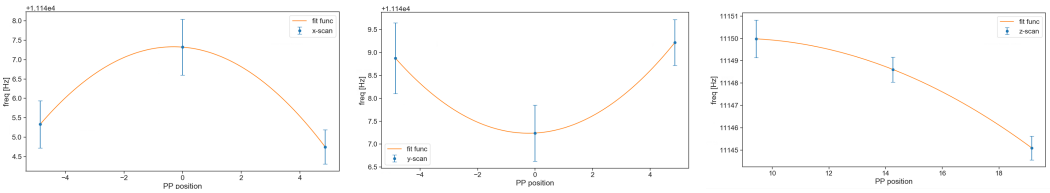

FIGURE 7.21: The cross scan measurements with a fit curve of probe 1 in each direction in order of x, y, and z directions

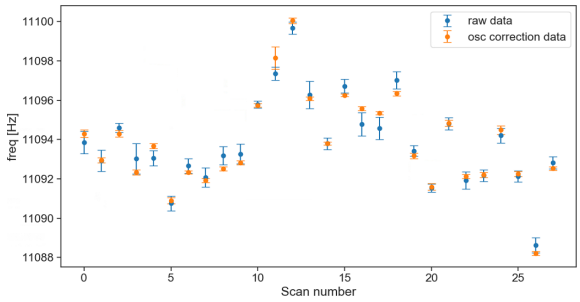

FIGURE 7.22: Cube scan measurement plot for probe 1. Blue markers represent the mean and error of 6 measurements per each scan and orange markers represent the mean and error of 6 measurements with the oscillation correction per each scan.

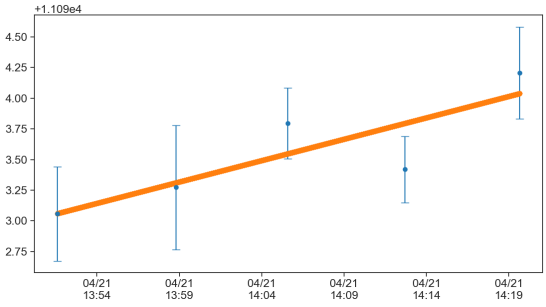

FIGURE 7.23: Field drift measurements plot for probe 1 during the cube scan. Blue markers represent the mean and error of 6 measurements per center point and the orange line represents the linear fit of the center measurements.

	dB_y/dy		$\delta dB_y/dy$		d^2B_y/dy^2		$\delta d^2B_y/dy^2$	
Probe	XY	YZ	XY	YZ	XY	YZ	XY	YZ
1	0.04	-0.01	-	0.05	0.15	0.18	-	0.04
2	0.85	0.79	-	0.04	0.28	0.34	-	0.02
3	-0.20	-0.14	-	0.07	0.24	0.14	-	0.04
4	-0.83	-0.98	-	0.06	0.09	0.04	-	0.04
5	0.30	0.30	-	-	0.07	0.03	-	-
6	0.26	0.32	0.38	0.17	0.93	0.90	0.24	0.10
7	-1.24	-1.08	0.27	0.09	-0.50	-0.74	0.13	0.06
8	1.90	1.82	0.50	0.08	-1.11	-0.72	0.23	0.05
9	-0.12	-0.07	0.17	0.82	0.05	0.23	0.11	0.45
10	-0.28	-0.20	0.41	-	0.05	0.33	0.19	-
11	-0.53	-0.53	0.09	0.07	0.46	0.39	0.04	0.03
12	-1.14	-0.73	0.14	0.19	0.18	0.21	0.09	0.11
13	-0.64	-0.63	0.14	0.12	-1.00	-1.14	0.06	0.05
14	0.38	-	1.18	-	-0.70	-	0.49	-
15	0.77	0.72	0.12	0.31	0.42	0.34	0.07	0.15
16	0.45	-	0.19	-	-0.11	-	0.09	-
17	0.31	0.31	0.19	0.18	1.58	1.61	0.08	0.08

Table 7.9: Two y-direction measurements from two planes XY and YZ during cube scan.

	dB_z/dz		$\delta dB_z/dz$		d^2B_z/dz^2		$\delta d^2B_z/dz^2$	
Probe	YZ	XZ	YZ	XZ	YZ	XZ	YZ	XZ
1	-0.57	-0.54	0.05	0.04	0.09	0.06	0.03	0.03
2	-0.70	-0.61	0.03	0.04	0.05	-0.03	0.02	0.02
3	-0.74	-0.59	0.07	0.05	0.01	0.05	0.04	0.03
4	-0.80	-0.63	0.06	0.08	0.03	0.11	0.04	0.05
5	-	-0.93	-	0.12	-	-0.07	-	0.08
6	-0.21	0.11	0.14	0.20	0.04	-0.05	0.11	0.13
7	0.01	0.17	0.09	0.21	-0.08	0.10	0.06	0.09
8	-	-0.50	-	0.08	-	0.08	-	0.05
9	-	-0.43	-	0.18	-	0.27	-	0.11
10	-	0.46	-	0.11	-	0.02	-	0.07
11	0.33	0.28	0.06	0.07	0.17	0.22	0.03	0.03
12	0.34	0.78	0.18	0.15	0.29	0.28	0.11	0.10
13	-0.16	-0.09	0.10	0.05	-0.03	0.05	0.05	0.03
14	-0.19	-0.14	0.03	0.05	-0.03	0.04	0.00	0.03
15	-	-0.76	-	0.16	-	-0.29	-	0.10
16	-	-0.06	-	0.05	-	0.07	-	0.03
17	-0.36	-0.26	0.16	0.12	-0.05	-0.06	0.08	0.06

Table 7.10: Two z-direction measurements from two planes YZ and XZ during cube scan.

Probe	d^2B_s/dx^2	$\delta d^2B_s/dx^2$	dB_s/dx	$\delta dB_s/dx$	d^2B_s/dy^2	$\delta d^2B_s/dy^2$	dB_s/dy	$\delta dB_s/dy$	d^2B_s/dz^2	$\delta d^2B_s/dz^2$	dB_s/dz	$\delta dB_s/dz$
1	-0.11	0.03	-0.12	0.04	0.16	0.04	0.01	0.05	-0.07	0.02	0.56	0.03
2	-0.29	0.02	-0.59	0.04	0.31	0.02	0.82	0.04	-0.01	0.02	0.66	0.03
3	-0.12	0.03	-0.24	0.05	0.19	0.04	-0.17	0.07	-0.03	0.03	0.67	0.04
4	-0.19	0.05	-0.15	0.08	0.07	0.04	-0.91	0.06	-0.07	0.03	0.71	0.05
5	-0.15	0.08	-0.05	0.13	0.05	0.00	0.30	0.00	0.07	0.08	0.93	0.12
6	-0.76	0.14	0.02	0.23	0.92	0.13	0.29	0.21	0.00	0.08	0.05	0.12
7	0.93	0.18	0.68	0.38	-0.62	0.07	-1.16	0.14	-0.01	0.05	-0.09	0.11
8	0.43	0.06	-0.11	0.13	-0.92	0.12	1.86	0.25	-0.08	0.05	0.50	0.08
9	-0.55	0.08	-0.02	0.13	0.14	0.23	-0.10	0.42	-0.27	0.11	0.43	0.18
10	-0.27	0.06	0.31	0.12	0.19	0.19	-0.24	0.41	-0.27	0.07	-0.46	0.11
11	-0.45	0.06	0.46	0.12	0.42	0.03	-0.53	0.06	-0.19	0.02	-0.31	0.05
12	-0.24	0.07	-0.17	0.11	0.20	0.07	-0.94	0.12	-0.28	0.07	-0.56	0.12
13	0.75	0.07	0.42	0.16	-1.07	0.04	-0.63	0.09	-0.01	0.03	0.13	0.06
14	0.53	0.04	0.22	0.09	-0.70	0.49	0.38	0.00	0.00	0.03	0.16	0.03
15	-0.07	0.06	0.18	0.11	0.38	0.09	0.74	0.17	0.29	0.10	0.76	0.16
16	-0.13	0.03	0.46	0.05	-0.11	0.09	0.45	0.19	-0.07	0.03	0.06	0.05
17	-0.67	0.11	-0.33	0.24	0.68	0.06	0.31	0.13	0.05	0.05	0.31	0.10

Table 7.11: Shimmed Gradient Result in unit of Hz/mm.

Probe	dB_s/dx	dB_s/dy	dB_s/dz	d^2B_s/dx^2	d^2B_s/dy^2	d^2B_s/dz^2
1	0.00	0.09	-0.01	0.04	0.05	0.00
2	-0.14	0.04	-0.08	0.02	0.06	0.02
3	0.05	0.00	-0.02	0.10	0.02	0.00
4	0.00	-0.06	-0.19	-0.09	0.13	0.03
5	0.01	0.12	-0.40	-0.05	0.12	-0.07
6	-1.01	0.45	-0.22	-0.01	-0.01	-0.15
7	0.09	-0.04	-0.10	0.36	0.08	0.14
8	-0.02	1.29	0.12	-0.10	-0.73	0.13
9	0.19	-0.35	0.23	0.05	-0.38	0.22
10	-0.12	-0.09	0.03	-0.07	-0.13	-0.10
11	0.15	-0.56	-1.39	0.08	-0.54	-0.03
12	-0.07	-0.24	-0.08	0.01	-0.12	-0.02
13	0.40	-0.15	-0.22	0.15	-0.19	-0.03
14	-0.05	0.22	0.23	0.02	-0.13	0.03
15	0.13	0.21	-0.43	0.13	0.27	-0.71
16	-0.15	-0.12	0.14	0.03	-0.04	0.06
17	-0.31	-0.15	-0.26	0.12	0.23	-0.16
MEAN	-0.05	0.04	-0.16	0.05	-0.08	-0.04
MIN	0.40	1.29	0.23	0.36	0.27	0.22
MAX	-1.01	-0.56	-1.39	-0.10	-0.73	-0.71

Table 7.12: (Run 3) Differences of the first and second orders of shimmed gradients in Hz between cross scan and cube scan in x, y, and z directions. The last three rows represent the mean of the differences, the maximum of the differences, and the minimum of the differences.

Cross Scan vs Cube Scan

The differences between cross scan and cube scan in units of Hz are shown in Table 7.12. The differences in the first-order gradient were 11 $\pm$ 16 ppb and the differences in the second-order gradient were -11 $\pm$ 11 ppb. It confirmed that the differences between the cross scan and cube scan were within their uncertainties.

7.2.2.5 Misalignment Analysis

In this section, combining all the analyses together, I discuss how to evaluate the misalignment between the plunging and trolley probe from the ΔB measurements, the imposed and shimmed field gradients, and the trolley barcode correction and how to account for it in the calibration constant.

ΔB Measurement

Here is the expression to calculate misalignment correction from ΔB measurements:

$$\begin{aligned} B_{\text{mis},i} &= \sum \left.\frac{dB_s}{dq}\right|_{q=0} \cdot \frac{\Delta B(\text{TR - PP})}{dB_{\text{imp}}/dq} \\ &= \sum S_q \cdot M_q, \end{aligned} \tag{7.12}$$

where S_q is the shim gradient, M_q misalignment, i is a selected probe and q is either x, y, or z directions.

The uncertainty of the misalignment is expressed as:

$$\delta B^2_{\text{mis},i} = ((\delta S_q) \cdot M_q)^2 + (S_q \cdot (\delta M_q))^2, \tag{7.13}$$

where δS_q is the uncertainty of the shim gradient which can be found in Table 7.11 and δM_q is the uncertainty of the misalignment. δM_q is in unit of mm and is evaluated by:

$$(\delta M_q)^2 = (\frac{\delta[\Delta B(\text{TR - PP})]}{dB_{\text{imp}}/dq})^2 + (\frac{\Delta B(\text{TR - PP}) \cdot \delta[dB_{\text{imp}}/dq]}{(dB_{\text{imp}}/dq)^2})^2, \tag{7.14}$$

where those uncertainties are found in Table 7.5 and 7.6.

Barcode Correction

During the calibration campaign, the ΔB measurement is only performed once. However, during rapid swapping, the trolley moves in and out 10 times which causes the additional possible misalignment between the target position and the real position. The encoder position is not as accurate as the barcode data. However, the barcode data cannot be directly used. The detailed explanation is in Section 7.2.2.2. After finding the local offset from the first swap data (reference data), the shimmed gradient is used to calculate the offset in a unit of Hz:

$$B_{\text{barcode corr}} = S_q \cdot mis_{\text{barcode}}, \tag{7.15}$$

where S_q is defined in equation 7.13 and $mis_{barcode}$ is the local offset from the first swap data. The result is in Table 7.4. The average offset is -0.168 Hz. The uncertainty of the barcode correction is about 0.08 Hz.

Misalignment Correction Result

Table 7.13 shows the misalignment correction results for each probe from the Run 3 calibration campaign.

Probe	$B_{mis,x}$	$\delta B_{mis,x}$	$B_{mis,y}$	$\delta B_{mis,y}$	$B_{mis,z}$	$\delta B_{mis,z}$	$B_{mis,total}$	$\delta B_{mis,total}$	$B_{mis,barcode}$	$\delta B_{mis,barcode}$
1	0.0113	0.0033	0.0075	0.0010	0.1485	0.0526	0.1673	0.0527	0.0000	0.0119
2	-0.0446	0.0122	-0.0623	0.0275	-0.1466	0.0612	-0.2535	0.0681	-0.1316	0.0078
3	0.0266	0.0090	-0.0249	0.0043	-0.0880	0.0822	-0.0863	0.0827	-0.0547	0.0127
4	-0.0679	0.0043	-0.3235	0.0291	0.1570	0.1636	-0.2344	0.1662	0.0057	0.0137
5	-0.0120	0.0010	-0.1435	0.0155	0.1240	0.1391	-0.0314	0.1399	-0.0075	0.0263
6	-0.0005	0.0003	-0.0725	0.0148	0.0037	0.0119	-0.0693	0.0190	-0.0592	0.5086
7	0.0021	0.0008	0.2932	0.0626	0.0306	0.0397	0.3259	0.07412	-0.0172	0.2494
8	0.0473	0.0092	-0.5741	0.0674	-0.1217	0.0916	-0.6485	0.1141	-0.0491	0.0313
9	0.0034	0.0004	-0.0042	0.0095	-0.4065	0.1274	-0.4072	0.1277	-0.0026	0.0856
10	-0.0412	0.0164	0.0202	0.0018	-0.1194	0.0584	-0.1405	0.0606	-0.1831	0.0482
11	-0.2008	0.0417	-0.1276	0.0275	0.2053	0.0708	-0.1232	0.0866	-0.0115	0.0307
12	-0.0585	0.0064	-0.3980	0.0445	0.4137	0.1266	-0.0428	0.1343	0.3292	0.0415
13	0.2844	0.0309	0.3326	0.0340	-0.0070	0.0246	0.6100	0.0521	0.0103	0.0917
14	0.1703	0.0188	0.0092	0.0602	-0.0808	0.0277	0.0987	0.0688	0.0030	0.0366
15	0.0294	0.0092	-0.3914	0.0378	-0.2553	0.1242	-0.6173	0.1301	-0.0030	0.0417
16	0.0948	0.0125	0.1196	0.0160	0.0114	0.0055	0.2258	0.0209	0.0088	0.1715
17	-0.2125	0.0462	-0.0402	0.0215	-0.1582	0.0764	-0.4109	0.0918	-0.0040	0.0663

Table 7.13: Misalignment correction results of Run 3 calibration campaign in unit of Hz

7.2.2.6 Shielded Proton and Temperature Correction

From the note [86], the standard (reference) temperature is chosen to be $T = 34.7°C$. Because frequency measurements depend on the temperature, the final correction is needed from the temperature difference between the actual and standard temperature.

Plunging Probe Correction

The shielded proton frequency is the measured frequency with a pure sphere water sample. Since the plunging probe is a cylinder shape probe with a pure water sample, the shield proton and temperature correction are needed for the plunging probe. The H_2O calibration probe frequency $\omega_p(T)$ to the free proton frequency at the standard temperature is expressed as:

$$\frac{\omega_p(T)}{\omega_p(34.7°C)} = 1 + \frac{1}{\omega_p(T)}\frac{d\omega_p(T)}{dT}\Delta T, \tag{7.16}$$

where $\frac{1}{\omega_p(T)}\frac{d\omega_p(T)}{dT} = -10.36(0.30) \times 10^{-9}$ and $\Delta T = T - 34.7°C$. From this relationship, the frequency of the plunging probe decreases as temperature increases. Temperature sensors connected to plunging probe measures in units of Ω. Therefore, the conversion from Ω to Celsius is needed. Fig 7.24 shows the average temperatures and uncertainties of the rapid swap of each probe. The error of each swap is the readout uncertainty, and it does not include $0.5°C$ uncertainty that is in common with all measurements because of the sensor accuracy. The most difference is about $2°C$ and the temperatures throughout rapid swapping remain stable since the standard deviation is about $0.2°C$.

The plunging probe uncertainty in ppb can be expressed as,

$$(\frac{\delta\omega(34.7)}{\omega})^2 = \delta(\frac{d\omega'}{dT})^2\Delta T^2 + (\frac{d\omega'}{dT})^2\delta(\Delta T)^2, \tag{7.17}$$

Probe	trolley						pluning probe			
	run-2		run-3		mean		run-2		run-3	
	mean	std	mean	std	mean	std	mean	std	mean	std
1	34.7	0.1	33.6	0.0	34.2	0.0	25.18	0.00	22.72	0.00
2	32.8	0.1	33.7	0.0	33.3	0.1	24.99	0.00	22.51	0.00
3	27.7	0.1	31.5	0.2	29.6	0.1	24.67	0.00	22.66	0.00
4	29.6	0.3	32.9	0.1	31.2	0.2	24.73	0.00	23.16	0.00
5	27.7	0.3	33.8	0.0	30.7	0.2	24.56	0.00	23.20	0.00
6	32.7	0.2	34.4	0.0	33.5	0.1	25.63	0.00	23.77	0.00
7	30.7	0.4	34.3	0.0	32.5	0.3	26.18	0.00	23.77	0.00
8	33.2	0.2	34.7	0.0	33.9	0.1	26.71	0.00	23.89	0.00
9	31.4	0.2	35.0	0.0	33.2	0.2	25.22	0.00	23.96	0.00
10	35.0	0.3	34.8	0.0	34.9	0.2	28.53	0.00	23.94	0.00
11	37.4	0.1	34.6	0.0	36.0	0.1	28.91	0.00	24.01	0.00
12	32.3	0.1	34.8	0.0	33.5	0.1	25.28	0.00	24.10	0.00
13	34.4	0.2	34.9	0.0	34.6	0.1	28.01	0.00	24.03	0.00
14	36.8	0.1	35.4	0.0	36.1	0.1	28.48	0.00	24.25	0.00
15	28.7	0.3	29.7	0.1	29.2	0.2	24.68	0.00	23.83	0.00
16	37.6	0.1	29.1	0.2	33.4	0.2	28.71	0.00	23.84	0.00
17	33.5	0.2	33.0	0.2	33.3	0.2	27.71	0.00	24.35	0.00
tot	32.7	3.0	33.5	1.8	33.1		26.36	0.01	23.64	0.01

Table 7.14: Plunging probe and trolley's temperatures during rapid swapping in Run 2 and Run 3 calibration campaigns. Units of C.

where $d\omega'/dT = \frac{1}{\omega_p(T)}\frac{d\omega_p(T)}{dT} = -10.36(0.30)$ ppb. Table 7.14 shows the plunging probe and trolley temperatures during rapid swapping in Run 2 and Run 3 calibration campaigns. From Table 7.14, the statistical uncertainty of the plunging probe is 0.00 °C. However, the systematic uncertainty of the plunging probe is 0.5 °C. The result is shown in 7.15.

The shielded proton frequency from the plunging probe is expressed as:

$$\tilde{\omega}_p'^{\text{shielded}} = \omega_p^{\text{measure}}/[1 - \delta_b(H_2O, T) - \delta_t], \tag{7.18}$$

where $\sigma(H_2O, T)$ is the isotropic chemical shift (dimagnetic shielding), which is -25.790(14) $\times 10^{-6}$, $\delta_b(H_20, T)$ is the bulk magnetic susceptibility of the water at T, and δ_t is the summation of the perturbations to the field due to the probe correction

Probe	Stat Unc (PPB)	Syst Unc(PPB)
1	3.6	6.3
2	3.7	6.3
3	3.6	6.3
4	3.5	6.2
5	3.5	6.2
6	3.3	6.1
7	3.3	6.1
8	3.2	6.1
9	3.2	6.1
10	3.2	6.1
11	3.2	6.1
12	3.2	6.1
13	3.2	6.1
14	3.1	6.1
15	3.3	6.1
16	3.3	6.1
17	3.1	6.0

Table 7.15: Plunging probe's temperature statistical and systematic uncertainties in ppb.

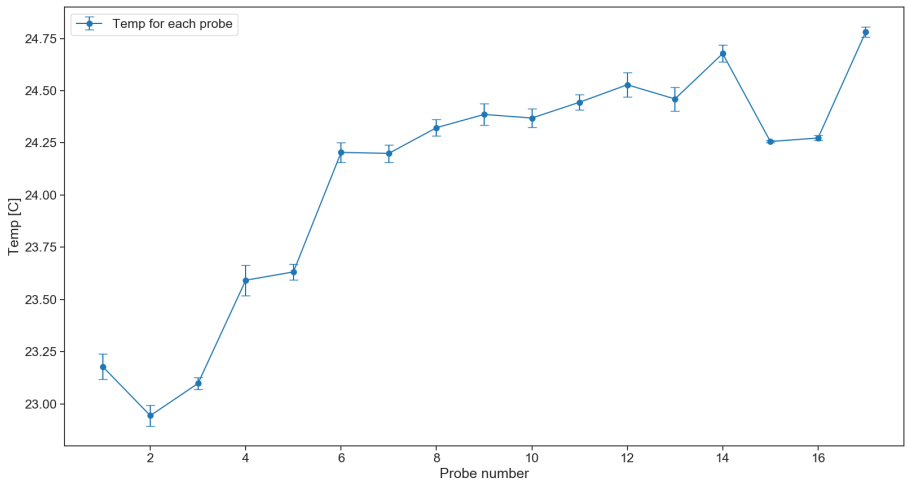

FIGURE 7.24: Plunging Probe's average temperatures and uncertainties during rapid swapping per probe.

[87][88]. The bulk susceptibility $\delta_b(H_2O, T)$ is evaluated,

$$\delta_b(H_2O, T) = \frac{1}{6}\chi(H_2O, T), \tag{7.19}$$

where $\chi(H_2O, T)$ is the susceptibility of water at temperature T. The susceptibility of water $\chi(H_2O, T)$ is described.

$$\chi(H_2O, T) = \chi(H_2O, 20^\circ C) \times [1 + a_1(T-20) + a_2(T-20)^2 + a_3(T-20)^3], \tag{7.20}$$

where $\chi(H_2O, 20^\circ C) = -9.05(3) \times 10^{-6}$, $a_1 = 1.38810 \times 10^{-4}$, $a_2 = -1.2685 \times 10^{-7}$, and $a_3 = 8.09 \times 10^{-10}$ [87][89]. Lastly, the perturbations δ_t is $-5.5 \times 10^{-9} \pm 12.9 ppb/^\circ C$. During rapid swapping, the equation 7.18 is applied to each plunging probe measurement.

Trolley Probe Correction

Unlike the plunging probe, the trolley probe contains a petroleum jelly sample, which has a different temperature dependence compared to water, and the temperature correction is the only one correction needed for the trolley measurements. The temperature correction is defined as [87],

$$f_{\text{corr}} = \frac{f_{\text{meas}}}{1 - \frac{d\delta_{\text{jelly}}}{dT}(T - 34.7)}, \tag{7.21}$$

where $d\delta_{\text{jelly}}/dT = 1.775 \times 10^{-9} \pm 0.225$ ppb$/^\circ C$. Fig 7.25 shows the average temperatures and uncertainties for the rapid swap of each probe. The pattern of the trolley temperature plot is similar to that of the plunging probe, but the difference is much larger than the plunging probe's difference, which is about $8^\circ C$.

Magnitude of Corrections

After evaluating all corrections for the plunging and trolley probes, corrections are applied to the rapid swap analysis (Section 7.2.2.2). As a result, calibration constants

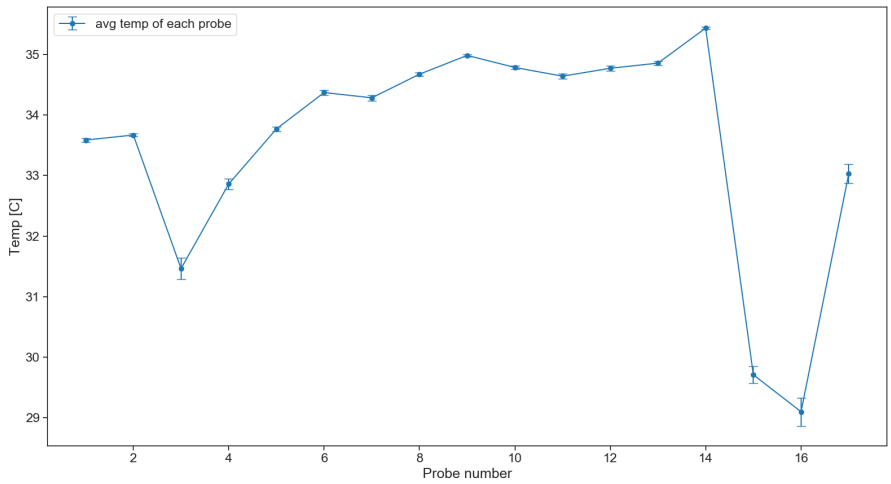

FIGURE 7.25: Trolley's average temperatures and uncertainties during rapid swapping per probe.

shift about -5.69 Hz when temperature corrections for both plunging and trolley probes are applied. In addition to the shielded proton correction for the plunging probe, the calibration constants shift about -98.7 Hz.

The uncertainty for temperature correction is evaluated as (unit of ppb):

$$\begin{aligned} \delta_{\text{dep}} &= \sqrt{(\Delta PP)^2 \times (0.30)^2 + (\Delta TR)^2 \times (0.255)^2} \\ \delta_{\text{temp}} &= \sqrt{(\delta PP)^2 \times (10.36)^2 + (\delta TR)^2 \times (1.775)^2}, \end{aligned} \tag{7.22}$$

where δ_{dep} indicates the temperature dependence uncertainty and δ_{temp} indicates the temperature uncertainty. ΔPP and ΔTR are the difference between measured and reference temperatures, $(34.7^{\circ}C)$ and 0.30 and 0.225 come from the equation 7.16 and 7.21. δPP and δTR are the uncertainty of measured temperatures. The detailed temperature correction can be found in the note [90]. As a result, temperature correction gives about 3.3 ppb for each probe. The uncertainty of shielded proton correction is the combination of the uncertainty in equation 7.18, which is about 13 ppb [89]. Therefore, the total uncertainty is about 13.3 ppb.

7.2.2.7 Systematic Uncertainty

There are a few systematic sources in the calibration analysis: FID extraction, misalignment, and temperature sensor. These systematic uncertainties shift and produce perturbation to the calibration coefficient, so they need to be studied.

FID Extraction

To measure the magnetic field, the FID frequency extraction is needed from the NMR signal. Run 1 analysis used the simulation to estimate the systematic uncertainty from the FID frequency extraction method. In the calibration campaigns, the local field is shimmed and well-known from the cross scan and cube scan. The difference in probe sensitivities from plunging and trolley probes can be evaluated by the simulation tool from the known gradients. The total FID-related systematic uncertainty, ϵ, is a sum of the fit uncertainty and intrinsic uncertainty [82]. Table 7.16 shows the fit and intrinsic uncertainties for the plunging and trolley probes during rapid swapping. The last column of Table 7.16 is the systematic uncertainty of FID extraction for the swapping run.

The calibration constant is redefined as

$$CC = \omega_{\text{truth}} - \omega_{\text{trolley}} - \epsilon_{\text{tr}} \tag{7.23}$$

During calibration campaign, plunging probe is used for ω_{truth}, so equation 7.23 is expressed as

$$\begin{aligned} CC &= \omega_{\text{pp}} + \epsilon_{\text{pp}} + \delta_{\text{static}} - \omega_{\text{tr}} - \epsilon_{\text{tr}} \\ &= \omega_{\text{pp}} - \omega_{\text{tr}} + \epsilon_{\text{pp-tr}} + \delta_{\text{static}} \end{aligned} \tag{7.24}$$

Therefore, $\epsilon_{\text{pp-tr}}$ directly contributes to the calibration constant. However, from Run 3 and beyond, I approached a new way to evaluate FID extraction uncertainties and will discuss them in the later section.

Probe	PP Fit	PP Intrinsic	TR Fit	TR Intrinsic	ϵ_{PP-TR}
1	-0.0154	2.3689	-0.0634	1.6837	0.7332
2	-0.0010	0.2471	-0.0051	0.1489	0.1023
3	-0.0130	1.8947	-0.0693	1.2827	0.6682
4	-0.0204	1.9983	-0.1002	1.6738	0.4043
5	0.0305	-2.9331	0.1429	-2.1610	-0.8845
6	0.0021	-1.0786	0.0016	-0.8752	-0.2029
7	-0.0004	0.4509	-0.0010	0.3583	0.0931
8	-0.0083	1.3271	-0.0423	1.0926	0.2686
9	-0.4737	9.4090	-0.9501	7.2948	2.5905
10	-0.0096	2.2564	-0.0282	1.6090	0.6661
11	-0.0773	5.3233	-0.1486	3.9577	1.4370
12	-0.2320	7.6126	-0.4968	5.6536	2.2238
13	0.0048	-2.2625	0.0063	-1.4440	-0.8200
14	-0.0061	2.2746	-0.0106	1.5487	0.7305
15	0.3062	-8.1866	0.5701	-6.2478	-2.2027
16	-0.0004	0.3587	-0.0008	0.3133	0.0457
17	0.0077	-1.2021	0.0306	-1.1727	-0.0523

Table 7.16: Fit and intrinsic uncertainties for trolley probes and the plunging probe during rapid swapping in a unit of Hz.

Active Volume Misalignment

The active volume of the plunging probe and the trolley are different due to the different probe geometries. Most notably, the active volume of the plunging probe has much longer tails than the active volume of the trolley, along the probe axis, due to the larger radius of the pickup coil. Fig 7.26 shows the sensitivity functions of the plunging probe and trolley probe. The extracted NMR frequency corresponds to the average frequency in the active volume. When the field is linear, the active volume difference would not affect the field measurements. However, in not completely homogeneous fields with a non-zero second-order derivative along the probe axis, the two NMR probe geometries probe slightly different contributions due to this difference in the active volume, even if they are perfectly aligned. Based on the local field scans, a corresponding correction of what the plunging probe would see if it would reassemble the trolley probe geometry is calculated. In run 1, this effect

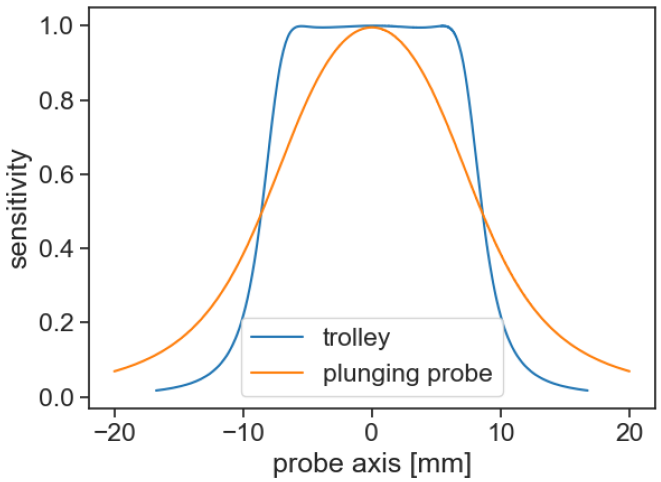

FIGURE 7.26: Active volume sensitivity functions for the trolley and plunging probes.

was not corrected but used as an uncertainty estimate. Local second-order gradients on the size of up to 5 ppb/mm^2 lead to corrections of up to 40 ppb.

To estimate the correction, a simulation tool is used with a shimmed gradient of each probe. First, the average frequencies of the plunging probe and trolley probe are estimated by the simulation tool and then I find the difference between the plunging probe and trolley's frequencies. Table 7.17 shows the average field evaluations and differences of the simulated evaluation between two probes. More detailed analysis will be described in the later chapter (Section 9.2).

Systematic Uncertainty from Misalignment Correction

The misalignment uncertainties come essentially from the gradients and the ΔB measurements. During the 3D stage in the calibration campaign, ± 5 counts are allowed which leads to position uncertainty (or repeatability uncertainty) from the limited position. ± 5 counts are converted to $0.1814mm$. The shimmed gradient fit function is expressed in Equation 7.10 and the shimmed gradient is the derivative of the fit function which is expressed in Equation 7.11. The position error is evaluated

	Active Volume Difference in Hz		
Probe	Trolley	Plunging Probe	Diff
1	10000.83	10001.12	-0.29
2	9999.93	9999.86	0.06
3	10000.37	10000.49	-0.12
4	10000.36	10000.54	-0.18
5	10000.04	9999.92	0.12
6	10001.90	10002.48	-0.57
7	9998.44	9997.84	0.59
8	9999.52	9999.34	0.17
9	10000.67	10000.78	-0.12
10	10001.41	10002.04	-0.64
11	10002.70	10003.94	-1.23
12	10003.71	10005.04	-1.33
13	10000.39	10000.48	-0.09
14	9999.57	9999.48	0.09
15	10005.08	10006.76	-1.68
16	10000.05	10000.01	0.05
17	10001.30	10001.82	-0.52

Table 7.17: Trolley and plunging probe's average frequencies over active volumes in a unit of Hz and misalignment uncertainties in all directions due to active volume in a unit of ppb.

from the error propagation of ± 5 counts and shimmed gradient at misalignment in the x, y, and z directions. Position error of the selected probe i in direction q can be found as,

$$\delta POS_{q,i} = 0.1814 \cdot \frac{1}{2}\sqrt{(\frac{\partial f(q,s)}{\partial q}\Big|_{q=q_0,s=s_0})^2 + (\frac{\partial f(q,t)}{\partial q}\Big|_{q=q_0,t=t_0})^2}, \tag{7.25}$$

where δPOS is a position uncertainty, q includes not only 3 main directions, x, y, or z but also cross terms, xy, yz, or zx. For cross-axis terms, the uncertainties are not available for all probes. For example, probe 1 in xy term is not able to extract the uncertainty because of the missing scans during the cube scan. For the missing cross-axis terms' uncertainties, the average values from other probes in the same cross-axis terms are used instead. The results are shown in Table 7.18.

The final misalignment uncertainties are the addition of two misalignment un-

Probe	Mis_x	Mis_y	Mis_z	Mis_{xy}	Mis_{yz}	Mis_{zx}
1	0.12	0.15	0.10	0.16	0.04	0.03
2	0.11	0.11	0.07	0.16	0.03	0.03
3	0.16	0.21	0.12	0.16	0.05	0.04
4	0.23	0.17	0.14	0.16	0.04	0.06
5	0.38	0.00	0.36	0.16	0.14	0.10
6	0.66	0.61	0.36	0.31	0.11	0.16
7	1.10	0.42	0.33	0.26	0.07	0.19
8	0.38	0.74	0.23	0.22	0.07	0.06
9	0.39	1.23	0.54	0.14	0.72	0.15
10	0.34	1.20	0.33	0.18	0.14	0.09
11	0.36	0.16	0.14	0.08	0.06	0.07
12	0.31	0.34	0.34	0.11	0.14	0.12
13	0.46	0.28	0.17	0.13	0.11	0.09
14	0.27	0.00	0.09	0.16	0.04	0.04
15	0.32	0.49	0.47	0.10	0.27	0.13
16	0.16	0.55	0.16	0.08	0.14	0.05
17	0.72	0.38	0.30	0.17	0.17	0.12

Table 7.18: Result of position uncertainty from misalignment in unit of PPB.

certainties: one from the misalignment equation shown in Table 7.13 and another one from the position uncertainty shown in Table 7.18. Since there are no cross-term misalignment corrections from Table 7.13, only x, y, and z direction uncertainties are needed to be propagated.

Footprint Correction

From Run 3 and beyond, during the rapid swapping procedure, the trolley is retracted 10° from 190° to 180° in order to keep enough distance from the plunging probe during its measurements. The chosen distance is initially estimated in order not to be perturbed by the trolley to the plunging probe during its measurements. However, there is trolley perturbation at 180° to the plunging probe measurements. The magnitude of the trolley perturbation is shown in Fig 7.27 from the note [88]. The plunging probe is positioned in the magnetic field at the nominal calibration location at 190° aligned to the trolley probe 1 position. The plunging probe takes a

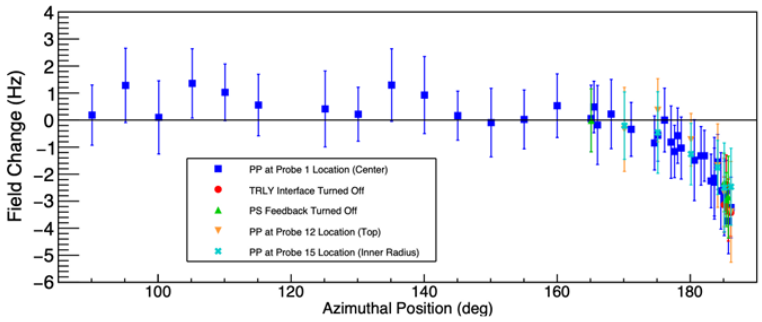

FIGURE 7.27: The magnitude of the trolley perturbation as seen by the plunging probe when the trolley is located at the azimuthal location indicated on the x-axis [88]

field measurement where the trolley is positioned at 185°. Then, the plunging probe takes another field measurement where the trolley is retracted to 85° in azimuth. The perturbation of the trolley, as seen by the plunging probe, is defined as the difference between the two field measurements. The general procedure is repeated for different trolley azimuthal locations: 33 different locations between 85° and 185°. Fig 7.27 includes the studies for various conditions such as turning off the trolley electronics, turning off power supply feedback, and positioning the plunging probe at different trolley probe locations.

In order to estimate the footprint correction at 180°, first, I need to find the right function to fit the plot. The fit function is $a + b/(x - x_0)^2$, where a and b are the constant coefficients and x_0 is the horizontal shift, in this case, the azimuthal distance of the ring. Once, constant coefficients are evaluated by fitting the fit function, the perturbation results are calculated with the fit function of the data in a region of $180° \pm 1°$. The fit value result is 14.3 ± 1.5 ppb. However, the footprint correction is 8 ppb, which is a more conservative estimate of error covering the full range of the error bars in Fig 7.27.

FID Extraction Difference between UMass and Hilbert Method

The trolley NMR frequency extraction algorithm (Chapter 6) used in the calibration analysis is identical to the one used in the field map analysis in order to ensure that the right quantity is calibrated. The well-shimmed field during rapid swapping and the long FIDs of the water-based NMR probe allows for a relatively simple frequency determination. Since this is a single point of failure in the ω_p analysis chain, this NMR frequency extraction is not only investigated in simulations but also cross-checked with a completely independent frequency extraction algorithm based on zero-crossings and an adaptive baseline correction developed by University of Massachusetts in Amherst (UMass). A more detailed description of the UMass (Zero-crossing) method can be found in [88]. In Run 1, the UMass algorithm was used for the calibration constant determination that was eventually used in the analysis chain. The Hilbert transform-based algorithm was used for cross-checking. However, in Run 2 and beyond, the Hilbert transform-based algorithm is used for the calibration constant determination, and the UMass algorithm is used for the cross-check. Table 8.1 shows the difference between the two frequency extraction algorithms of all plunging probe measurements during rapid swapping in the Run 3 calibration campaign. More detailed investigation and study will be presented in the next chapter 8.

7.2.3 Run3 Calibration Result

After combining every analysis step together, the final Run 3 calibration constant of the selected trolley probe i is combined as,

$$CC_i = B_{\mathrm{pp},i} - B_{\mathrm{tr},i} + B_{\mathrm{mis},i} + B_{\mathrm{bar},i} + B_{\mathrm{fp},i}, \tag{7.26}$$

where B_{pp} and B_{tr} are the plunging probe and trolley probe field measurements from the rapid swap, B_{mis} is the misalignment correction, B_{bar} is the barcode correction,

Probe	Hilbert Method (Hz)	UMass Method (Hz)	Differece (Hz)	Difference (PPB)
1	11101.0491	11101.2670	0.2179	3.5
2	10940.9076	10940.9450	0.0374	0.6
3	11140.0652	11140.0670	0.0018	0.0
4	11121.2655	11121.2500	-0.0155	-0.3
5	11191.5009	11191.5690	0.0681	1.1
6	10244.6310	10244.6110	-0.0200	-0.3
7	11098.2015	11098.2090	0.0075	0.1
8	10630.8019	10613.8378	0.0634	1.0
9	10800.2586	10800.2730	0.0144	0.2
10	10818.9366	10818.6120	-0.3246	-5.3
11	10730.0975	10729.8620	-0.2355	-3.8
12	10807.7843	10807.2030	-0.5813	-9.4
13	10823.7895	10823.7770	-0.0125	-0.2
14	10448.8441	10448.7820	-0.0621	-1.0
15	10653.3723	10653.3260	-0.0463	-0.7
16	10873.3268	10873.2210	-0.1058	-1.7
17	10123.8804	10101.2900	-0.0172	-0.3

Table 7.19: Results of differences between Hilbert and UMass frequency extraction methods per each probe during rapid swapping.

and B_{fp} is the footprint correction. The final uncertainties are separated into two parts: statistical and systematical uncertainties. The statistical ($\delta_{\text{stat},i}$) and systematical uncertainties ($\delta_{\text{syst},i}$) per probe i can be calculated as,

$$\delta_{\text{stat},i} = \sqrt{\delta^2_{\text{swap},i} + \delta^2_{\text{mis},i} + \delta^2_{\text{bar},i} + \delta^2_{\text{pos},i}} \tag{7.27}$$

$$\delta_{\text{syst},i} = \sqrt{\delta^2_{\text{fp},i} + \delta^2_{\text{act},i} + \delta^2_{\text{FID},i} + \delta^2_{\text{temp},i}}, \tag{7.28}$$

where δ_{swap} is the rapid swap uncertainty, δ_{mis} is the misalignment uncertainty, δ_{bar} is the barcode uncertainty, δ_{pos} is the 3D position repeatability uncertainty, δ_{fp} is the trolley footprint uncertainty, δ_{act} is the uncertainty from the active volume difference between the trolley and plunging probe, and δ_{FID} is the NMR frequency systematic uncertainty, and δ_{temp} is the temperature uncertainty.

The final Run 3 calibration constant results are in Table 7.20. All calibration constants are applied to the blind constant, which is within the 50 ppb levels. There are three different calibration constant results: calibration constant raw, calibration

	Run 3 Calibration Constant [Hz]						
Probe	Raw	Stat	Syst	PP Temp	Shielded	Stat	Syst
1	190.76	0.15	0.21	183.12	90.41	0.22	0.52
2	181.36	0.13	0.21	173.58	80.87	0.21	0.53
3	193.58	0.19	0.26	185.91	93.20	0.25	0.54
4	184.31	0.40	0.27	176.95	84.23	0.43	0.54
5	192.21	0.37	0.26	184.89	92.18	0.40	0.54
6	205.35	0.32	0.32	198.35	105.62	0.35	0.56
7	219.38	0.36	0.30	212.37	119.65	0.38	0.55
8	174.73	0.39	0.19	167.84	75.11	0.42	0.49
9	184.95	0.37	0.42	178.09	85.36	0.40	0.62
10	124.24	0.37	0.61	117.31	24.59	0.39	0.76
11	275.20	0.42	0.68	268.34	175.61	0.45	0.82
12	207.23	0.36	1.05	200.41	107.68	0.38	1.14
13	222.50	0.30	0.31	215.67	122.94	0.33	0.55
14	176.78	0.43	0.43	170.09	77.36	0.45	0.62
15	174.21	0.56	0.60	167.29	74.57	0.58	0.76
16	118.42	0.64	0.30	111.47	18.74	0.66	0.55
17	267.06	0.41	0.69	260.42	167.69	0.43	0.83

Table 7.20: Final results of Run 3 calibration constant with plunging probe temperature corrections and shield proton corrections.

constant with only plunging probe temperature correction, and calibration constant with both Plunging Probe and shielded proton corrections.

7.2.4 Comparison Between Different Analyzer

The primary analyzer for the Run 3 calibration analysis, Yi Bingzhi, uses different fixed probe selections for the oscillation correction. Besides that, most of the analysis steps are identically the same. However, the primary analyzer uses C/C++ macro scripts and I use Python-based GM2 library packages for data-driven analysis. For systemic uncertainty, the primary analyzer uses my FID extraction uncertainty for the final result. The temperature correction comparisons between two analyzers are shown in Table 7.21. The shielded correction comparisons are shown in Table 7.22. The final Run 3 calibration constant comparisons are shown in Fig 7.28.

	Temperature Correction [Hz]		
Probe	Yi	Chris	Difference
1	-7.67	7.67	0.00
2	-7.80	7.81	0.01
3	-7.71	7.71	0.00
4	-7.39	7.40	0.01
5	-7.36	7.37	0.01
6	-6.99	7.00	0.01
7	-7.00	7.00	0.01
8	-6.92	6.92	0.00
9	-6.88	6.89	0.01
10	-6.89	6.90	0.01
11	-6.84	6.85	0.01
12	-6.79	6.80	0.01
13	-6.83	6.84	0.01
14	-6.69	6.70	0.01
15	-6.96	6.96	0.00
16	-6.95	6.95	0.00
17	-6.62	6.62	0.00

Table 7.21: Temperature dependency of the diamagnetic shielding of water comparison between Yi and I.

7.2.5 Summary

Compared to the Run 2 calibration campaign, many new features for analysis are added such as an automatic rapid swapping script and cube scan. Automatic script reduces human error and cube scan helps to understand the uncertainty of cross terms.

There are two different analyzers with silently different approaches and tools for the Run 3 calibration study. Two parallel studies are a good way to cross-check the results. In conclusion, there are no main differences between the final results, which are expected.

The uncertainty in total (statistic and systemic uncertainty) is about 10.2 ppb on average, which achieves the 30 ppb goals of the experiment.

	Shielded Proton Correction [Hz]		
Probe	Yi	Chris	Difference
1	100.67	100.38	0.29
2	100.80	100.52	0.28
3	100.71	100.42	0.29
4	100.40	100.12	0.28
5	100.37	100.09	0.29
6	100.01	99.73	0.29
7	100.01	99.73	0.28
8	99.94	99.65	0.29
9	99.90	99.61	0.28
10	99.91	99.62	0.28
11	99.86	99.57	0.29
12	99.81	99.52	0.28
13	99.85	99.57	0.28
14	99.71	99.43	0.29
15	99.98	99.69	0.29
16	99.97	99.68	0.29
17	99.65	99.36	0.29

Table 7.22: Shielded proton correction due to the bulk magnetic susceptibility and comparison between Yi and I.

7.2.6 Preliminary Result: Pre-Run 4 Calibration Analysis

After finishing the Run 3 calibration analysis, I start to look at pre-Run 4 calibration data. Pre-Run 4 analysis steps and studies are almost identical to Run 3 calibration analysis with minor tuning on a few fitting parameters. Table 7.23 shows the preliminary pre-Run 4 calibration constant result with the plunging probe, shielded proton correction, corresponding statistic, and systematic uncertainties. Both Run 3 and pre-Run 4 raw calibration constants and the differences between the two are shown in Fig 7.29. The mean difference is 0.38 $\pm$ 0.96 Hz, which is 6.1 ppb.

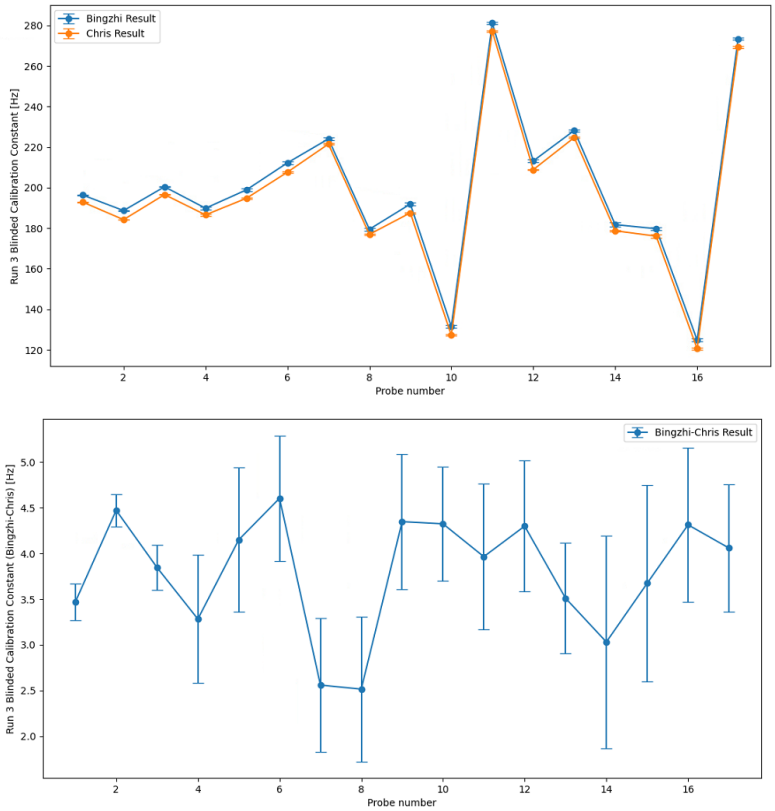

FIGURE 7.28: Top Plot: Run 3 calibration constant raw result with blinded constant. Bottom Plot: The difference between the two results.

	Run 4 Calibration Constant [Hz]						
Probe	Raw	Stat	Syst	PP Temp	Shielded	Stat	Syst
1	188.77	0.31	0.24	183.10	90.06	0.35	0.54
2	181.79	0.37	0.18	175.87	82.83	0.43	0.52
3	192.64	0.29	0.26	186.85	93.81	0.34	0.55
4	183.48	0.35	0.43	177.54	84.50	0.40	0.65
5	193.22	0.47	0.33	187.16	94.12	0.50	0.60
6	205.72	0.47	0.35	199.81	106.77	0.52	0.61
7	218.34	0.69	0.39	212.45	119.41	0.72	0.62
8	173.81	0.76	0.47	167.84	74.80	0.78	0.68
9	185.83	0.42	0.55	179.62	86.59	0.48	0.74
10	124.04	0.48	0.39	118.28	25.23	0.52	0.63
11	274.75	0.46	1.09	268.88	175.84	0.50	1.19
12	206.39	0.58	1.42	200.33	107.30	0.61	1.50
13	222.58	0.42	0.60	216.69	123.65	0.46	0.77
14	178.06	0.72	0.86	171.89	78.86	0.74	0.99
15	173.17	0.29	1.41	167.41	74.37	0.35	1.49
16	117.84	0.40	0.53	111.86	18.83	0.44	0.72
17	267.41	1.15	1.41	261.52	168.48	1.17	1.49

Table 7.23: Pre-Run 4 preliminary calibration constant with statistic and systematic uncertainties. PP Temp is plunging probe temperature correction and Shielded is shielded proton correction.

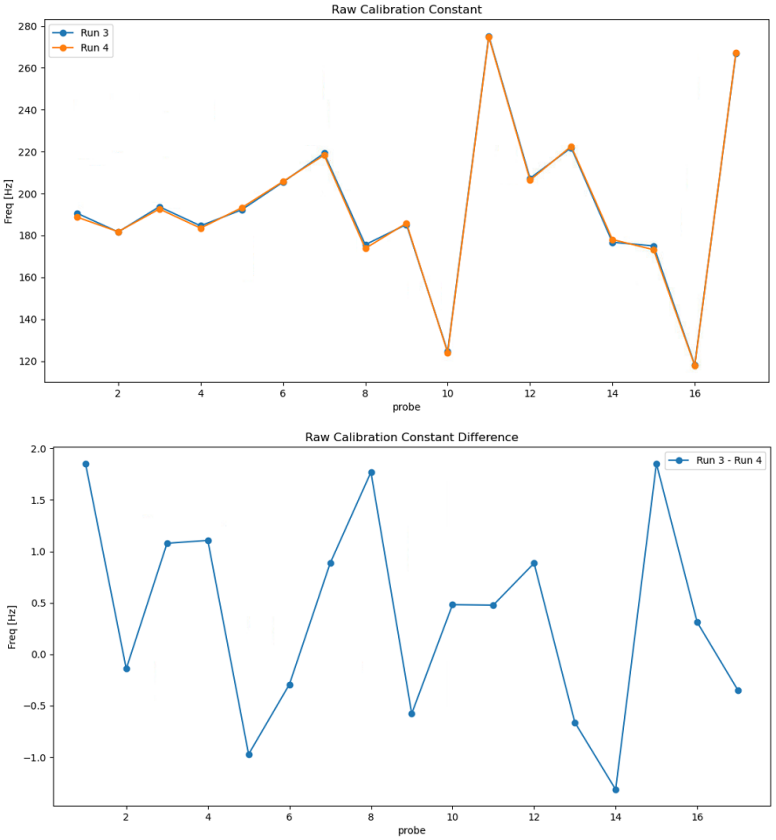

FIGURE 7.29: Top: blue is for Run 3 raw calibration constants and orange is for pre-Run 4 raw calibration constants. Bottom: the differences between Run 3 and pre-Run 4 calibration constants.

8

Plunging Probe FID Freq Extraction and Uncertainty

8.1 Plunging Probe FID Overview

The plunging probe is used to calibrate the trolley probe during the calibration campaign (Section 7.2). The local oscillator (LO) for the plunging probe system is detuned from the expected NMR frequency by ∼10 kHz. The FID is sampled at 10 MHz for 500 ms. The constant baseline of the signal is determined at a long-time region of the signal where the FID signal decays away [83].

During the calibration campaign, the plunging probe is at the calibration target where the field is shimmed to high uniformity or applied a high linear gradient. The shimmed uniformity field is used for the rapid swap (Section 7.2.1.4) and the applied high linear field is used for the Δ B measurements (Section 7.2.1.2) for determining the relative position between the plunging probe and the selected trolley probe.

8.1.1 Shimmed Field

Due to the highly uniform field, the plunging probe FIDs have long signals. One of the plunging probe FIDs is shown in the top plot from Fig 8.1. The plunging probe

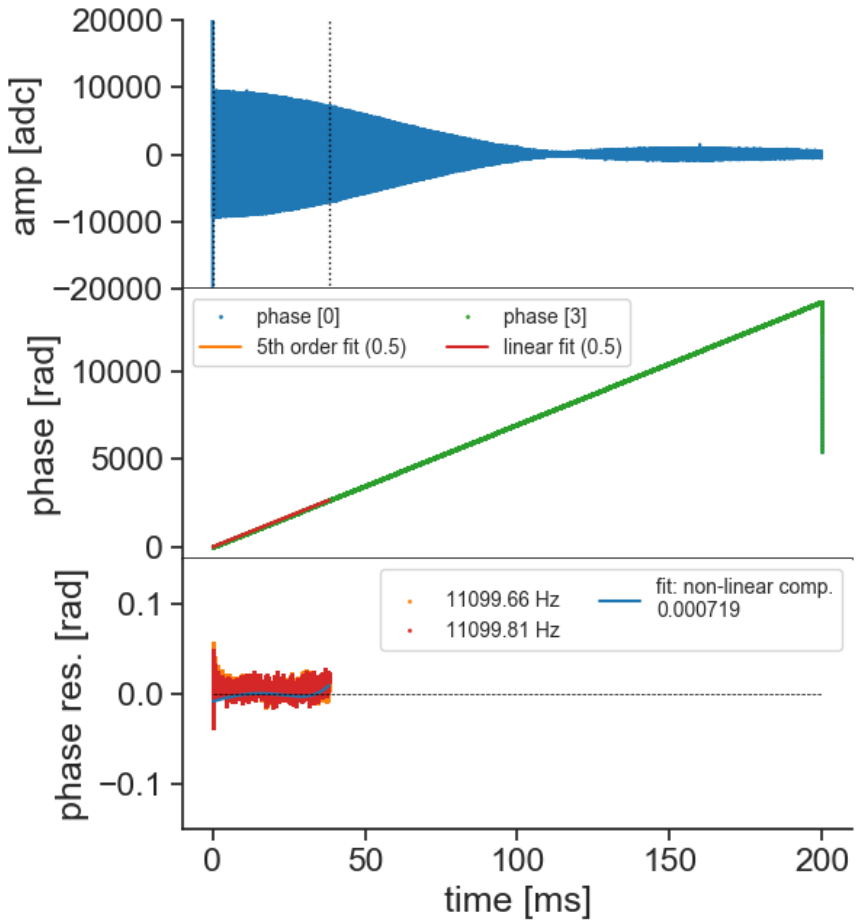

FIGURE 8.1: Plunging probe FID at the center of the trolley during rapid swapping. Rest of probes FID is at Appendix C.3.

FID is typically around 100 ms long. The phase function, which is shown in the second plot from Fig 8.1, is calculated exactly as described in Chapter 5. Then the polynomial fit of $\phi(t)$, the orange and red lines on the phase function in the second plot from Fig 8.1, is performed in the half of the range from the maximum amplitude to $1/e$ of its maximum amplitude and a 1 ms veto window is applied to the beginning and end of the fit window to avoid artifacts. The frequency is the fit value of $\phi(t)/dt$ in the polynomial fits. The residuals are shown in the bottom plot of Fig 8.1. One shows the residuals from a linear fit and the other from a polynomial with odd terms up to the 5^{th} order.

For the calibration analysis, there are at least two different approaches to cross-checking the result at the end. One uses the Hilbert transform method and another uses the zero-crossing method to extract its frequencies during the rapid swap. Detailed studies of comparison between the two methods are discussed in the next section.

8.2 Plunging Probe FID Extraction Method

8.2.1 Overview

The plunging probe NMR frequency extraction algorithm (Section 7.1) used in the calibration analysis is identical to the one used in the field map analysis in order to ensure that the right quantity is calibrated. The frequency extraction used for the plunging probe uses the same library and package and follows the same scheme.

1. A Hilbert transform is used to extract the phase function.

2. The phase function is smoothed in two iterations before it is fitted with a 5^{th} order polynomial in the first 50% of the FID length.

3. The FID length is defined from the maximal amplitude of the envelope to 1/e of its maximal amplitude.

8.2.2 Two Methods: Hilbert vs UMass

As described in Section 7.2.2.7, in Run 1, the UMass algorithm was used for the calibration constant determination that was eventually used in the analysis chain. The Hilbert transform-based algorithm was used for cross-checking. However, in Run 2 and beyond, the Hilbert transform-based algorithm is used for the calibration constant determination, and the UMass algorithm is used for cross-checking. Table 8.1 shows the difference between the two frequency extraction algorithms of all the plunging probe measurements during rapid swapping in the Run3 calibration campaign.

Probe	Hilbert Method (Hz)	UMass Method (Hz)	Differece (Hz)	Difference (PPB)
1	11101.0491	11101.2670	0.2179	3.5
2	10940.9076	10940.9450	0.0374	0.6
3	11140.0652	11140.0670	0.0018	0.0
4	11121.2655	11121.2500	-0.0155	-0.3
5	11191.5009	11191.5690	0.0681	1.1
6	10244.6310	10244.6110	-0.0200	-0.3
7	11098.2015	11098.2090	0.0075	0.1
8	10630.8019	10613.8378	0.0634	1.0
9	10800.2586	10800.2730	0.0144	0.2
10	10818.9366	10818.6120	-0.3246	-5.3
11	10730.0975	10729.8620	-0.2355	-3.8
12	10807.7843	10807.2030	-0.5813	-9.4
13	10823.7895	10823.7770	-0.0125	-0.2
14	10448.8441	10448.7820	-0.0621	-1.0
15	10653.3723	10653.3260	-0.0463	-0.7
16	10873.3268	10873.2210	-0.1058	-1.7
17	10123.8804	10101.2900	-0.0172	-0.3

Table 8.1: Results of difference between Hilbert and UMass frequency extraction methods per each probe during rapid swapping.

I decided to investigate the plunging probe study after I found out that there are unexpected large deviations for probes 1, 10, 11, and 12. For the detailed plots, Run 3 plunging probe FID for each rapid swap is shown in Appendix C.3. Run 3 plunging probe frequency extraction as a function of fit lengths and the frequency extraction as a function of polynomial orders is shown in Appendix C.3.

8.2.3 Uncertainty Studies

The differences in frequency extractions for probes 3 and 12 are 0.0 and 9.4 ppb. Fig 8.2 shows the plunging probe FID plots for probes 3 and 12. The FIDs of both probes look fine. However, the shapes of phase residual plots in Fig 8.2 are different between probes 3 and 12. Probe 12's residual plot has more curves while probe 3's residual plot is almost flat. Moreover, the fit window of probe 12 is longer than the fit window of probe 3. Because of the residual plot's curvature shape, the fit is more sensitive to polynomial orders and fit window lengths. For example, the phase residual plots with different polynomial order fit are shown in Fig 8.3. Depending

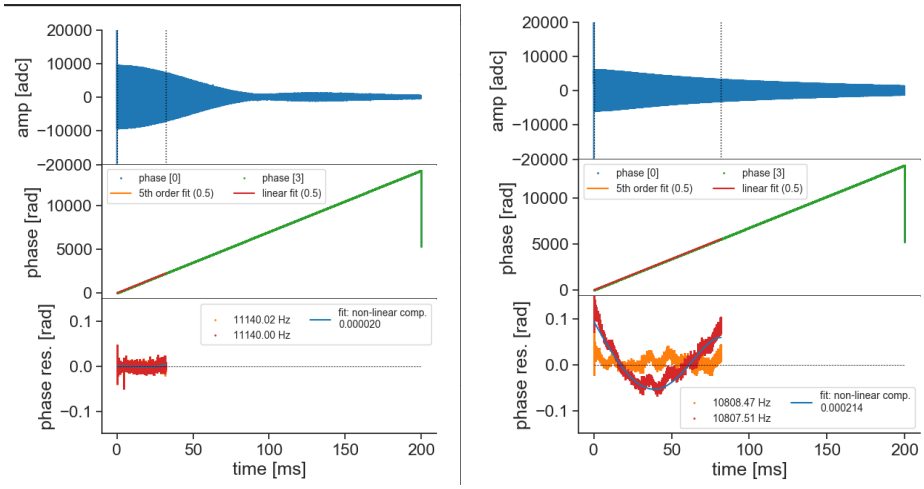

FIGURE 8.2: Left plot is plunging probe FID for probe 3 and the right plot is plunging probe FID for probe 12

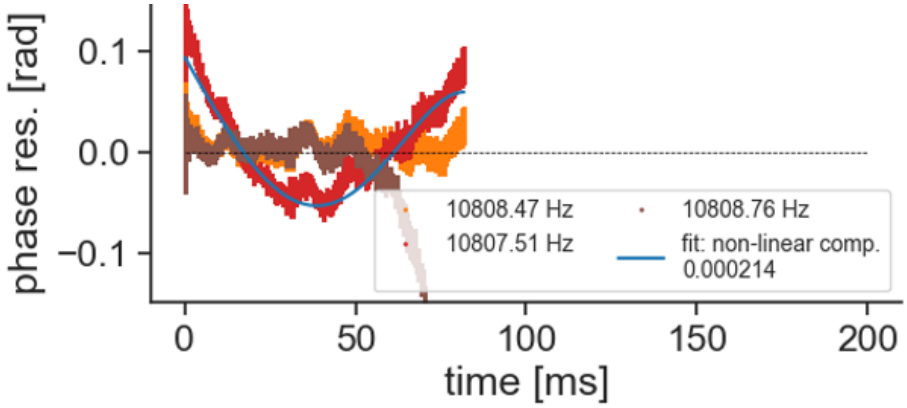

FIGURE 8.3: The phase residual plot for probe 12 with different polynomial orders fitting: Red(linear), Orange(5^{th} order), and Brown(7^{th} order)

on the polynomial order, Fig 8.3 shows different residual shapes. Because of the different residual shapes, the plunging probe frequency extraction can be different. Fig 8.4 shows relative frequencies as a function of different polynomial orders of probes 12 and 17. The plot shows that probe 12's relative frequencies are highly dependent on the polynomial order. Fig 8.5 shows the frequencies as a function of different fit window lengths of probes 12 and 17.

In order to compare how much the analysis choices of the frequency extraction

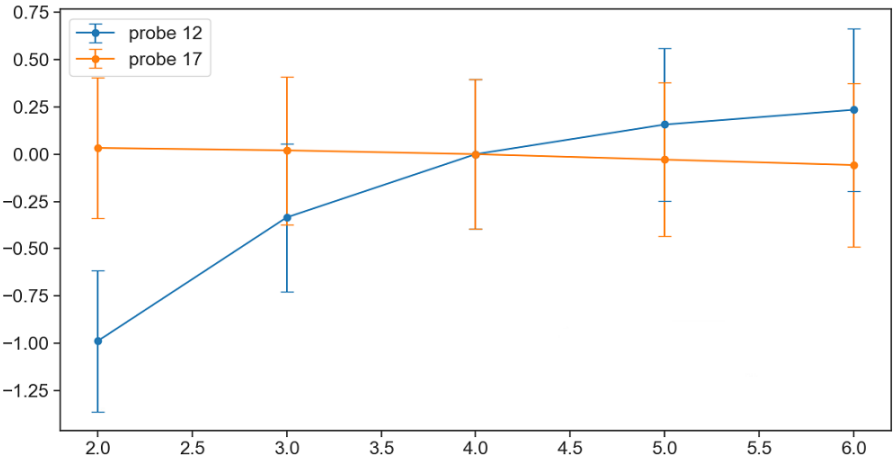

FIGURE 8.4: Relative frequencies of probe 12 and 17 with different polynomial orders. X-axis shows the different polynomial orders and the y-axis shows the relative frequencies in Hz. The error bars represent uncertainties from events at each parameter setting.

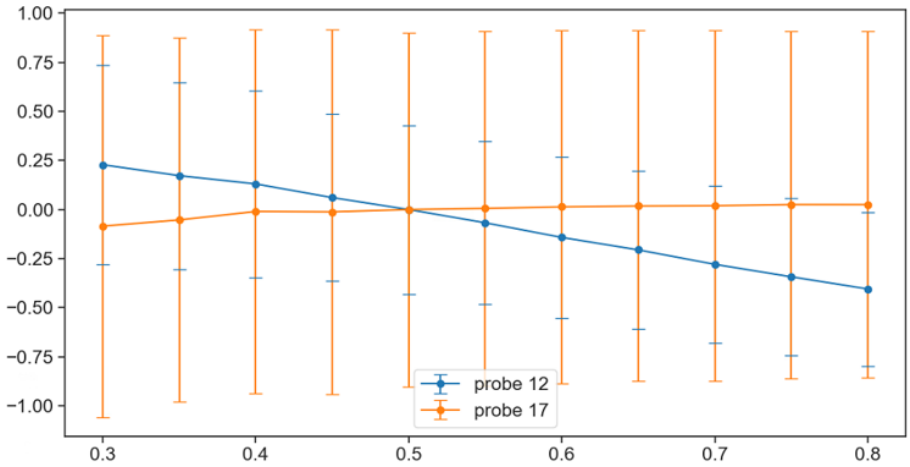

FIGURE 8.5: The frequencies of probes 12 and 17 with different fit window lengths with the same polynomial order of 5. The x-axis shows the different fit window lengths and the y-axis shows the relative frequencies in Hz.

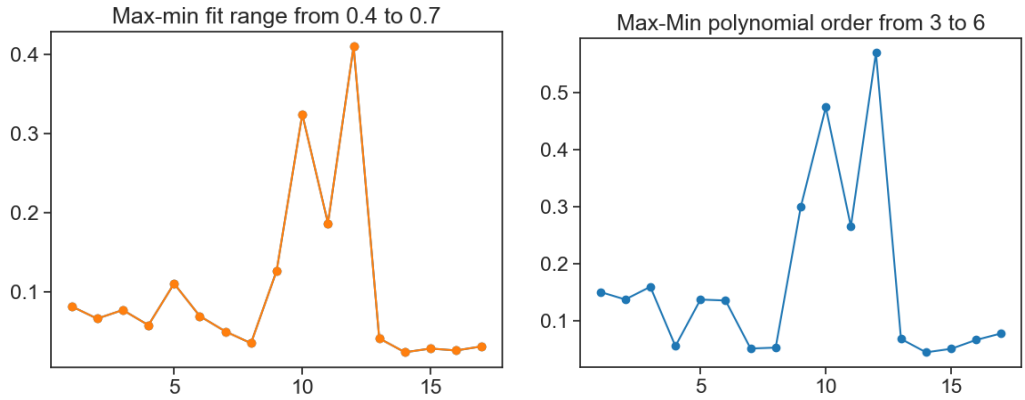

FIGURE 8.6: The left plot shows the difference between the maximum and minimum values of the fit window lengths from the selected parameter, ranging from 0.4 to 0.7 per probe number. The right plot shows the difference between the maximum and minimum values of the polynomial order from the selected parameter, ranging from 3 to 6 per probe number.

algorithm affect actual frequency extraction, the difference between the maximum and minimum values on selected parameter ranges is calculated and plotted as a function of probe numbers. The selected ranges for fit window length are from 0.4 to 0.7, where 0.5 is the default setting. The selected ranges for the polynomial order fit parameters are from 3^{rd} order to 9^{th} order, where 5^{textth} order is the default setting shown in Fig 8.6. From Fig 8.6, the pattern of the left and right plots are similar: there are peaks at probes 10, 11, and 12 which is matched with the three probes that are the largest differences between Hilbert and UMass among all probes. I decide to look at other Run data: the current analysis is based on Run 3. Fig 8.7 shows the differences between the maximum and minimum frequencies of the fit window lengths from the selected parameter, ranging from 0.4 to 0.7 per probe number of each Run's calibration campaign. At the moment, Run 4, Run 5, and Run 6 calibration analyses are not completed so only Run 2 and Run 3 analyses are ready to be investigated on what causes the large frequency difference depending on the analysis choices (fit length window and polynomial orders) of the frequency extraction algorithm. For investigations, I choose the selected variables such as amplitude, time, and azimuth

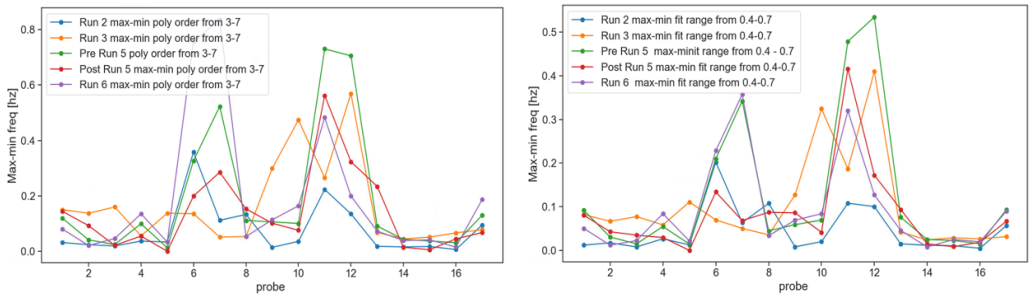

FIGURE 8.7: The left plot shows the difference between the maximum and minimum values of the fit window lengths from the selected parameter, ranging from 0.4 to 0.7 per probe number of each Run. The right plot shows the difference between the maximum and minimum values of the polynomial order from the selected parameter, ranging from 3 to 6 per probe number of each Run.

second-order gradient to find out any correlations.

Fig 8.8 shows the FID length as a function of the difference in frequency extraction with different calibration campaigns (from Run 2 to Run 6). I am not sure about Run 3 because the Run 3 plot is not similar to other plots. My hypothesis is that there are huge outliers that cause huge differences between the maximum and minimum extracted frequencies. Besides Run 3, all other Runs behave the same in that longer FID lengths tend to be less sensitive to analysis choices. This makes sense because longer FID lengths have less sensitivity to higher order polynomial terms.

8.3 Summary

The standard plunging probe frequency extraction uses the Hilbert transform as same as the trolley probe frequency extraction. The plunging probe phase function is smoothed in two iterations before it is fitted with a 5^{th} order polynomial in the first 50 % of the FID length. During rapid swapping in the calibration campaigns, the local field is well-shimmed and the resulting long FIDs of the water-based NMR probe of multiple 100 ms allow for a relatively simple frequency determination. There is a completely independent frequency extraction algorithm based on zero-crossing

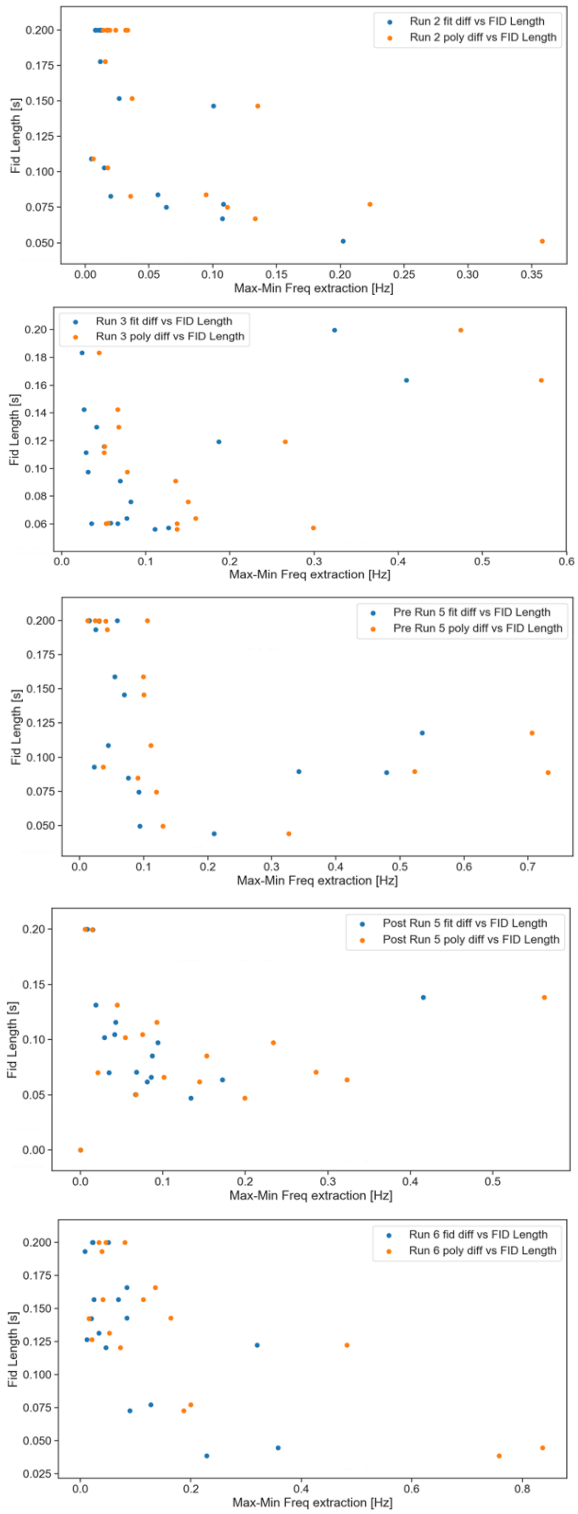

FIGURE 8.8: The plots represent the FID length as a function of the difference in extracted frequencies. From top to bottom, it starts with Run 2, Run 3, Pre Run 5, Post Run 5, and Run 6.

δ^{freq} [ppb]	dipole	NQ	SQ	N6
run2	<1	<1	2	1
run3	<1	1	2	2
combined	<1	1	2	2

Table 8.2: Uncertainty from frequency extraction (δ^{freq}) on the calibration constant propagated to multipoles.

and an adaptive baseline correction developed by UMass to cross-check the standard NMR frequency extraction results.

Analysis choices of the frequency extraction algorithm, such as the fit window length and polynomial order, are expected to have a minimal effect on the extracted frequencies in a very well-shimmed field. In order to quantify the effect these degrees of freedom of analysis choices have, the parameters for the plunging probe frequency extraction are varied, and the effect on the calibration constants is evaluated. This yield an uncertainty from frequency extraction.

For the study, the fit length is varied between 0.4 to 0.7 (nominal 0.5) of the FID length. Polynomial orders with 3 to 6 degrees of freedom (nominal 4) are used. I decided on the range of analysis choices because we consider a reasonable, yet conservative range of the FID frequency extraction settings. The effect is quantified by the maximal range of difference with respect to the nominal. Plots and detailed study methods are explained in the previous section.

Since these effects are mostly uncorrelated between the different probes, the effect on the dipole is suppressed. Fig 8.9 shows an overview of the effect on the dipole and higher multipoles. Table 8.2 summarizes the uncertainty associated with the plunging probe frequency extraction. This is a sub-ppb effect for the dipole and a max 2 ppb effect for higher-order moments.

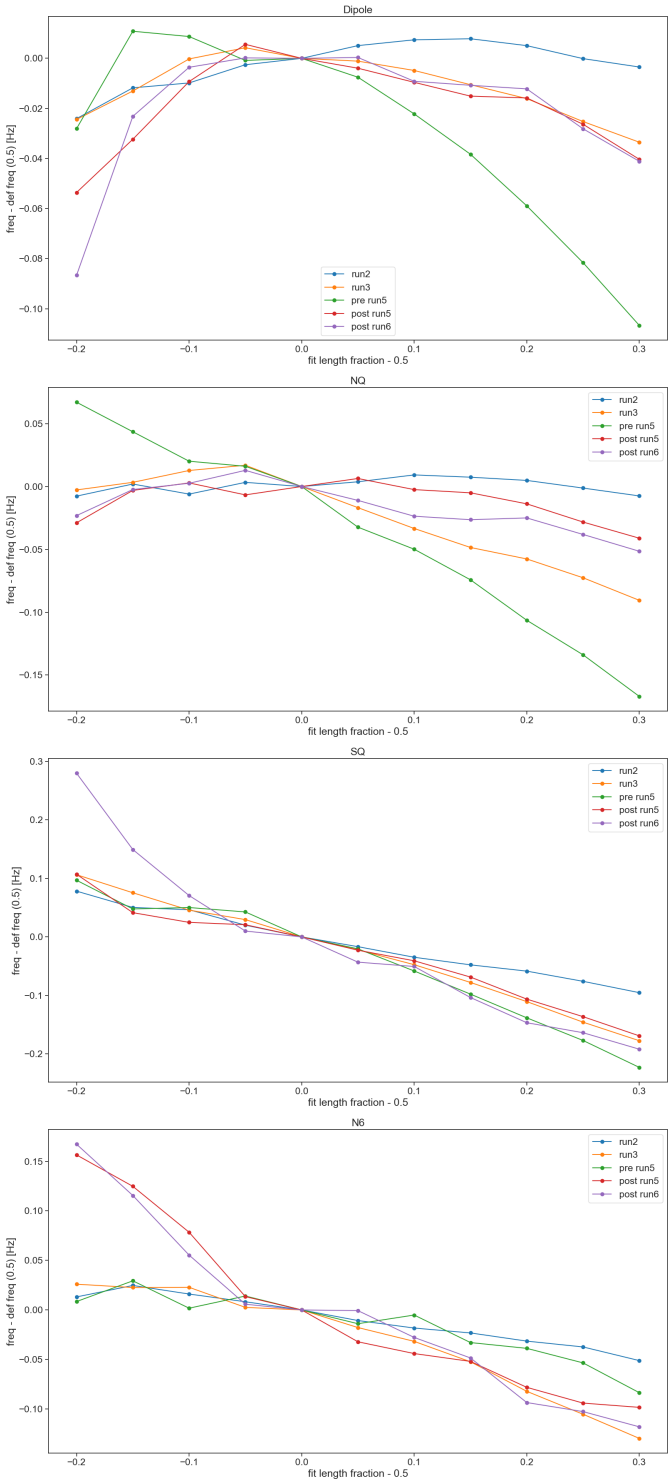

FIGURE 8.9: The plots represent the multipole subtract with multipole value at the default setting (fit length fraction = 0.5) as a function of fit length fraction - 0.5. From top to bottom, it starts with a dipole, norm quadrupole, skew quadrupole, and norm sextupole.

9

Field Measurement Systematics

FID frequency extraction has a crucial role in the magnetic field measurement. The collaboration developed the FID models and built the fundamental framework for the experiment [83]. They studied noise, baseline, and distortion. With these NMR FID analyses, they also applied it to the trolley calibration to make sure the trolley probes were well-tuned. Run 1 field analysis was based on their work, simulation, and framework. There are two papers that can be found in DocDB (Muon g-2 Internal), Muon g-2 NMR Frequency Extraction [83], and Muon g-2 Trolley Calibration [82]. Both papers explain the detail of NMR probes' FID and how FID models and frameworks are constructed.

It is important to study the same effects also for beyond Run 1. In this chapter, I will review Run 1 uncertainty analysis and I will introduce my reinterpretation and a new approach to the systematic uncertainty for Run 2 and beyond.

9.1 Run 1 Uncertainty Analysis

Chapter 5 introduced NMR techniques such as FID frequency extraction and simulation. After the RF pulse, the proton spins precess and the magnetic field induces EMF

Type	Sample L (mm)	Sample R (mm)	Coil L (mm)	Coil R (mm)	Coil N
Plunging Probe	40	2.12	11	7.5	5
Trolley Probe (Short)	33.5	1.25	7	2.3	Layer 1: 9 Layer 2: 8
Trolley Probe (Long)	33.5	1.25	15	2.3	Layer 1: 28 Layer 2: 2 at each end
Fixed Probe	33.5	1.25	15	2.3	Layer 1: 28 Layer 2: 2 at each end

Table 9.1: List of probe geometries [83].

in the pick-up coil. Then, this signal is read out by electronics. Equation 5.2 shows that the response function of coil $\eta(x, y, z)$ contributes to the FID signal. There are three NMR probes used in the experiment: trolley, fixed probe, and plunging probe. Each probe has a different probe geometry and coil lengths, so each probe's FID looks different. Therefore, it is important to study the NMR measurement systematics from different NMR probe geometry by using simulation.

9.1.1 NMR Probe geometry and sensitivity center

The sample dimensions and coil dimensions are significantly important variables to understand the probe geometry in the simulation. Table 9.1 shows the details of the probe geometry variables.

In the simulation, there are a few assumptions to generate the spin precession and the signal in the pick-up coil. The external magnetic field is in the y direction and the coil axis is in the z-direction. Due to the non-uniform field, the spin precession is in the XZ plane. Then, the signal strength generated by a spin precession is proportional to $\mu_{\mathrm{XZ}} B_{\mathrm{ZX}}$ and the initial spin magnetic moment, μ_{XZ} is proportional to $sin(kB_{\mathrm{ZX}})$. In the simulation, k is tuned to be $kB_{\mathrm{xz}} = \pi/2$ at the center of the coil due to the RF pulse. Therefore, the signal strength, or the sensitivity, of the probe to a precessing spin at a position is defined,

$$S(x, y, z) = C \cdot B_{\mathrm{XZ}} sin(kB_{\mathrm{XZ}}), \tag{9.1}$$

where C is a normalization constant in the sample volume: $\int\int\int_V S(x, y, z)dxdydz =$

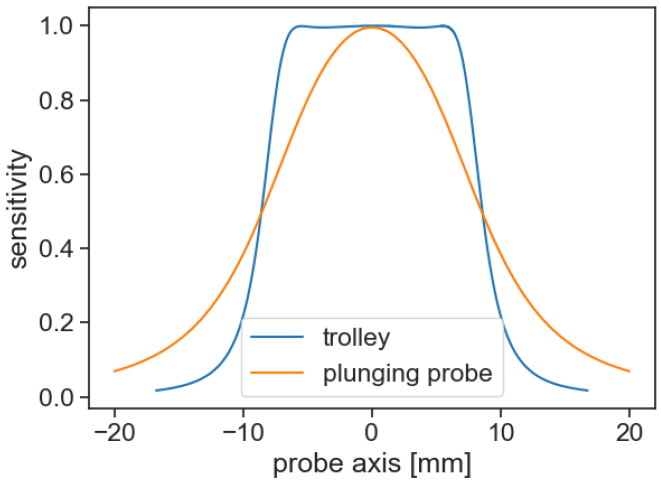

FIGURE 9.1: Sensitivity functions for trolley and plunging probes.

1.

According to Equation 5.2, the contributions to the signal are $\Omega(x, y, z)$, $A(x, y, z)$, and $\eta(x, y, z)$. In simulation, $A = Csin(kB_{\mathrm{XZ}})$ and $\eta = B_{\mathrm{XZ}}$. Then, the signal strength average frequency $\overline{\omega}$ can be expressed as

$$\overline{\omega} = \int\int\int \Omega(x, y, z)S(x, y, z)dxdydz \tag{9.2}$$

Fig 9.1 shows how the probe sensitivity functions look like for the trolley probe long and the plunging probes.

9.1.2 Fit Accuracy and Probe Accuracy

9.1.2.1 Fit Accuracy

The *fit accuracy* δ is defined as the difference between the extracted ω from the FID analysis and the true ω calculated based on the average frequency and the probe sensitivity function [83].

$$\delta = \omega_{\mathrm{extracted}} - \overline{\omega} \tag{9.3}$$

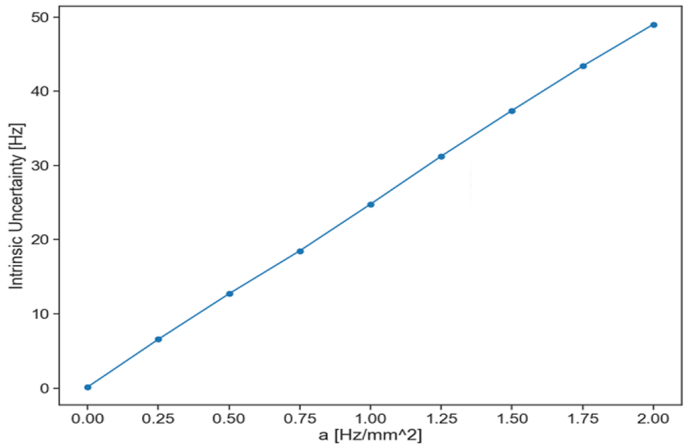

FIGURE 9.2: Probe Accuracy (Intrinsic Uncertainty) ϵ as a function of the second order field gradient a

9.1.2.2 Probe Accuracy (Intrinsic Uncertainty)

The *probe accuracy (intrinsic uncertainty)* ϵ is defined as the difference between $\overline{\omega}$ and the field at the probe sensitivity center, ω_C [83]:

$$\epsilon = \overline{\omega} - \omega_C. \tag{9.4}$$

ω_{truth} and ω_C are different in non-linear gradient and the relationship between ϵ and non-linear field can be addressed through simulation. Let the external magnetic field be as $\Omega(z) = az^2 + bz + \Omega_0$. To illustrate the dependence of ϵ on the second order gradient is to fix the coefficient b to be 10 Hz/mm while a is scanned from 0 to 2 Hz/mm^2. As shown in Fig 9.2, the probe accuracy (intrinsic uncertainty) ϵ has a strong correlation to the second-order field gradient [83].

9.1.3 Run 1 Calibration

Three independent analyzers had done blinded studies for Run 1 calibration analyses by using independent methods. At the end, everyone's results are within less than 5 ppb. The detailed notes of the Run 1 calibration analyses can be found here: E989 Note 191: Magnetic Field Calibration Analysis for Run 1 [88] and E989 Note 230:

Probe ID	PP FIT (HZ)	PP Intrinsic (Hz)	TRLY Fit (Hz)	TRLY Intrinsic (Hz)
1	-0.001	1.573	-0.022	1.191
2	0.000	1.798	-0.016	1.361
3	-0.001	1.616	-0.022	1.223
4	0.000	0.057	-0.019	0.043
5	0.000	0.200	-0.018	0.151
6	-0.159	5.553	-0.019	4.146
7	-0.258	6.396	-0.021	4.146
8	0.231	-5.024	-0.023	-3.802
9	-0.004	2.126	-0.022	1.610
10	-0.011	2.919	-0.019	2.209
11	-0.311	6.409	-0.022	4.449
12	-0.124	5.772	-0.018	4.222
13	-0.187	6.395	-0.019	4.439
14	-0.150	6.281	-0.019	4.399
15	-0.204	5.369	-0.020	4.063
16	-0.186	5.939	-0.019	4.280
17	-0.159	6.396	-0.019	4.439

Table 9.2: Fit and intrinsic uncertainties for trolley probes and the plunging probes during Run 1 rapid swap [83].

Trolley Calibration Analysis for Run1 [89].

During the calibration campaign, the local field at the calibration region is shimmed so that the higher-order gradient of the local field is reduced significantly, and the local field shape is well-known. Then, simulated FIDs can be generated from the known field shape and the intrinsic uncertainties can be evaluated from these simulated FIDs.

9.1.3.1 Trolley Probe and Plunging Probe

Table 9.2 shows the result of the fit and intrinsic uncertainties of each trolley probe and plunging probe in the calibration region and intrinsic uncertainty dominates the total error. The trolley probe's intrinsic uncertainty ϵ_t is important in the calibration and more details can be found in chapter 7.

9.1.4 Systematic Uncertainty for the Azimuthally Averaged Field

9.1.4.1 Systematic Uncertainty Evaluation for a Field Scan

The systematic uncertainty, both fit and intrinsic uncertainties, can be evaluated from the simulated FID using the local field derived from the measurement because the truth of the field at the probe center and the average frequency weighted by the probe sensitivity function are given by the simulation.

First, the field non-uniformity in this example field scan is investigated. As shown in Fig 9.3, the dB/dz (top) and d^2B/dz^2 (bottom) as a function of the azimuthal position for probe 1, 5, 9, and 12. The reason why these probes are selected is that they are located at the center of the trolley (probe 1), in the middle layer (probe 5), the closest to the inflector (probe 9) and the closest to the pole surface (probe 12). Normally, the dB/dz and d^2B/dz^2 are up to 40 Hz/mm and 0.5 Hz/mm^2. However, in the worst case, on the inflector region (probe 9), the dB/dz and d^2B/dz^2 can be up to 200 Hz/mm and 5 Hz/mm^2, respectively.

For the events in the normal field, dB/dz and d^2B/dz^2 are scanned in ranges from 1 to 40 Hz/mm and from 0 to 0.5 Hz/mm^2 with 10 steps each. For the events in the extreme field, dB/dz and d^2B/dz^2 are scanned from 1 to 200 Hz/mm and from 0 to 5 Hz/mm^2 with 10 steps each. The fit accuracy scan results for normal and extreme events are shown in Fig 9.4 [83].

9.1.4.2 Systematic Uncertainty Evaluation for the azimuthally averaged field

When calculating the azimuthally averaged field, these uncertainties for all events are completely correlated [83]. Therefore, the total fit and intrinsic uncertainties of the azimuthally averaged frequency for a given probe can be calculated by the average of uncertainties, summing the uncertainties of all the events divided by the total number of events. The fit uncertainty (top) and intrinsic uncertainty (bottom) as a function of azimuthal position for probes 1, 5, 9, and 12 are shown in Figure 9.5.

Probe ID	Fit Unc (δ)	Intrinsic Unc (ϵ)
1	0.033	0.0017
2	0.048	0.0014
3	0.034	-0.0015
4	0.029	-0.0025
5	0.020	-0.0026
6	0.029	-0.0187
7	0.079	-0.0164
8	0.039	-0.0090
9	0.098	-0.0052
10	0.036	-0.0028
11	0.043	0.0185
12	0.051	-0.0191
13	0.037	-0.0217
14	0.025	-0.0156
15	0.021	-0.0077
16	0.048	-0.0083
17	0.031	0.0005
mean	0.041	-0.0064
std	0.0196	0.0097

Table 9.3: Fit and intrinsic uncertainties for the azimuthally averaged frequencies of trolley probes in a unit of Hz [83].

The uncertainties of each trolley probe are shown in Table 9.3.

9.2 Calibration: Active Volume Analysis

The active volume analysis was briefly discussed in the previous section (see Section 7.2.2.7). In this section, I will look at the active volume difference between the trolley and plunging probe in more detail, specifically on Run 2 and Run 3 calibration rapid swap datasets. This study is motivated by the active volume of the plunging probe and the trolley being different due to the different probe geometries, so there should be a correction between measurements of the two probes because the extracted NMR frequency corresponds to the average frequency in the active volume throughout the non-homogeneous fields with the non-zero second order gradients.

For the analysis, I use Run 2 and Run 3 online cross scan measurements. The

Probe ID	dB_x/dx	dB_y/dy	dB_z/dz	d^2B_x/dx^2	d^2B_y/dy^2	d^2B_z/dz^2
1	-0.88	0.02	0.95	-0.02	0.07	0.25
2	-0.20	0.11	1.44	-0.19	0.07	0.24
3	0.22	-0.13	-0.23	-0.05	0.22	-0.03
4	-0.02	0.78	-0.09	-0.07	-0.05	-0.18
5	0.67	0.39	3.53	-0.03	0.07	0.63
6	-0.75	1.11	-0.20	-0.45	0.64	0.09
7	0.00	0.00	0.00	0.00	0.00	0.01
8	0.00	0.00	0.00	0.00	0.00	0.01
9	0.52	-0.87	6.60	-0.36	0.19	0.92
10	0.28	0.03	-1.15	-0.03	0.01	-0.06
11	-1.79	-0.93	-0.15	-0.16	0.00	0.15
12	0.12	0.22	2.02	-0.21	0.14	0.36
13	-0.18	-0.55	-1.25	0.41	-0.29	-0.23
14	-0.63	-0.75	0.47	0.28	-0.34	0.08
15	0.17	0.68	-1.03	-0.07	0.07	-0.21
16	0.86	0.73	0.05	0.00	-0.07	-0.01
17	0.78	-0.59	-0.17	-0.63	0.62	0.00

Table 9.4: Run 2 online cross scan results per probe: the first shimmed gradient of x, y, and z in a unit of Hz/mm and the second order shimmed gradient of x, y, and z in a unit of Hz/mm^2.

Run 2 online cross scan results per probe are shown in Table 9.4 and the Run 3 online cross scan results per probe are shown in Table 9.5.

Once I obtained shim gradients from an online cross-scan dataset of Run 2 and Run 3, I use the simulation tools to generate the average frequencies over the active volume of each probe. The result is shown in Table 9.6 and it shows the trolley and plunging probe simulated frequencies and the differences between the two frequencies.

As a result, the Run 3 active volume difference is smaller than the Run 2 active volume difference because Run 3 has smaller second-order gradients. Uncertainties can be addressed from shim gradient uncertainty, repeatability uncertainty, and coil length uncertainty. First, shim gradient uncertainty is the uncertainty from the second-order gradients in the z-direction. Since the second-order gradients in the z-direction are the dominant factors, I only considered the second-order azimuthal

Probe ID	dB_x/dx	dB_y/dy	dB_z/dz	d^2B_x/dx^2	d^2B_y/dy^2	d^2B_z/dz^2
1	-0.12	-0.08	-0.55	-0.08	0.06	0.03
2	-0.46	0.78	-0.58	-0.15	0.13	0.00
3	-0.29	-0.17	-0.64	-0.11	0.09	0.02
4	-0.15	-0.85	-0.52	-0.05	-0.03	0.02
5	-0.06	0.18	-0.53	-0.05	-0.03	0.00
6	1.03	-0.16	0.17	-0.38	0.46	0.07
7	0.59	-1.12	0.19	0.29	-0.35	-0.06
8	-0.09	0.57	-0.62	0.27	-0.09	-0.02
9	-0.21	0.25	-0.66	-0.30	0.26	0.03
10	0.43	-0.15	0.43	-0.10	0.16	0.06
11	0.31	0.03	1.70	-0.27	0.48	0.11
12	-0.10	-0.70	0.64	-0.12	0.16	0.15
13	0.02	-0.49	0.09	0.30	-0.44	0.02
14	0.27	0.15	-0.39	0.25	-0.29	-0.02
15	0.05	0.53	-0.34	-0.10	0.06	0.21
16	0.52	0.57	-0.20	-0.07	-0.03	0.00
17	-0.02	0.46	-0.05	-0.67	0.68	0.05

Table 9.5: Run 3 online cross scan results per probe: the first shimmed gradient of x, y, and z in a unit of Hz/mm and the second order shimmed gradient of x, y, and z in a unit of Hz/mm^2.

(z-direction) gradients' uncertainties as the shim gradient uncertainty. Second, the repeatability uncertainty is the uncertainty from the repeated trials with simulation tools using the same gradients. Lastly, coil length uncertainty is the uncertainty from the coil length measurement systematic errors. Coil lengths of each probe are shown in Table 9.1. I change the coil length in the simulation tool by 15 percent to see how much of a difference that makes. The results are shown in Table 9.7. The total uncertainties are calculated as

$$\sigma_{total} = \sqrt{(\delta gradient)^2 + (\delta repeatability)^2 + (\delta coil\text{-}length)^2}. \tag{9.5}$$

9.3 New Approach: Intrinsic Uncertainty Analysis

I will introduce the new approach to the intrinsic uncertainty of the azimuthally averaged field in this section.

	Run 2 [Hz]			Run 3 [Hz]		
Probe ID	Trolley	PP	Diff	Trolley	PP	Diff
1	10005.972	10008.159	-2.19	10000.830	10001.116	-0.29
2	10005.893	10007.602	-1.71	9999.929	9999.865	0.06
3	9999.246	9999.107	0.14	10000.372	10000.494	-0.12
4	9995.439	9993.694	1.74	10000.360	10000.540	-0.18
5	10015.327	10020.847	-5.52	10000.040	9999.923	0.12
6	10002.168	10003.023	-0.86	10001.905	10002.479	-0.57
7	10000.119	10000.165	-0.05	9998.437	9997.842	0.59
8	10000.122	10000.167	-0.05	9999.520	9999.345	0.17
9	10022.050	10029.875	-7.83	10000.668	10000.784	-0.12
10	9998.597	9998.098	0.50	10001.406	10002.041	-0.64
11	10003.665	10004.866	-1.20	10002.703	10003.936	-1.23
12	10008.942	10012.116	-3.17	10003.705	10005.039	-1.33
13	9994.476	9992.779	1.70	10000.394	10000.483	-0.09
14	10001.954	10002.671	-0.72	9999.574	9999.484	0.09
15	9994.993	9993.006	1.99	10005.078	10006.762	-1.68
16	9999.753	9999.596	0.16	10000.054	10000.006	0.05
17	10000.134	10000.172	-0.04	10001.300	10001.818	-0.52

Table 9.6: Run 2 and Run 3 Active volume difference results between the trolley and plunging probe.

9.3.1 Oversampling

There are about 9000 events in one trolley measurement. The length of the SR is about 45 m long, so each sample is 5 mm apart. Because the trolley extent is 15 mm, the trolley probe measures the same region multiple times. Fig 9.6 shows the visualization of the oversampling during trolley measurements. 1/weight means how many times the probe measures at the azimuthal position.

Intrinsic uncertainty $\epsilon = \overline{\omega} - \omega_C$ is defined to be probe accuracy for an event. However, in terms of the azimuthally averaged field in the whole ring region, the intrinsic uncertainty can not explain the systematic difference from the oversampling. In a sense, intrinsic uncertainty for the azimuthally averaged field should be the systematic difference from the oversampling.

Probe ID	$\Delta d^2B/dz^2$ [Hz]	Repeatability [Hz] Trolley	PP	Coil Length [Hz] Trolley	PP	Total Uncertainty
1	0.09	0.04	0.04	0.06	0.02	0.12
2	0.14	0.03	0.04	0.01	0.03	0.15
3	0.17	0.04	0.03	0.05	0.01	0.19
4	0.25	0.03	0.04	0.01	0.02	0.25
5	0.18	0.03	0.03	0.03	0.05	0.19
6	0.24	0.04	0.06	0.05	0.10	0.28
7	0.26	0.03	0.05	0.03	0.11	0.29
8	0.16	0.04	0.05	0.04	0.03	0.18
9	0.24	0.04	0.06	0.05	0.03	0.26
10	0.20	0.05	0.05	0.04	0.03	0.21
11	0.49	0.11	0.13	0.16	0.26	0.60
12	0.74	0.11	0.15	0.03	0.15	0.78
13	0.30	0.01	0.03	0.02	0.02	0.30
14	0.42	0.03	0.02	0.03	0.04	0.43
15	0.53	0.12	0.20	0.06	0.14	0.60
16	0.29	0.01	0.02	0.02	0.02	0.29
17	0.68	0.04	0.04	0.01	0.07	0.69

Table 9.7: The table included shim gradient uncertainty, repeatability uncertainty, and coil length systematic uncertainty in units of Hz.

9.3.2 Intrinsic Uncertainty for the averaged field of the ring

The azimuthally averaged field is defined as

$$\langle f \rangle = \frac{1}{2\pi} \int_0^{2\pi} f(\varphi) d\varphi. \tag{9.6}$$

The measurement of one event i is the average field of the probe extent is driven from Equation 9.2 and is expressed as

$$\overline{\omega}_i = \int_0^{2\pi} f(\varphi) S_i(\varphi) d\varphi. \tag{9.7}$$

Because there is oversampling, the average of all events is not the correct way to express it. Indeed, the azimuthal average around the ring is as:

$$\langle \omega_{\text{meas}} \rangle = \sum_i^n \overline{\omega}_i \cdot \Psi_i = \sum_i^n \int_0^{2\pi} f(\varphi) S_i(\varphi) d\varphi \cdot \Psi_i, \tag{9.8}$$

where Ψ_i is the weight of event i and n is approximately 9000. The *averaging bias* η is the difference between the azimuthal averaged field and the azimuthal averaged field of measurements which is

$$\eta = \langle f \rangle - \langle \omega_{\text{meas}} \rangle = \frac{1}{2\pi} \int_0^{2\pi} f(\varphi) d\varphi - \sum_0^n \overline{\omega}_i \cdot \Psi_i. \tag{9.9}$$

In the standard ω_p analysis chain, $2\Psi_i$ is defined as $\Delta\varphi_i$ where the distance is apart between the two nearest samples.

9.3.2.1 Framework Verification with Data

It is extremely crucial to verify the framework with real trolley measurements so that there are no numerical and other possible errors. Equation 9.7 can be rewritten as

$$f_{\varphi_i}^{\text{meas}} = \int_0^{2\pi} f(\varphi_i + \vartheta)\, \omega(\vartheta)\, d\vartheta = \int_0^{2\pi} f(\varphi)\, \omega(\varphi - \varphi_i)\, d\varphi = \int_0^{2\pi} f(\varphi)\, \omega_i(\varphi)\, d\varphi, \tag{9.10}$$

assuming $\omega(\vartheta)$ is anyways 0 outside $\vartheta_{\text{probe}}/2$ and $\omega_i(\varphi) = \omega(\varphi - \varphi_i)$. Then, in this case, Equation 9.6 can be rewritten as

$$\begin{aligned}
\langle f \rangle_{\text{azi}} &= \frac{1}{2\pi} \int_0^{2\pi} f(\varphi) \left[\frac{\sum_i \omega_i(\varphi)}{\sum_i \omega_i(\varphi)} \right] d\varphi \\
&= \frac{1}{2\pi} \int_0^{2\pi} \left[\frac{\sum_i f(\varphi)\omega_i(\varphi)}{\sum_i \omega_i(\varphi)} \right] d\varphi \\
&= \frac{1}{2\pi} \int_0^{2\pi} \sum_i f(\varphi)\omega_i(\varphi)\Omega(\varphi)\, d\varphi \\
&= \frac{1}{2\pi} \sum_i \int_0^{2\pi} f(\varphi)\omega_i(\varphi)\Omega(\varphi)\, d\varphi,
\end{aligned} \tag{9.11}$$

where $\Omega(\varphi) = 1/\sum_i \omega_i(\varphi)$. Assigning a weight Ψ_i to each measurement (traditionally we use $\Psi_i = \Delta\varphi_i/(2\pi)$) allows us to relate $\sum f_{\varphi_i}^{\text{meas}} \Psi_i$ to $\langle f \rangle_{\text{azi}}$. We can enforce $\sum f_{\varphi_i}^{\text{meas}} \Psi_i = \langle f \rangle_{\text{azi}}$ for each measurement i and calculate the corresponding weights

Run Number	Naive (HZ)	$\Psi_i = \Delta\varphi_i$ (Hz)	$\Psi_i'(Hz)$
7215	15.134	0.012	0.000
7293	91.970	0.003	0.000
7468	35.739	0.016	0.000
7608	62.514	0.005	0.000
7638	40.779	0.005	0.000
7842	7.753	-0.005	0.000

Table 9.8: Verification of the Framework. Naive results do not use any weight. Ψ_i is the traditional weight that is used for production. Ψ_i' is the new weight for the test.

Ψ_i that helps us to fulfill this:

$$\Psi_i = \frac{\int_0^{2\pi} f(\varphi)\omega_i(\varphi)\Omega_(\varphi)d\varphi}{\int_0^{2\pi} f(\varphi)\omega_i(\varphi)d\varphi} = \frac{\int_0^{2\pi} f(\varphi)\omega_i(\varphi)\Omega_(\varphi)d\varphi}{f_{\varphi_i}^{\text{meas}}}. \tag{9.12}$$

In order to verify that the framework is valid, η should be zero value when new weight Ψ_i' is used to Equation 9.9.

I use the Fourier Fit to a real field map as a truth field, $f(\varphi)$. Fig 9.7 shows both raw and Fourier fit plots of Run 7070. Using the truth field, $f(\varphi)$, and different weights, we can evaluate different η for each weight. The new weight Ψ_i expects η to be zero. The result is shown in table 9.8.

I use multiple trolley runs from the Run 2 Dataset in Appendix A, Table A.1. Naive results mean that there is no weight used for the test and treat it as the constant is uniform. Ψ_i is the traditional weight that is used for production. Finally, Ψ_i' is a new weight that I want to test the software framework. As shown in Table 9.8, for every run, η is zero when I use a new weight, Ψ_i'. It shows that the framework has no numerical errors.

9.3.2.2 Result

The result and comparison between Run 1 and the new proposed intrinsic uncertainty are shown in Table 9.9. For intrinsic uncertainty, ϵ, the mean and standard deviation are evaluated from Table 9.3. For intrinsic uncertainty, η, the mean and standard

	Previous Intrinsic Unc (ϵ) [Hz]	New Intrinsic Unc (η) [Hz]
mean	-0.0064	0.0032
std	0.0097	0.0092

Table 9.9: Mean and standard deviation of the previous and new intrinsic uncertainties in a unit of Hz.

deviation are calculated from the Purcell Dataset of the whole Run 2 trolley runs, which is 28 runs. Purcell Interpolation details can be found in the document [91]. The difference between the two intrinsic uncertainty is small, 0.0032 Hz or 0.05 ppb, which is expected because intrinsic uncertainty is such a small systematic difference.

9.3.3 Comparison between Two Intrinsic Uncertainty

Run 1 intrinsic uncertainty, ϵ, is evaluated from the simulation with a known local gradient for each event. It means that we cannot evaluate ϵ if we do not know the local gradient. Unfortunately, finding the precise local gradients of 17 probes is not easy from trolley measurements. However, new intrinsic uncertainty does not need local gradients for each sample because we use a global gradient as a whole ring.

The simulation takes about 30 seconds per sample. There are 9000 events with 17 probes in general for one trolley run. Then, it will take about 1280 hours per trolley run. There are 28 trolley runs in the Run 2 Dataset, which needs 35840 hours or 1494 days to complete the simulation. The computing time is not realistic. On the other hand, the oversampling method only takes a few minutes for one run, so it will take about 30 minutes to 1 hour to complete all Run 2 Dataset.

9.4 Conclusion

Prior to the work described in this dissertation, the collaborator had constructed an outstanding and effective NMR FID analysis framework. He focused on two systematic uncertainties: one related to the fit, the other being intrinsic. The fit uncertainty is a systematic difference from the true value arising in the FID frequency extrac-

tion. The intrinsic uncertainty reflects a systematic difference arising from the probe geometry and field map. These uncertainties explain the systematic difference on a single-event basis. However, the experiment's overall analysis requires the systematic uncertainty of the azimuthally averaged field around the entire ring. As the event or sample spacing is smaller than the probe's extent in length, there are regions where the trolley measures multiple times, leading to oversampling. Because each event spaces differently, each event has different numbers of overlaps, which are defined to be weight.

Because of the oversampling, there is a systematic shift, and the intrinsic uncertainty must reflect this shift. The result of the new approach of intrinsic uncertainty for the Run 2 Dataset is a 0.05 ppb difference from Run 1 intrinsic uncertainty of Run 1. The difference is indeed small, as expected.

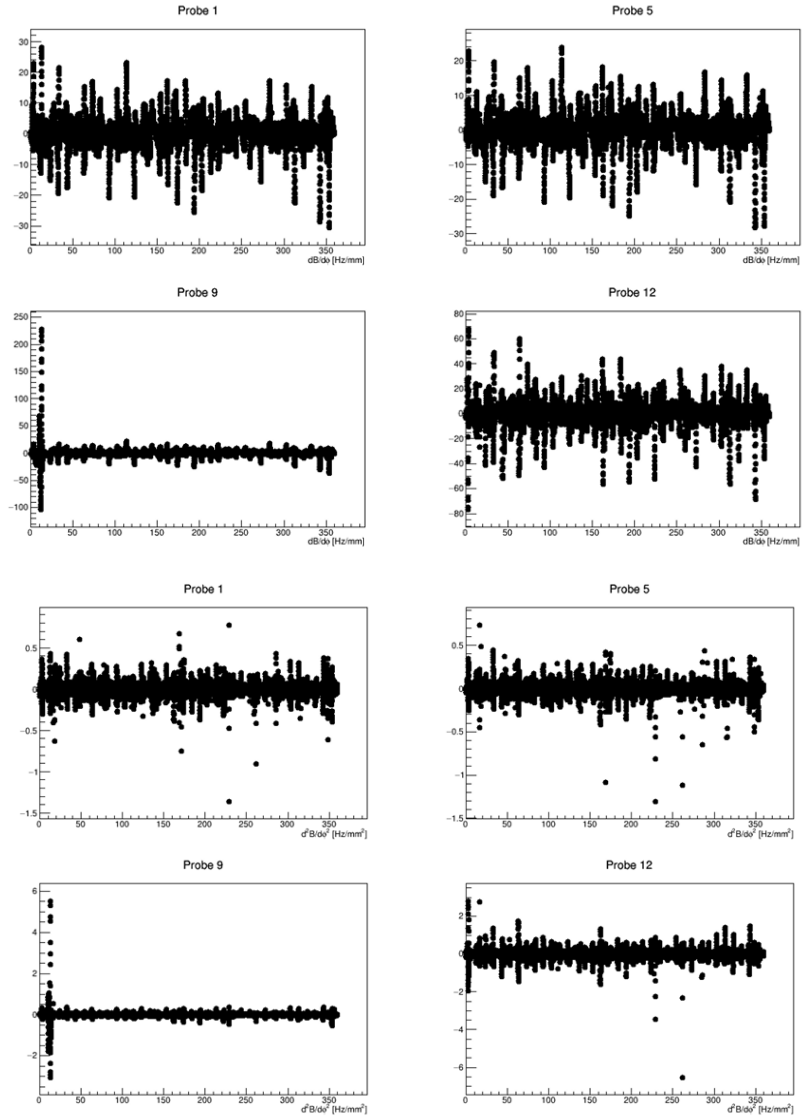

FIGURE 9.3: Top: First gradient dB/dz as function of trolley position; x-axis unit is degree and y-axis unit is Hz/mm. Bottom: Second gradient d^2B/dz^2 as a function of trolley position; x-axis unit is degree and y-axis unit is Hz/mm^2. Plots are from the reference Figure 39 and 40 [83]

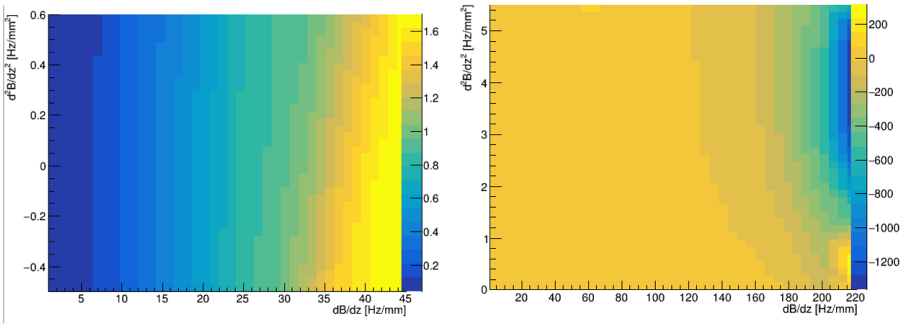

FIGURE 9.4: Scan of the fit accuracy in a different field from the note [83].

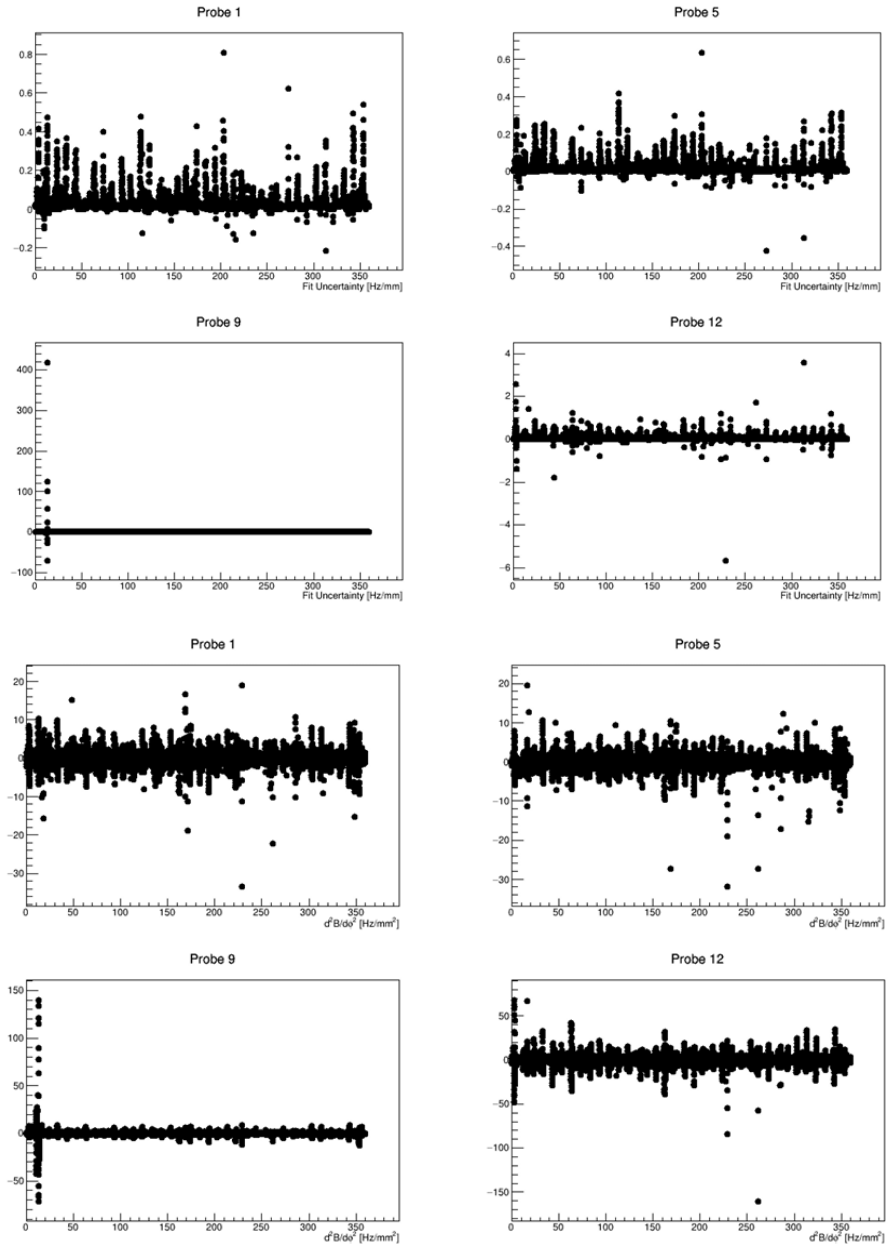

FIGURE 9.5: Top: fit uncertainty δ as a function of trolley position: x-axis is azimuthal positions in a unit of degrees and y-axis is fit uncertainties in a unit of Hz/mm. Bottom: intrinsic uncertainty ϵ as a function of trolley position: x-axis is azimuthal positions in a unit of degrees and y-axis is fit uncertainties in a unit of Hz/mm^2. Plots are reproduced from the note [83].

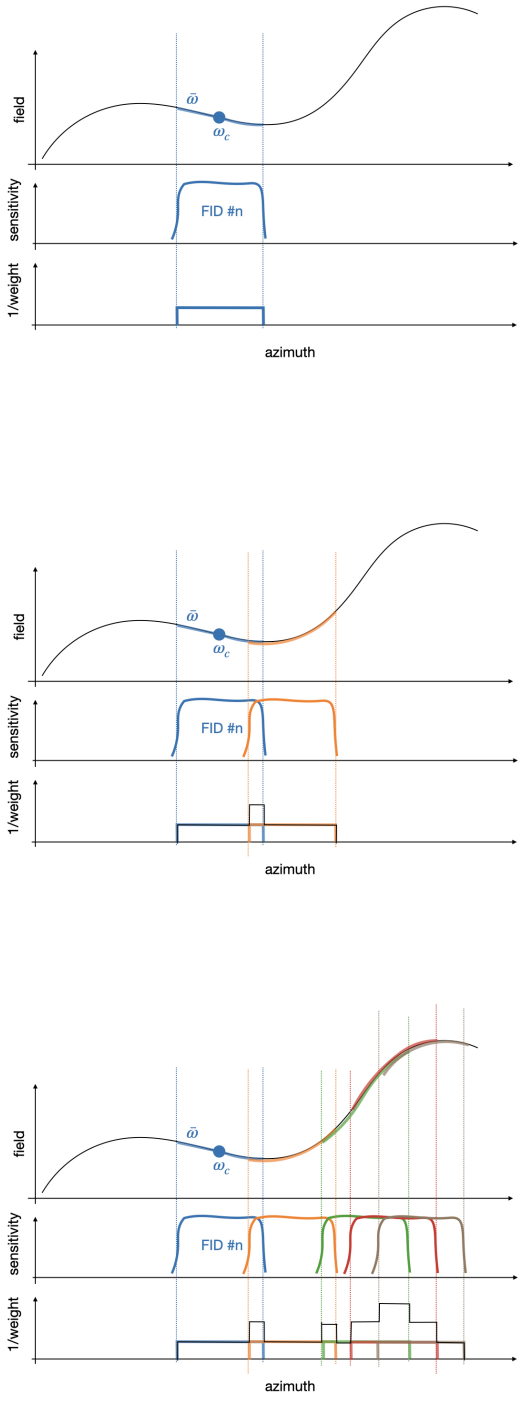

FIGURE 9.6: visualization of the oversampling during real measurement.

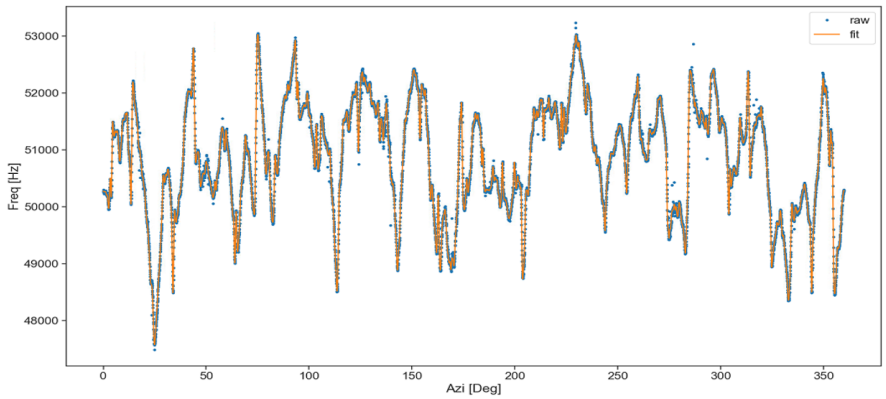

FIGURE 9.7: : Trolley Run [7070]. Blue is the raw data plot and orange is the Fourier Fit of the blue plot (order of 500).

10

Conclusion and Outlook

10.1 Conclusion

The BNL E821 Muon g-2 experiment measured the anomalous magnetic moment of the muon, a_μ, to a relative uncertainty of 0.54 ppm. The measured value corresponds to a discrepancy of between 3.5 and 3.7 standard deviations from the SM theoretical prediction. For the effect to be reliably established, a minimum of 5 or more standard deviation discrepancy is needed. To prove this premise, a new experiment based on the same approach as the BNL E821 has been undertaken with a greater precision goal. The Fermilab E989 muon g-2 experiment aims to measure a_μ with a precision of 140 ppb. I joined the E989 experiment field team in 2018 and mainly focused on studying the systematics of NMR techniques and probes. The objective of this work is to implement my studies of the NMR techniques and probes and to demonstrate the advancement and improvement of the field measurements, which are directly connected to the calculation of a_μ. Several methods and data-driven computational models are produced to analyze the FID frequency extractions using all of the relevant NMR probes in the experiment: fixed probes, trolley probes, and

plunging probes. The method presented here focuses on the optimization of parameters, calibration of the field measurements, and steps necessary to reduce the related systematic uncertainties in a holistic approach.

Chapter 2 covered the theoretical efforts aimed to calculate the value of a_μ to extreme precision. Chapter 3 introduced the overview of the E989 experiment. The experiment was done by counting the number of decay positrons observed in the electromagnetic caloimeters above an energy threshold, while the NMR probes in and around the muon SR measured the magnetic field of the muon storage region. Straw trackers assisted both measurements by measuring the muon beam dynamics that directly impact both the precession frequency measurement, ω_a, and the distribution of muons within the measured magnetic field. Chapter 4 and Chapter 5 described the magnetic field measurement system and the NMR techniques that the field team used to measure the magnetic field of the SR. More mechanisms and methods details of each probe (fixed probes, trolley probes, plunging probes in order) are introduced in Chapter 6, Chapter 7, and Chapter 8. Lastly, Chapter 9 described the field measurement systematics.

My contributions to the experiment are on the magnetic field measurement analysis. The first step of the magnetic field measurement analysis is to calibrate trolley NMR probes with a dedicated calibration probe, the plunging probe. One of the primary goals of my work was the calibration analysis. I performed a careful cross-check of the Run 2 and 3 calibrations[89] with my own independently developed analysis approach. I introduced certain new uncertainty studies that were not included in the previous calibration analysis, such as new FID extraction uncertainty, active volume correction, and 3D repeatability position uncertainty. I will be the primary analyzer for Run 4 and beyond calibration analysis and another collaborator will be the secondary analyzer to cross-check my results. My pre-Run 4 calibration results are shown in Section 7.2.6 and the difference between pre-Run 4 and Run 3 calibration

results is 6.1 ppb.

Besides working on the trolley calibration analysis, I have also analyzed the plunging probe FID extraction. There are two major methods to extract the plunging probe FID: the Hilbert method and UMass (zero-crossing) method. I studied the differences between the two methods. In addition, I studied how much effect the extracted frequencies are in a very well-shimmed field depending on analysis choices of the frequency extraction algorithm, such as fit window length and polynomial order. The uncertainty associated with the plunging probe frequency extraction result is shown in Table 8.2. This is a sub-ppb effect for the dipole and a max 2 ppb effect for higher-order moments.

The analysis step following the trolley calibration is the fixed probe mapping. The fixed probe field moments are synchronized to the trolley field moments. There are a total of 378 fixed probes mounted around the ring to monitor the field drift. However, not all fixed probes have good FIDs. I came out with a new algorithm to improve the fixed probe measurement resolutions, especially for probes with short FIDs. I implemented the new algorithm to the production campaign, so each production file contains new extracted fixed probe frequencies.

Lastly, I worked on field measurement systematics. I introduced a new approach called oversampling to find the systematic uncertainty of the azimuthally averaged field of the ring. The uncertainty from the new approach is shown in Table 9.9, which is 0.05 ppb difference from Run 1 intrinsic uncertainty.

10.2 Outlook

At the time of this writing, the Muon g-2 collaboration is finalizing Run 2 and Run 3 publications which aim to be completed in summer 2023. Five data-taking periods, Run 1, Run 2, Run 3, Run 4, and Run 5 have been completed, while Run-6 data-taking is currently underway. Including Run 5 data, the total recorded dataset

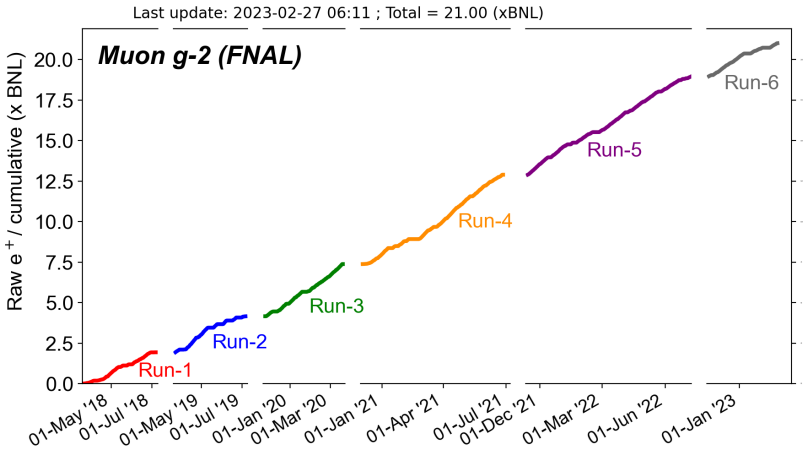

FIGURE 10.1: The fraction of BNL statistics recorded overtime during the run 6.

contains 17.5 times the number of events compared to BNL E821; with the data collected in Run 6 to date, the stated E989 goal of 21 times BNL E821 has been exceeded. The plot of the BNL fraction statistics was recorded over time during the run shown in Fig 10.1. The first result is only 6 % of the total expected data so there is much more data to analyze. With the data acquired since Run 1, given the improvements and upgrades of the $\tilde{\omega}_p^{'}$ measurement hardware and software, and with my contributions, such as the precise analysis of calibration constant, NMR frequency extraction uncertainties for NMR probes, and field measurement systematics, the uncertainties in the determination of the magnetic field are being further reduced. This is an integral contribution, one of many needed to achieve the error budget of 70 ppb in the final result.

Appendix A

Dataset Definitions

Table A.1: Run 2 Dataset Overview [Run numbers] 2018 2019

Run 2	Sub-Run	Trolley Pair	Fixed Probe Runs	Template Run
2A	1	(6627, 6676)	6630 6672	6651
2B	1	(6777, 6843)	6780 6837	6965
	2	(6843, 6880)	6845 6877	
2C	1	(6880, 6937)	6883 6934	
	2	(6937, 6988+6989)	6946 6985	
	3	(6988+6989, 7032)	6992 7029	
	4	(7032, 7070)	7036 7065	
2D	1	(7078, 7107)	7082 7104	7168
	2	(7107, 7152)	7124 7149	
	3	(7152, 7188)	7155 7185	
	4	(7188, 7215)	7191 7212	
	5	(7215, 7251+7253)	7218 7248	
	6	(7251+7253, 7293)	7256 7290	
2E	1	(7392, 7432)	7396 7427	7420
	2	(7432, 7468)	7435 7465	
2F	1	(7477, 7514)	7480 7511	7530
	2	(7514, 7549)	7521 7546	
2G	1	(7608, 7638)	7611 7635	7623
2H	1	(7675, 7699)	7678 7696	7687
2I	1	(7842, 7876)	7845 7873	7859

Table A.2: Run 3 Dataset Overview [Run numbers] 2019 2020

Run 3	Sub-Run	Trolley Pair	Fixed Probe Runs	Template Run
3B	1	(8711, 8747)	8715 8741	8771
	2	(8747, 8796)	8750 8793	
	3	(8796, 8846)	8799 8826	
3C	1	(8908, 8948)	8911 8945	8928
3D	1	(8955, 8996)	8959 8993	9080
	2	(8996, 9030)	8999 9027	
	3	(9030, 9070)	9033 9067	
	4	(9070, 9091)	9073 9088	
	5	(9163, 9200)	9166 9197	
3E	1	(9200, 9235)	9203 9232	
	2	(9235, 9271)	9238 9269	
	3	(9271, 9314)	9274 9311	
3F	1	(9321, 9359)	9324 - 9356	9340
3G	1	(9368, 9407)	9372 9404	9412
	2	(9407, 9453)	9410 9450	
3J	1	(9631, 9656)	9634 9653	9668
	2	(9656, 9680)	9659 9677	
	3	(9680, 9702)	9683 9699	
3L	1	(9769, 9800)	9772 9797	9784
3M	1	(9811, 9847)	9815 9843	10020
	2	(9847, 9886)	9850 9883	
	3	(9886, 9928)	9889 9925	
3N	1	(9928, 9963)	9931 9960	
	2	(9963, 10005)	9966 10001	
	3	(10005, 10036)	10008 10033	
	4	(10036, 10072)	10039 10069	
	5	(10072, 10096)	10075 10093	
3O	1	(10106, 10148)	10110 10144	10171
	2	(10148, 10191)	10153 10188	
	3	(10191, 10225)	10194 10222	

Appendix B

New Fit Window for Fixed Probe

Table B.1: The new fit windows for all bad fixed probes. The table contains the original fit window [μs] as (start, end) and the new fit window as (start, end). Also, the table includes the standard deviation [Hz] of the old and new fit windows of Run 10220.

Probe	Old fit window	New fit window	Std (Hz, before)	New Std(Hz, after)
3	(511 , 576)	(576 , 605)	72.76	8.06
4	(508 , 577)	(577 , 560)	45.11	10.14
5	(504 , 555)	(555 , 550)	72.47	9.99
9	(506 , 580)	(580 , 540)	18.83	8.82
15	(518 , 608)	(608 , 620)	120.65	12.65
16	(498 , 520)	(520 , 505)	407.72	25.34
17	(509 , 530)	(530 , 510)	569.01	23.04
21	(495 , 549)	(549 , 520)	73.94	32.25
22	(499 , 559)	(559 , 565)	175.08	12.50
23	(508 , 593)	(593 , 605)	107.12	9.40
27	(495 , 569)	(569 , 565)	31.19	3.77
28	(499 , 557)	(557 , 539)	21.69	5.26
33	(505 , 541)	(541 , 515)	116.43	12.94
34	(507 , 575)	(575 , 544)	28.76	8.80
35	(509 , 562)	(562 , 535)	258.82	9.63
43	(509 , 709)	(709 , 620)	29.76	12.83
71	(514 , 642)	(642 , 642)	11.98	3.92
74	(510 , 693)	(693 , 695)	27.03	2.96
75	(510 , 534)	(534 , 540)	76.16	9.80
91	(505 , 738)	(738 , 719)	25.95	4.32
124	(503 , 562)	(562 , 544)	21.03	4.73
181	(501 , 894)	(894 , 894)	11.51	9.84
182	(513 , 544)	(544 , 520)	54.35	5.16
192	(505 , 812)	(812 , 812)	16.49	4.30
194	(513 , 682)	(682 , 682)	10.74	2.45
217	(502 , 1014)	(1014 , 915)	26.00	0.73
221	(507 , 687)	(687 , 700)	17.19	4.90
232	(516 , 585)	(585 , 563)	19.50	4.75
257	(512 , 569)	(569 , 530)	36.93	7.73
328	(516 , 889)	(889 , 871)	12.06	7.98
329	(518 , 792)	(792 , 774)	17.39	7.96
330	(503 , 563)	(563 , 544)	15.60	5.28
341	(504 , 939)	(939 , 635)	15.03	3.68
342	(506 , 624)	(624 , 540)	17.54	4.56
371	(511 , 780)	(780 , 780)	10.44	7.81
372	(505 , 566)	(566 , 548)	13.18	4.28

Appendix C

Run 3 Plunging Probe FID and Frequency Extraction Plots

C.1 Run 3 Plunging Probe FID Plots during Rapid Swapping

C.2 Run 3 Plunging Probe Plot: Frequency Extraction as Function of Fit Length

C.3 Run 3 Plunging Probe Plot: Frequency Extraction as Function of Polynomial Order

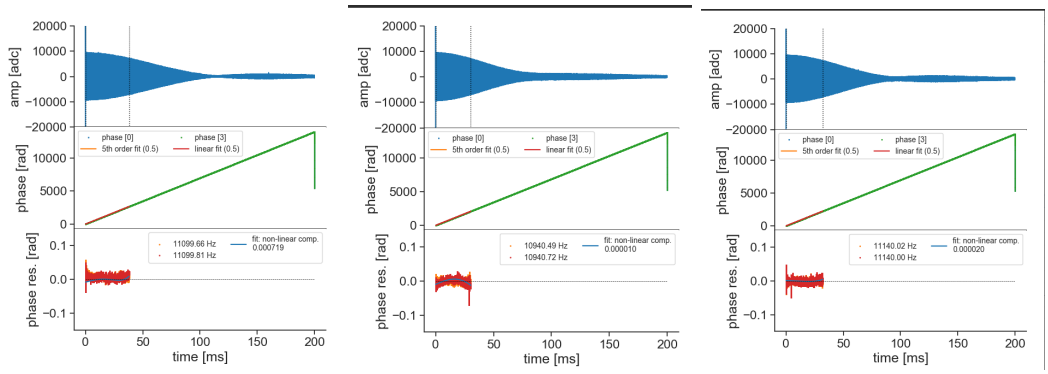

FIGURE C.1: Rapid Swap: probe 1, 2, 3

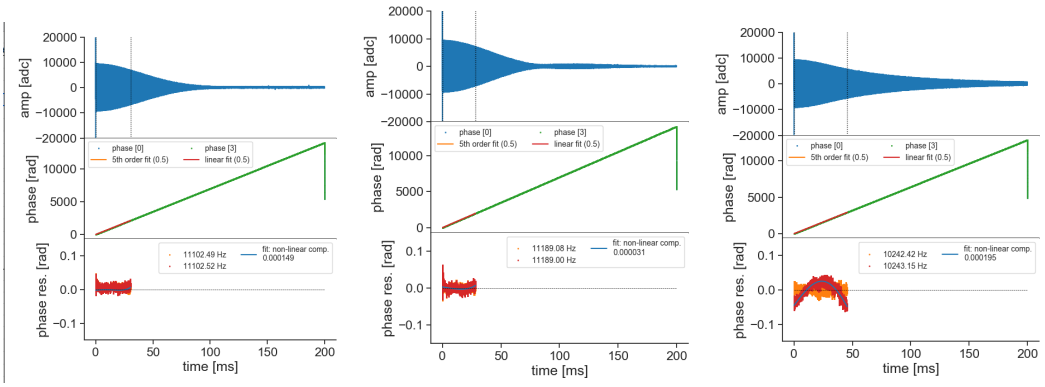

FIGURE C.2: Rapid Swap: probe 4, 5, 6

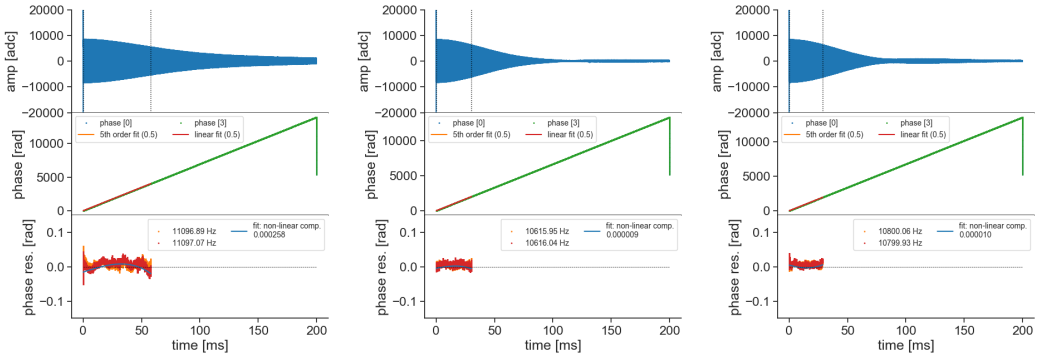

FIGURE C.3: Rapid Swap: probe 7, 8, 9

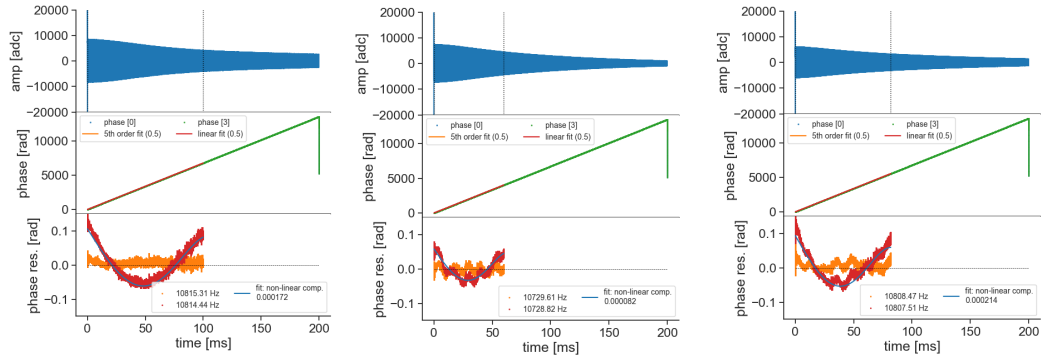

FIGURE C.4: Rapid Swap: probe 10, 11, 12

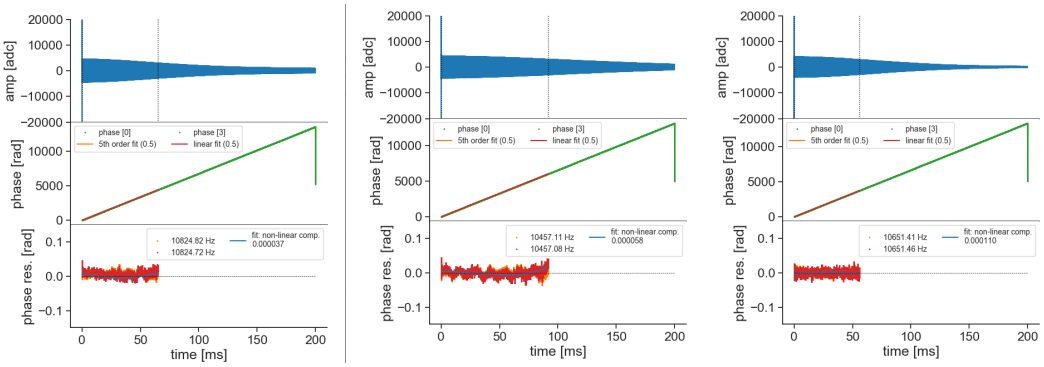

FIGURE C.5: Rapid Swap: probe 13, 14, 15

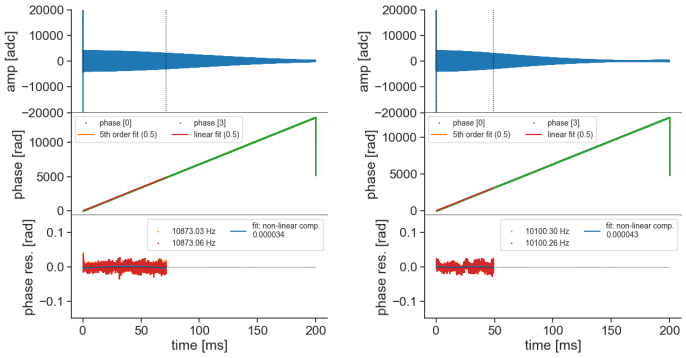

FIGURE C.6: Rapid Swap: probe 16, 17

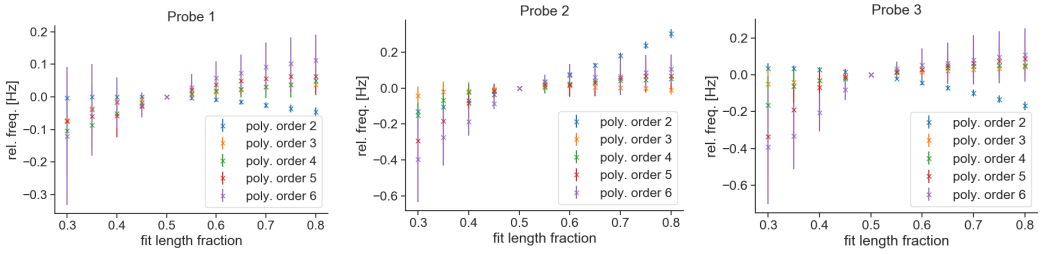

FIGURE C.7: Rapid Swap: probe 1, 2, 3

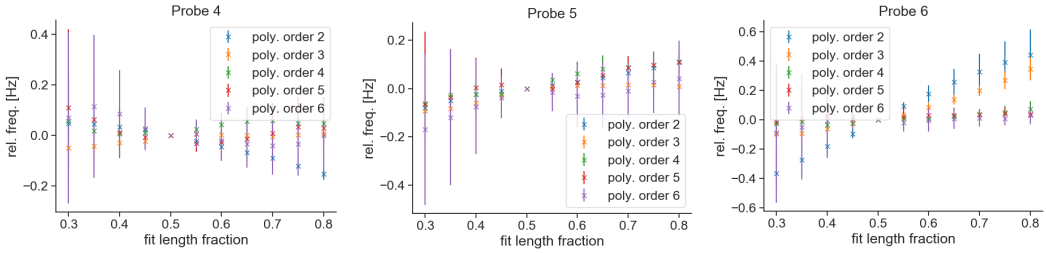

FIGURE C.8: Rapid Swap: probe 4, 5, 6

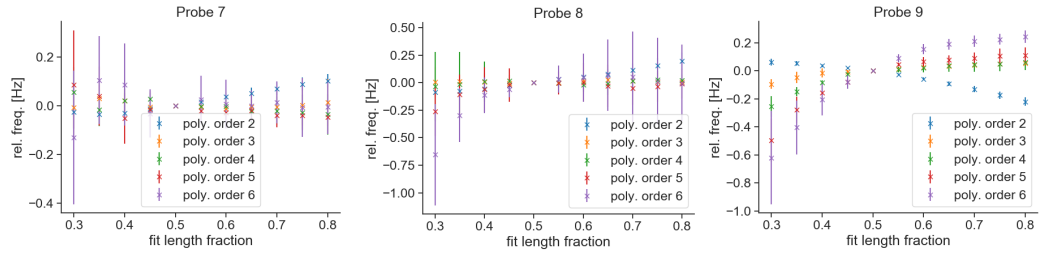

FIGURE C.9: Rapid Swap: probe 7, 8, 9

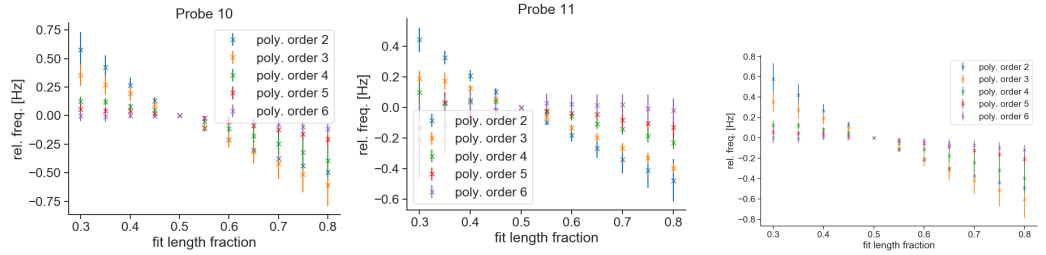

FIGURE C.10: Rapid Swap: probe 10, 11, 12

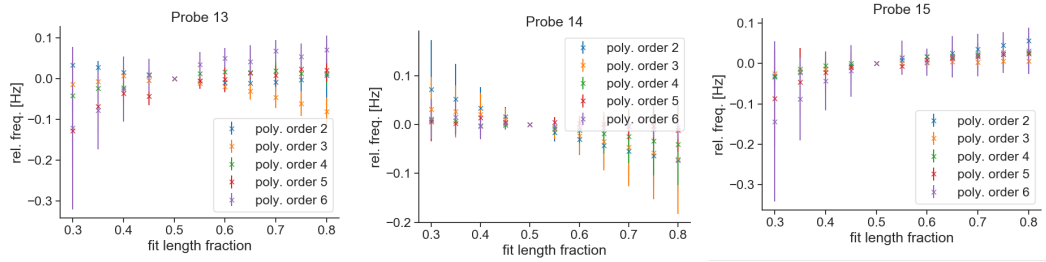

FIGURE C.11: Rapid Swap: probe 13, 14, 15

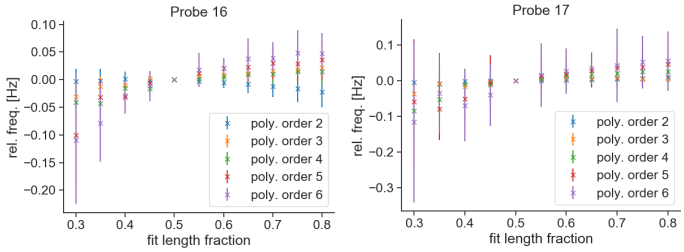

FIGURE C.12: Rapid Swap: probe 16, 17

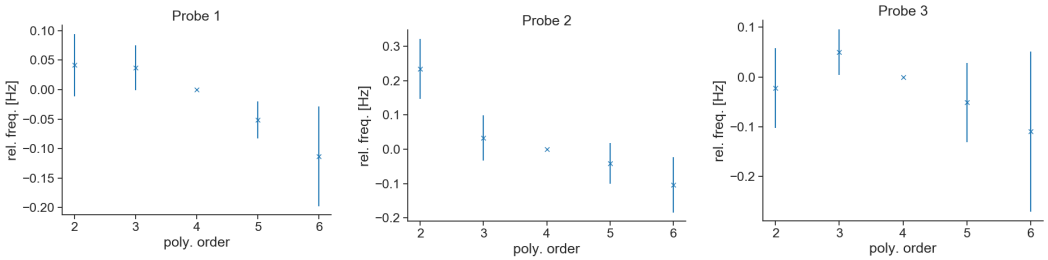

FIGURE C.13: Rapid Swap: probe 1, 2, 3

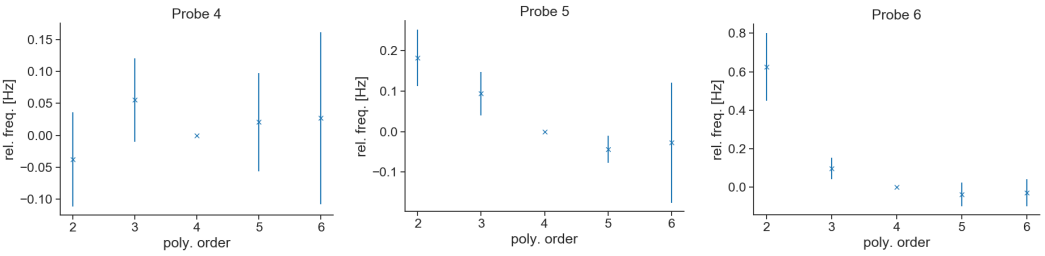

FIGURE C.14: Rapid Swap: probe 4, 5, 6

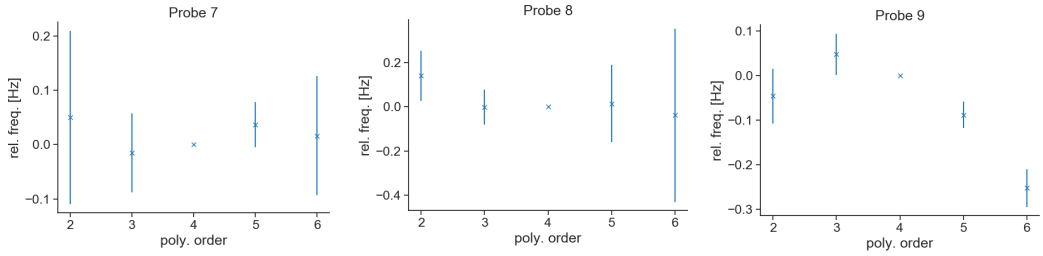

FIGURE C.15: Rapid Swap: probe 7, 8, 9

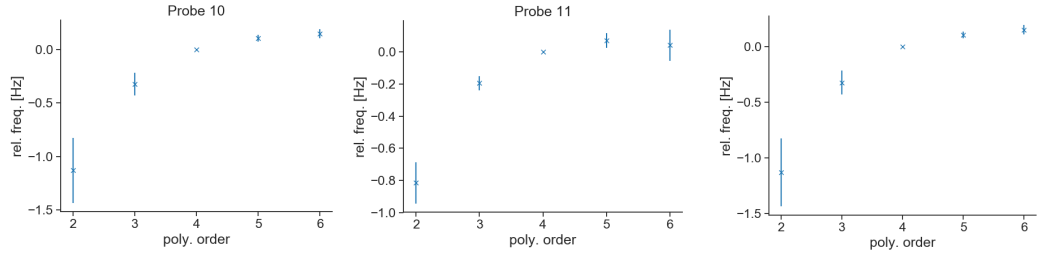

FIGURE C.16: Rapid Swap: probe 10, 11, 12

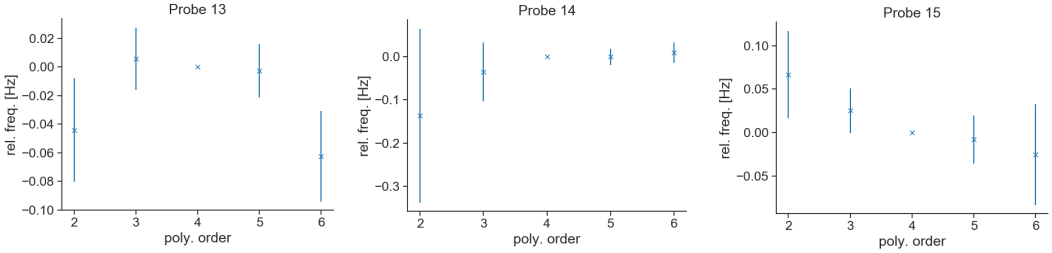

FIGURE C.17: Rapid Swap: probe 13, 14, 15

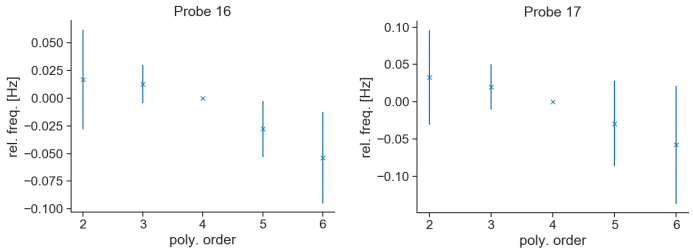

FIGURE C.18: Rapid Swap: probe 16, 17

Bibliography

[1] J. P. Miller, E. Rafael, and B. L. Roberts. Muon (g-2): Experiment and Theory. *IOP Science*, 70, 2007.

[2] P. Kusch, and H. M. Foley. The Magnetic Moment of the Electron. *Phys. Rev.*, 74:250–263, Aug 1948.

[3] B. Odom, D. Hanneke, B. D'Urso, and G. Gabrielse. New Measurement of the Electron Magnetic Moment Using a One-Electron Quantum Cyclotron. *Phys. Rev. Lett.*, 97:030801, Jul 2006.

[4] D. Hanneke, S. Fogwell, and G. Gabrielse. New Measurement of the Electron Magnetic Moment and the Fine Structure Constant. *Phys. Rev. Lett.*, 100:120801, Mar 2008.

[5] X. Fan, T. G. Myers, B. A. Sukra, and G. Gabrielse. Measurement of the Electron Magnetic Moment. *Phys. Rev. Lett.*, 130:071801, Feb 2023.

[6] T. Aoyama, M. Hayakawa, T. Kinoshita,and M. Nio. Complete Tenth-Order QED Contribution to the Muon $g-2$. *Phys. Rev. Lett.*, 109:111808, Sep 2012.

[7] T. Aoyama, and et al. (Muon g-2 Theory Initiative). The Anomalous Magnetic Moment of the Muon in the Standard Model. *Physics Reports*, 887:1–166, 2020.

[8] G. Charpak, and et al. A New Measurement of the Anomalous Magnetic Moment of the Muon. *Physics Letters*, 1(1):16–20, April 1962.

[9] J. Bailey, and et al. Precision Measurement of the Anomalous Magnetic Moment of the Muon. *Phys. Lett. B*, 28:287–290, 1968.

[10] J. Bailey, and et al. Final Report on the CERN Muon Storage Ring including the Anomalous Magnetic Moment and the Electric Dipole Moment of the Muon, and a Direct Test of Relativistic Time Dilation. *Nuclear Physics B*, 150:1–75, 1979.

[11] G. W. Bennett, and et al. (Muon g-2 collaboration). Final Report of the Muon E821 Anomalous Magnetic Moment Measurement at BNL. *Phys. Rev. D*, 73:072003, 2006.

[12] B. Abi, and et al. (Muon g-2 collaboration). Measurement of the Positive Muon Anomalous Magnetic Moment to 0.46 ppm. *Phys. Rev. Lett.*, 126:141801, Apr 2021.

[13] B. Abi, and et al. (Muon g-2 collaboration). Magnetic-field Measurement and Analysis for the Muon g-2 Experiment at Fermilab. *Phys. Rev. A*, 103:042208, Apr 2021.

[14] A. Keshavarzi, K. S. Khaw, and T. Yoshioka. Muon g-2: A review. *Nuclear Physics B, ISSN-0550-3213*, 975, 2022.

[15] J. Grange, and et al. Muon (g-2) Technical Design Report, 2018.

[16] S. Corrodi. Purcell Analysis Technical Report. *Muon g-2 Internal DocDB*, 27375, 2022.

[17] S. Charity. Bloch Analysis Technical Report. *Muon g-2 Internal DocDB*, 27000, 2022.

[18] S. Corrodi, and et al. E989 Note 294: Run 2/3 Field Documentation: Review. *Muon g-2 Internal DocDB*, 28082, 2022.

[19] C. Gnendiger, D. Stockinger, and H. Kim. The Electroweak Contributions to $(g-2)_\mu$ after the Higgs-boson Mass Measurement. *Phys. Rev. D*, 88:053005, Sep 2013.

[20] S. Bodenstein, C. A. Dominguez, K. Schilcher, and H. Spiesberger. Hadronic Contribution to the Muon g-2 Factor. *Physical Review D*, 88(1), jul 2013.

[21] A. Keshavarzi, D. Nomura, and T. Teubner. $g-2$ of Charged Leptons, $\alpha(M_Z^2)$, and the Hyperfine Splitting of Muonium. *Phys. Rev. D*, 101:014029, Jan 2020.

[22] A. Kurz, T. Liu, P. Marquard, and M. Steinhauser. Hadronic Contribution to the Muon Anomalous Magnetic Moment to Next-to-Next-to-Leading Order. *Physics Letters B*, 734:144–147, 2014.

[23] A. Keshavarzi, D. Nomura, and T. Teubner. Muon $g-2$ and $\alpha(M_Z^2)$: A New Data-Based Analysis. *Phys. Rev. D*, 97:114025, Jun 2018.

[24] F. V. Ignatov, and et al. Measurement of the $e^+e^- \to \pi^+\pi^-$ Cross Section from Threshold to 1.2 GeV with the CMD-3 Detector. 2 2023.

[25] C. Aubin, T. Blum, C. Tu, M. Golterman, C. Jung, and S. Peris. Light quark Vacuum Polarization at the Physical Point and Contribution to the Muon $g-2$. *Phys. Rev. D*, 101:014503, Jan 2020.

[26] P. Joaquim, R. Eduardo, and V. Arkady . *The Hadronic Light-by-Light Scattering Contribution to the Muon and Electron Anomalous Magnetic Moments*, pages 303–317.

[27] A. Nyffeler. Hadronic Light-by-Light Scattering in the Muon $g-2$: A New Short-distance Constraint on Pion Exchange. *Phys. Rev. D*, 79:073012, Apr 2009.

[28] F. Jegerlehner, and A. Nyffeler. The Muon g-2. *Physics Reports*, 477(1):1–110, 2009.

[29] F. Jegerlehner. *The Anomalous Magnetic Moment of the Muon*. Springer, 2008.

[30] C. Lehner, and A.S. Meyer. Consistency of Hadronic Vacuum Polarization between Lattice QCD and the R ratio. *Phys. Rev. D*, 101:074515, Apr 2020.

[31] Sz. Borsanyi, and et al. Leading Hadronic Contribution to the Muon Magnetic Moment from lattice QCD. *Nature*, 593, May 2021.

[32] D. Giusti, F. Sanfilippo, and S. Simula. Light-quark Contribution to the Leading Hadronic Vacuum Polarization term of the Muon $g-2$ from Twisted-mass Fermions. *Phys. Rev. D*, 98:114504, Dec 2018.

[33] D. Giusti, V. Lubicz, G. Martinelli, F. Sanfilippo, and S.Simula. Electromagnetic and Strong Isospin-Breaking Corrections to the Muon $g-2$ from Lattice QCD + QED. *Phys. Rev. D*, 99:114502, Jun 2019.

[34] G. Antoine, and et al. Leading Hadronic Contribution to $(g-2)_\mu$ from Lattice QCD with $N_\mathrm{f} = 2+1$ Flavors of O(a) Improved Wilson Quarks. *Phys. Rev. D*, 100:014510, Jul 2019.

[35] C. Davies, and et al. Hadronic-Vacuum-Polarization Contribution to the Muon's Anomalous Magnetic Moment from Four-Flavor Lattice QCD. *Phys. Rev. D*, 101:034512, Feb 2020.

[36] B. Chakraborty, and et al. Strong-Isospin-Breaking Correction to the Muon Anomalous Magnetic Moment from Lattice QCD at the Physical Point. *Phys. Rev. Lett.*, 120:152001, Apr 2018.

[37] E. Shintani, and Y. Kuramashi. Hadronic Vacuum Polarization Contribution to the Muon $g-2$ with $(2+1)$-flavor Lattice QCD on a Larger than $(10\ \text{fm})^4$ Lattice at the Physical Point. *Phys. Rev. D*, 100:034517, Aug 2019.

[38] T. Blum, and et al. Calculation of the Hadronic Vacuum Polarization Contribution to the Muon Anomalous Magnetic Moment. *Phys. Rev. Lett.*, 121:022003, Jul 2018.

[39] Sz. Borsanyi, and et al. Hadronic Vacuum Polarization Contribution to the Anomalous Magnetic Moments of Leptons from First Principles. *Phys. Rev. Lett.*, 121:022002, Jul 2018.

[40] M.D. Morte, and et al. The Hadronic Vacuum Polarization Contribution to the Muon g 2 from Lattice QCD. *Journal of High Energy Physics*, 2017, Oct 2017.

[41] B. Chakraborty, C. T. H. Davies, P. G. de Oliveira, J. Koponen, G. P. Lepage, R. S. Van de Water. Hadronic Vacuum Polarization Contribution to a_μ from Full Lattice QCD. *Phys. Rev. D*, 96:034516, Aug 2017.

[42] T. Blum, and et al. Hadronic Light-by-Light Scattering Contribution to the Muon Anomalous Magnetic Moment from Lattice QCD. *Phys. Rev. Lett.*, 124:132002, Apr 2020.

[43] E. Chao, and et al. Hadronic Light-by-Light Contribution to g-2 from Lattice QCD: a Complete Calculation. *The European Physical Journal C*, 81(7), jul 2021.

[44] G. Colangelo, M. Hoferichter,and P. Stoffer. Two-pion Contribution to Hadronic Vacuum Polarization . *Journal of High Energy Physics*, 2019, 2019.

[45] M. Davier, A. Hoecker, B. Malaescu, and Z. Zhang. Reevaluation of the Hadronic Vacuum Polarisation Contributions to the Standard Model Predictions of the Muon g-2 and $\alpha(m_Z^2)$ using Newest Hadronic Cross-section Data. *The European Physical Journal C*, 77, 2017.

[46] M. Davier, A. Hoecker, B. Malaescu, and Z. Zhang. A New Evaluation of the Hadronic Vacuum Polarisation Contributions to the Muon Anomalous Magnetic Moment and to $\alpha(m_Z^2)$. *The European Physical Journal C*, 80, 2020.

[47] M. Hoferichter, B-L. Hoid, and B. Kubis. Three-pion Contribution to Hadronic Vacuum Polarization. *Journal of High Energy Physics*, 2019, 2019.

[48] J. Bijnens, N. Hermansson-Truedsson, and A. Rodríguez-Sánchez. Short-Distance Constraints for the HLbL Contribution to the Muon Anomalous Magnetic Moment. *Physics Letters B*, 798:134994, 2019.

[49] I. Danilkin, and M. Vanderhaeghen. Light-by-Light Scattering Sum Rules in Light of New Data. *Phys. Rev. D*, 95:014019, Jan 2017.

[50] G. Eichmann, C.S. Fischer, and R. Williams. Kaon-box Contribution to the Anomalous Magnetic Moment of the Muon. *Phys. Rev. D*, 101:054015, Mar 2020.

[51] A. Gerardin, H. B. Meyer, and A. Nyffeler. Lattice Calculation of the Pion Transition form Factor with $N_f = 2 + 1$ Wilson Quarks. *Phys. Rev. D*, 100:034520, Aug 2019.

[52] M. Knecht, S. Narison, A. Rabemananjara, and D. Rabetiarivony. Scalar Meson Contributions to a_μ from Hadronic Light-by-Light Scattering. *Physics Letters B*, 787:111–123, 2018.

[53] P. Masjuan, and P. Sanchez-Puertas. Pseudoscalar-pole Contribution to the $(g_\mu - 2)$: A Rational Approach. *Phys. Rev. D*, 95:054026, Mar 2017.

[54] K. Melnikov, and A. Vainshtein. Hadronic Light-by-Light Scattering Contribution to the Muon Anomalous Magnetic Moment Reexamined. *Phys. Rev. D*, 70:113006, Dec 2004.

[55] P. Roig, and P. Sanchez-Puertas. Axial-vector Exchange Contribution to the Hadronic Light-by-Light Piece of the Muon Anomalous Magnetic Moment. *Phys. Rev. D*, 101:074019, Apr 2020.

[56] G. Colangelo, M. Hoferichter, A. Nyffeler, M. Passera, and P. Stoffer. Remarks on Higher-order Hadronic Corrections to the Muon g-2. *Physics Letters B*, 735:90–91, 2014.

[57] T. Aoyama, T. Kinoshita, and M. Nio. Theory of the Anomalous Magnetic Moment of the Electron. *Atoms*, 7(1), 2019.

[58] P. Athron, and et al. New Physics Explanations of a in Light of the FNAL Muon g - 2 Measurement. *Journal of High Energy Physics*, 2021(9), sep 2021.

[59] A. Czarnecki, and W. J. Marciano. Muon Anomalous Magnetic Moment: A Harbinger for New Physics. *Physical Review D*, 64(1), jun 2001.

[60] A. Tewsley-Booth. The Precision Magnetic Field Analysis for the Fermilab Muon g-2 Experiment. *PhD thesis, University of Michigan*, 2019.

[61] A. Cherchiglia, D. Stockinger, and H. Kim. Muon g - 2 in the 2HDM: Maximum results and detailed phenomenology. *Physical Review D*, 2018.

[62] M. Krawczyk. The New (g-2) for Muon Measurement and Limits on the Light Higgs Bosons in 2HDM (II), 2001.

[63] M. Pospelov. Secluded U(1) Below the Weak Scale. *Physical Review D*, 80(9), nov 2009.

[64] H. Davoudiasl, H. Lee, and W. J. Marciano. Muon g-2, Rare Kaon Decays, and Parity Violation from Dark Bosons. *Physical Review D*, 89(9), may 2014.

[65] S.N. Gninenko, N.V. Krasnikov, and V.A. Matveev. Muon g-2 and Searches for a New Leptophobic sub-GeV Dark Boson in a Missing-Energy Experiment at CERN. *Physical Review D*, 91(9), may 2015.

[66] M. Tanabashi, and et al. Review of Particle Physics. *Phys. Rev. D*, 98:030001, Aug 2018.

[67] J. F. Bueno, and et al. Precise Measurement of Parity Violation in Polarized Muon Decay. *Physical Review D*, 84(3), Aug 2011.

[68] T. Albahri, and et al. (Muon g-2 collaboration). Measurement of the Anomalous Precession Frequency of the Muon in the Fermilab Muon $g-2$ Experiment. *Phys. Rev. D*, 103:072002, Apr 2021.

[69] A.P. Schreckenberger, and et al. New Fast Kicker Results from the Muon g-2 E-989 Experiment at Fermilab. In *9th International Particle Accelerator Conference*, 4 2018.

[70] N. Raha. The Current Status of the Fermilab Muon g–2 Experiment. *Universe*, 5(2), 2019.

[71] J. Kaspar, and et al. Design and performance of SiPM-based readout of PbF2 crystals for high-rate, precision timing applications. *Journal of Instrumentation*, 12(01), 1 2017.

[72] S. Charity. Beam Profile Measurements using the Straw Tracking Detectors at the Fermilab Muon g-2 experiment, and a Study of their Sensitivity to a Muon Electric Dipole Moment. *PhD thesis, University of Liverpool*, 2018.

[73] W. D. Phillips, W. E. Cooke, and D. Kleppner. Magnetic Moment of the Proton in H2O in Bohr Magnetons. *Metrologia*, 13(4):179, oct 1977.

[74] P. J. Mohr, D.B. Newell, and B.N. Taylor. CODATA Recommended Values of the Fundamental Physical Constants: 2014. *Rev. Mod. Phys.*, 88:035009, Sep 2016.

[75] W. Liu, and et al. High Precision Measurements of the Ground State Hyperfine Structure Interval of Muonium and of the Muon Magnetic Moment. *Phys. Rev. Lett.*, 82:711–714, Jan 1999.

[76] M. Smith. Developing the Precision Magnetic Field for the E989 Muon g-2 Experiment. *PhD thsis, University of Washington*, 2017.

[77] S. Corrodi. Trolley - "Cleaning up the Gold standard" - Motion and Position Uncertainties. *Fermilab E989 Muon g-2 docDB*, 18016, 2019.

[78] D. Flay, and et al. High-Accuracy Absolute Magnetometry with Application to the Fermilab Muon g-2 Experiment. *Journal of Instrumentation*, 16(12):P12041, dec 2021.

[79] R. Hong, and et al. Systematic and Statistical Uncertainties of the Hilbert-Transform Based High-precision FID Frequency Extraction Method. 1 2021.

[80] D. Flay. Plunging Probe Frequency Analysis. *Muon g-2 Internal DocDB*, 17821, 2019.

[81] M. Ubaidullah, and H. Qureshi. Frequency Extraction. *Muon g-2 Internal DocDB*, 25656, 2021.

[82] R Hong. Muon g-2 Trolley Probe Calibration. *Muon g-2 Internal DocDB*, 17833, 2019.

[83] R. Hong. Muon g-2 NMR Frequency Extraction. *Muon g-2 Internal DocDB*, 18347, 2019.

[84] B. Yi. Improved Trolley Position Determination. *Muon g-2 Internal DocDB*, 20532, 2019.

[85] B. Yi. Run 3 Trolley Calibration Analysis Update. *Muon g-2 Internal DocDB*, 25142, 2021.

[86] T. Chupp, and A. Tewsley-Booth. Full Field Analysis in a Nutshell v2+. *Muon g-2 Internal DocDB*, 23402, 2021.

[87] M. Fertl. Update - Temperature Dependance pet. Jelly. *Muon g-2 Internal DocDB*, 24697, 2021.

[88] D. Flay. E989 Note 191: Magnetic Field Calibration Analysis for Run 1. *Muon g-2 Internal DocDB*, 17821, 2020.

[89] B. Yi. E989 Note 230: Trolley Calibration Analysis for Run1. *Muon g-2 Internal DocDB*, 22947, 2020.

[90] P. Winter, and S. Corrodi. E989 Note 231: Trolley Temperature Correction. *Muon g-2 Internal DocDB*, 23025, 2020.

[91] A. Tewsley-Booth. Purcell Interpolation Review. *Muon g-2 Internal DocDB*, 17458, 2019.